

# **EFFECT OF JET FUEL COMPOSITION ON FORCED IGNITION IN GAS TURBINE COMBUSTORS**

A Dissertation  
Presented to  
The Academic Faculty

by

Sheng Wei

In Partial Fulfillment  
of the Requirements for the Degree  
Doctor of Philosophy in the  
Aerospace Engineering Department

Georgia Institute of Technology  
May 2019

**COPYRIGHT © 2019 BY SHENG WEI**

# **EFFECT OF JET FUEL COMPOSITION ON FORCED IGNITION IN GAS TURBINE COMBUSTORS**

Approved by:

Dr. Jerry Seitzman, Advisor  
School of Aerospace Engineering  
*Georgia Institute of Technology*

Dr. Jechiel Jagoda  
School of Aerospace Engineering  
*Georgia Institute of Technology*

Dr. Wenting Sun  
School of Aerospace Engineering  
*Georgia Institute of Technology*

Dr. Joseph Oefelein  
School of Aerospace Engineering  
*Georgia Institute of Technology*

Dr. Devesh Ranjan  
School of Mechanical Engineering  
*Georgia Institute of Technology*

Date Approved: [January 08, 2019]

To Yanran Wang and Clementine Wei

## ACKNOWLEDGEMENTS

Firstly, I want to thank Dr. Jerry Seitzman for guiding the research and helping me develop my critical thinking skills. I also want to thank Dr. Brandon Sforzo for introducing me into the research topic of forced ignition and helping me take the high-speed diagnostic images. Without inheriting the rig that he built, I will not be able to finish this thesis in a timely manner. Also many thanks to Dr. Sasha Bibik for spending much time on teaching me how to use the PDPA. I appreciate the availability of all research engineers on helping me with purchasing items or answering any questions I had. Throughout the PhD program, the combustion lab family helped me tremendously emotionally and intellectually. It is great to know that I am not alone in the struggle. I want to acknowledge Nishant, Sampath, Edwin, Aimee, Alex, Miad, Hanna, Vedant, Matt and all others. Thanks to the building managers, Chris and Seth, for keeping the Quincy alive for so long that I can complete my work.

I want to thank Georgia Tech Aerospace Engineering for recruiting me as a PhD student. I want to thank FAA for sponsoring this project.

Much thanks to my parents for raising me and giving me the opportunity to education. And thanks to everyone who help me along the way.

# TABLE OF CONTENTS

<b>ACKNOWLEDGEMENTS</b>	<b>iv</b>
<b>LIST OF TABLES</b>	<b>viii</b>
<b>LIST OF FIGURES</b>	<b>ix</b>
<b>LIST OF SYMBOLS AND ABBREVIATIONS</b>	<b>xv</b>
<b>SUMMARY</b>	<b>xvii</b>
<b>Chapter 1: Introduction and literature review</b>	<b>1</b>
<b>1.1 Motivation</b>	<b>1</b>
<b>1.2 How ignition occurs in gas turbine combustors</b>	<b>3</b>
<b>1.3 Literature Review</b>	<b>6</b>
1.3.1 Fuel effect on ignition in gas turbine engines	6
1.3.2 Forced ignition	10
<b>1.4 Thesis objectives and organization</b>	<b>14</b>
<b>Chapter 2: Background</b>	<b>17</b>
<b>2.1 Vortical structure of a pulsed jet</b>	<b>17</b>
<b>2.2 Planar Laser Induced Fluorescence (PLIF)</b>	<b>19</b>
<b>Chapter 3: Approach</b>	<b>21</b>
<b>3.1 Ignition facility</b>	<b>21</b>
3.1.1 Prevaporized fuel ignition facility	22
3.1.2 Liquid Fuel Spray Ignition Facility	25
<b>3.2 Description of Jet Fuels</b>	<b>27</b>
<b>3.3 Ignition probability measurement</b>	<b>29</b>
3.3.1 Diagnostic Approach	30
3.3.2 Probability and uncertainty calculation	31
3.3.3 Repeatability	33
<b>3.4 High speed diagnostics</b>	<b>34</b>
3.4.1 Schlieren Imaging	34
3.4.2 OH* Chemiluminescence	35
3.4.3 OH Planar Laser Induced Fluorescence (PLIF)	36
3.4.4 Imaging system and synchornization	37
3.4.5 Image processing	40
<b>3.5 Droplet distribution measurement</b>	<b>42</b>
<b>3.6 Reduced-order forced ignition modeling approach</b>	<b>46</b>
3.6.1 Two-stage perfectly stirred reactor model	46
3.6.2 Reduced-order liquid spray ignition model.	50

<b>Chapter 4: Spark kernel structure</b>	<b>59</b>
<b>4.1 Ignition process revelation via high speed diagnostics</b>	<b>59</b>
4.1.1 Spark kernel characterization	59
4.1.2 Ignition characterization – fuel A2	62
4.1.3 Ignition characterization – fuel comparison	69
<b>4.2 Chapter summary</b>	<b>73</b>
<b>Chapter 5: Forced ignition of prevaporized fuel/air mixture</b>	<b>75</b>
<b>5.1 Effect of equivalence ratio and fuel performance ranking</b>	<b>75</b>
<b>5.2 Reduced order simulation results</b>	<b>82</b>
5.2.1 Successful vs. unsuccessful ignition	82
5.2.2 Fuel comparison: A2 vs. C1	87
5.2.3 Fuel comparison for five fuels: A1, A2, A3, C1, C5	95
<b>5.3 Chapter summary</b>	<b>99</b>
<b>Chapter 6: Forced ignition of liquid jet fuel</b>	<b>101</b>
<b>6.1 Ignition probability ranking</b>	<b>101</b>
<b>6.2 Droplet distribution measurement</b>	<b>107</b>
<b>6.3 Probability correlations</b>	<b>112</b>
6.3.1 Correlations to single properties	112
6.3.2 Correlation to physical models	116
6.3.3 Summary	124
<b>6.4 Reduced order simulation</b>	<b>125</b>
6.4.1 Model validation	126
6.4.2 Energy transfer mechanisms	127
6.4.3 Effect of droplet temperature and air temperatures	132
6.4.4 Effect of droplet relative velocity (Reynolds Number)	136
6.4.5 Effect of fuel chemistry and recovery temperatures on ignition	139
6.4.6 Effect of droplet distribution	143
<b>6.5 Chapter summary</b>	<b>146</b>
<b>Chapter 7: Conclusions and recommendations</b>	<b>148</b>
<b>7.1 Summary and conclusions</b>	<b>148</b>
7.1.1 Paradigm for forced ignition	149
7.1.2 Droplet heating	150
7.1.3 Fuel chemistry	151
<b>7.2 Recommendation for future work</b>	<b>152</b>
<b>APPENDIX A. Additional fuel properties</b>	<b>154</b>
<b>APPENDIX B. Imaging processing code (Matlab)</b>	<b>155</b>
<b>APPENDIX C. PSR Two-stage Ignition code (Python)</b>	<b>159</b>
<b>APPENDIX D. Abrazom and Sirignano vaporization model</b>	<b>164</b>
<b>APPENDIX E. PSR Droplet ignition code (Python)</b>	<b>165</b>

<b>APPENDIX F. ASME D341 – python code for viscosity approximation</b>	<b>175</b>
<b>APPENDIX G. Absolute Ignition probability ranking</b>	<b>177</b>
<b>REFERENCES</b>	<b>179</b>

## LIST OF TABLES

Table 1. Test conditions for prevaporized fuels.....	24
Table 2. Test conditions for liquid fuel spray ignition.....	27
Table 3. Brief description of tested fuels. ....	29
Table 4. Summary of the imaging components. ....	36
Table 5. Ignition delay time based on minimum values obtained in Figure 4.1-15. ....	73
Table 6. Parametric study to characterize the effect of the fuel type and the boiling temperatures on ignition. ....	141
Table 7. Absolute ignition probability for room temperature fuel spray.....	177
Table 8. Absolute ignition probability for chilled fuel spray.....	178



## LIST OF FIGURES

Figure 1.2-1. Modified schematic of a combustion chamber from [5]. Cloud 1 represents the initial high temperature plasma generated from the ignitor. Cloud 2 represents cooled ignition kernel after interacting with an air layer with little/no fuel present. Cloud 3 represents ignition kernel transitioning into a self-sustaining flame after interaction with fuel/air mixtures. ....	3
Figure 1.2-2. A CAD drawing of the VESTA manufactured by Turbomeca. Two igniters are used to ignite 18 burners. 14 burners are shown. Adapted from [6]. ....	5
Figure 1.3-1. Comparison of measured and predicted values of $q_{LLO}$ for J79-17C combustor, adapted from [16]. Compositions of fuels (1A – 6A) is provided in [16]. ....	7
Figure 1.3-2. Comparison of measured and predicted values of $q_{LLO}$ for a TF41 combustor for various fuel blends, adapted from [16]. ....	7
Figure 1.3-3. The range of combustor inlet conditions for primary figure of merits (FOM) that include lean blowout, cold start, and high-altitude ignition, adapted from [4]. ....	9
Figure 1.3-4. Combine PLIF and emission signal of an ignition sequence in an SI direct injection (DI) engine [20]. TDC stands for top-dead-center. A and B stands for after and before. A spark is generated at 34° BTDC. The angles are the crank angles. ....	11
Figure 1.3-5. CFD simulation of a spark discharge from two electrodes in a convecting air flow [21]. ....	12
Figure 1.3-6. Cross-sections of the two types of surface discharge igniters [22]. Left: Sunken fire igniter with recessed gap; Right: Flush fire igniter with flush gap. ....	13
Figure 1.3-7. t-ratio from a multivariable linear regression model for predicting ignition probability [23]. ....	14
Figure 2.1-1. The fluorescence image through the pulsed jets' center planes. The top row shows a fast rise in the pressure driving the pulse and then a slow decay in the pressure. The bottom row shows the opposite case, in which the pressure rises slowly and decays quickly. Adapted from [25]. ....	18
Figure 2.2-1. Energy level diagram of LIF [29]. ....	20
Figure 3.1-1. Schematic of test facility for prevaporized fuels, adapted from [23]. ....	22
Figure 3.1-2. Schematic of fuel and air delivery system. ....	24
Figure 3.1-3. Schematic of test facility modified for liquid fuel spray, adapted from [23]. ....	25
Figure 3.1-4. Liquid fuel supply for spray testing. ....	26
Figure 3.3-1. Timing diagram for measurement of ignition probability. ....	31
Figure 3.3-2. A sample image of a successful ignition event with room temperature fuel spray, with the camera exposure synchronized according to timing signals in Figure 3.1-1. ....	31
Figure 3.3-3. Absolute probabilities for fuels A2 and C1 of room temperature ignition acquired on two different days. ....	34
Figure 3.4-1. Profile schematic of schlieren illumination and imaging configuration (not to scale); C2 is the schlieren imaging camera. ....	35

Figure 3.4-2. Timing relations of the beginning of TTL signal (To), laser signal, gate opening of intensifier for chemiluminescence camera (I1), gate opening of intensifier for the PLIF camera (I2), and gate opening of the schlieren camera (C2). .....	38
Figure 3.4-3. Top view schematic of test section with relative position of the (C1) timing camera, (C2) schlieren camera, (C3) chemiluminescence camera, and (C4) PLIF camera. intensifiers on the (I1) chemiluminescence camera and (I2) PLIF camera are also depicted. ....	39
Figure 3.4-4. Depiction of edge-tracking algorithm used to obtain kernel velocities. ....	40
Figure 3.4-5. Calibration images acquired before experiments for registration. Schlieren camera (C2) was used as reference for chemiluminescence (C3) and PLIF (C4) cameras. ....	41
Figure 3.5-1. Select PDPA parameters. ....	44
Figure 3.5-2. Top-down view of the schematic of the PDPA system setup. T is the transmitter that emits laser beams. R is the receiver that acquires laser Doppler signals. ....	44
Figure 3.5-3. Location of PDPA measurements. Left: 3 centerline locations where measurements are taken. Right: Measurements are taken radially downward at each location: $r$ is the transverse direction, and $r'$ is the span-wise direction. ....	45
Figure 3.6-1. Setup of two stage perfectly stirred model. Adapted from [38]. ....	49
Figure 3.6-2. Schematic for hybrid chemistry approach in breaking down large fuel molecules. ....	50
Figure 3.6-3. Conceptual model PSR modeling with droplet vaporization. ....	51
Figure 3.6-4. Descriptions of the modules used to achieve liquid droplet vaporization and chemical reaction in gas phase. ....	52
Figure 3.6-5. Example of droplet distribution based on a Rosin-Rammler distribution, $X=10$ , $q=3.8$ . A total mass of 1 mg is used to obtain the number of droplets in each diameter. ....	54
Figure 3.6-6. Radius (red) and Temperature (green) profile for a 10 $\mu\text{m}$ , n-dodecane droplet heating and vaporizing in 880 K ambient air with a relative velocity of 10 m/s. ....	57
Figure 3.6-7. The vaporization rate $\dot{m}$ (red) and the heat transferred to the droplet $\dot{q}$ (green) profile for a 10 $\mu\text{m}$ , n-dodecane droplet heating and vaporizing in 880 K ambient air with a relative velocity of 10 m/s. ....	57
Figure 3.6-8. Results for a 10 $\mu\text{m}$ radius n-dodecane droplet in 880 K environment at 10 m/s relative velocity from [40]. Model 4 is from Abramzon and Sirignano[39]. ....	58
Figure 4.1-1. Vertical velocity histories of the spark kernel, determined from the high-speed schlieren images, averaged over three successful and unsuccessful ignition events. For the A2 fuel. The horizontal bars show the uncertainty in time after the spark discharge due to triggering of the camera. ....	61
Figure 4.1-2. Vertical velocity history of the spark kernels for each of the fuels tested, each averaged over three successful events. ....	61
Figure 4.1-3. Volumetric growth of the spark kernel following discharge, obtained from high-speed schlieren data. ....	62
Figure 4.1-4. Intensity per pixel versus time for a successful ignition event and an unsuccessful event for fuel A2. ....	63
Figure 4.1-5. Sequence of simultaneously acquired emission (top), PLIF (middle) and schlieren (bottom) images for early times from a successful ignition event with the A2	

fuel; the event is the same used in Figure 4.1-4. The crossflow direction is left to right in the images. ....	64
Figure 4.1-6. Successful ignition with A2, case 2. ....	65
Figure 4.1-7. Successful ignition with A2, case 3. ....	65
Figure 4.1-8. Sequence of PLIF images for later times for the successful A2 ignition event depicted in Figure 4.1-5. ....	68
Figure 4.1-9. Sequence of simultaneously acquired emission (top), PLIF (middle) and schlieren (bottom) images for early times from a failed ignition event with the A2 fuel; the event is the same used in Figure 4.1-4. ....	68
Figure 4.1-10. Sequence of simultaneously acquired emission (top), PLIF (middle) and schlieren (bottom) images for early times from a successful ignition event with the C5 fuel. ....	70
Figure 4.1-11. Successful ignition with C5, case 2. ....	70
Figure 4.1-12. Successful ignition with C5, case 3. ....	71
Figure 4.1-13. Sequence of simultaneously acquired emission (top), PLIF (middle) and schlieren (bottom) images for early times from a successful ignition event with the C1 fuel. ....	71
Figure 4.1-14. Successful ignition with C1, case 2. ....	72
Figure 4.1-15. Spatially integrated and background corrected emission camera intensities for three fuels. Each data point represents the average over three successful ignition events. ....	73
Figure 5.1-1. Binned Ignition probability data. Each data point contains ~300 ignition events. ....	77
Figure 5.1-2. Ranking of relative ignition probability with respect to that of A2 for prevaporized fuel/air mixtures. The equivalence ratio of the main flow is at 0.675. ....	78
Figure 5.1-3. Relative ignition probability (vaporized fuel) compared to the fuel's DCN. ....	80
Figure 5.1-4. Relative ignition probability (vaporized fuel) compared to volumetric percentage of iso-paraffins. ....	80
Figure 5.1-5. Relative ignition probability (vaporized fuel) compared to volumetric percentage of n-paraffins. ....	81
Figure 5.1-6. Relative ignition probability (vaporized fuel) compared to volumetric percentage of aromatics. ....	81
Figure 5.1-7. Relative ignition probability (vaporized fuel) compared to volumetric percentage of cycloparaffins. ....	82
Figure 5.2-1. A successful ignition at $\phi=0.50$ (blue solid line) and an unsuccessful ignition at $\phi=0.48$ (blue dashed line). The solid black line represents the kernel temperature if no fuel is entrained. The second stage fuel entrainment starts at 0.09 ms. A spark is formed at $t=0$ . ....	83
Figure 5.2-2. Chemical heat release rate and dilution cooling rate for the successful (solid blue) and the unsuccessful (dashed blue) as in Figure 5.1-1. The vertical dotted lines indicate the time when a flammable mixture starts being entrained. ....	84
Figure 5.2-3. The bifurcation for the lean ignition limits for A2 and C1. The red curves show result for C1, and the blue curve show results for A2. The solid lines are for successful cases, and the dashed lines are for unsuccessful cases. The dark solid line	

shows the kernel temperature without fuel entrainment. The vertical dotted line indicates when fuel entrainment starts (at 0.09 ms). .....	87
Figure 5.2-4. Chemical heat release rate and dilution cooling rate for the successful (solid blue) and the unsuccessful (dashed blue) as in Figure 5.2-3. ....	88
Figure 5.2-5. Ignition kernel simulation for A2 and C1 at $\phi=0.6$ . ....	89
Figure 5.2-6. The mole fraction of the intermediate breakdown products in the kernel as a function of time after the kernel initiation for A2 at $\phi=0.60$ . The fuel is introduced at 0.09 ms. ....	91
Figure 5.2-7. Intermediate A2 products for early times at conditions of Figure 5.2-6. ....	91
Figure 5.2-8. Intermediate fuel breakdown products for unsuccessful ignition kernel of C1 for $\phi=0.60$ and early times after fuel introduction. ....	92
Figure 5.2-9. Intermediate fuel breakdown products for successful ignition kernel of C1 for $\phi=0.62$ and early times after fuel introduction. ....	92
Figure 5.2-10. Autoignition of isobutene and benzene at 1800 K and 1400 K at one atmosphere and $\phi=1$ . ....	93
Figure 5.2-11. Autoignition delay time as a function of $1000/T$ for intermediate species of the products from the original fuel break down. ....	94
Figure 5.2-12. The lean ignition limit (LIL) for five fuels at conditions like the test conditions, with 90 $\mu$ s transit time and 60 $\mu$ g/s mass entrainment rate. ....	95
Figure 5.2-13. Ethylene concentration during early times after fuel entrainment for $\phi=0.6$ . ....	96
Figure 5.2-14. The left graph shows the sensitivity analysis on the $\tau_{\text{transit}}$ time while keeping the mass flow rate fixed. The right graph shows the effect of changing the entrainment while keeping $\tau_{\text{transit}}$ fixed. ....	97
Figure 6.1-1. Probability ranking with probabilities scaled to the probability of A-2, with probabilities acquired under test conditions in Table 2 for room temperature fuels. ....	102
Figure 6.1-2. Probability ranking with probabilities scaled to the probability of A2, with probabilities acquired under test conditions listed in Table 2 for the chilled fuels. ....	104
Figure 6.1-3. Viscosities versus temperature for a few fuels studied in this program. ASTM D341 is used to predict viscosities at different temperatures. $T_{\text{cold}}$ is the temperature of the tested chilled fuels, and $T_{\text{RT}}$ is the temperature of the tested room temperature fuels. ....	106
Figure 6.2-1. Sauter Mean Diameter (SMD) profiles in the spanwise and transverse directions at the plane 10 mm downstream of the nozzle for fuel C3. The origin is defined at the point at which the center line intersects the cross-section. ....	109
Figure 6.2-2. Transverse SMD ( $D_{32}$ ) profiles at the plane 30.4 mm downstream of the nozzle. The origin is defined at the point at which the center line intersects the cross-section. The red line indicates the position of the igniter. ....	110
Figure 6.2-3. The measured $D_{32}$ versus the predicted $D_{32}$ at 5.8 mm above the igniter in the 30.4 mm plane. ....	110
Figure 6.2-4. Droplet size number density distribution at 5.8 mm above the igniter center in the 30.4 mm plane downstream of the nozzle. Normalized by the total number of droplets captured. ....	111
Figure 6.2-5. Rosin-Rammer fitting for A2 in Figure 6.2-4. ....	112
Figure 6.3-1. The relative ignition probabilities versus DCNs for ignition of room temperature fuel sprays. ....	113

Figure 6.3-2. The relative ignition probability versus fuels' density at 15 C for ignition of room temperature fuel sprays.....	114
Figure 6.3-3. The linear correlation indexes between the ignition probability and the properties.....	115
Figure 6.3-4. Relative ignition probabilities versus the 10% recovery temperature. ....	115
Figure 6.3-5. Relative ignition probabilities versus the kinematic viscosities. ....	116
Figure 6.3-6. Relative ignition probabilities versus 10% recovery temperature. Left: fuel spray at 294 K; Right: fuel spray at 246 K. ....	117
Figure 6.3-7. The heating time to the 10% recovery temperature. The droplets is placed in 1600 K quiescent air, and the initial temperatures of the droplets are 294 K (left) and 246 K (right). The droplet sizes for each fuel are predicted by Equation 10.....	119
Figure 6.3-8. The heating time to the 20% recovery temperature. The droplets is placed in 1600 K quiescent air, and the initial temperatures of the droplets are 294 K (left) and 246 K (right). The droplet sizes for each fuel are predicted by Equation 10.....	120
Figure 6.3-9. The heating time to the 50% recovery temperature. The droplets is placed in 1600 K quiescent air, and the initial temperatures of the droplets are 294 K (left) and 246 K (right). The droplet sizes for each fuel are predicted by Equation 10.....	120
Figure 6.3-10. The relative ignition probabilities versus the relative effective vaporizations calculated with Equation 29. The ambient temperature is 1600 K. ....	123
Figure 6.3-11. Relative ignition probability versus relative lean ignition limits calculated with Equation 30. ....	124
Figure 6.4-1. Temperature history for an entrained fluid mixture with an equivalence ratio of 1. The red line is for 10 $\mu\text{m}$ droplets, and the orange line is for 20 $\mu\text{m}$ droplets. The black line indicates temperature of the profile if no fuel droplets are introduced. The dashed vertical line indicates the time (20 $\mu\text{s}$ ) when fuel droplets are introduced. ....	128
Figure 6.4-2. The chemical heat release rates for ignition of the 10 $\mu\text{m}$ droplets (red) and the 20 $\mu\text{m}$ droplets. ....	129
Figure 6.4-3. The dilution cooling rates for ignition of the 10 $\mu\text{m}$ droplets (red) and the 20 $\mu\text{m}$ droplets. ....	129
Figure 6.4-4. The energy supplied to the droplets for heating and vaporization for ignition of the 10 $\mu\text{m}$ droplets (red) and the 20 $\mu\text{m}$ droplets. ....	130
Figure 6.4-5. The total vaporization rate for ignition of the 10 $\mu\text{m}$ droplets (red) and the 20 $\mu\text{m}$ droplets. ....	131
Figure 6.4-6. Kernel temperature history. The red line indicates the case where both the air and the fuel are at 300 K. The blue line indicates the case where the air temperature is set at 250 K. The orange line indicates the case where the fuel temperature is set at 250 K case.....	133
Figure 6.4-7. Total chemical heat release rate history. The red line indicates the case where both the air and the fuel are at 300 K. The blue line indicates the case where the case where the air temperature is set at 250 K. The orange line indicates the case where the fuel temperature is set at 250 K case. The purple, dashed, vertical line indicates time when fuel droplets are introduced into the kernel.....	134
Figure 6.4-8. Kernel dilution cooling rate history. The red line indicates the case where both the air and the fuel are at 300 K. The blue line indicates the case where the case where the air temperature is set at 250 K. The orange line indicates the case where the fuel temperature is set at 250 K case. ....	136

Figure 6.4-9. Temporal profile of heat transfer rate to droplets. The red line indicates the case where both the air and the fuel are at 300 K. The blue line indicates the case where the air temperature is set at 250 K. The orange line indicates the case where the fuel temperature is set at 250 K case.....	136
Figure 6.4-10. Kernel temperature histories. The red line indicates the case where $Re_D=0$ . The blue line indicates the case where the case where $Re_D=5$ . The orange line indicates the case where $Re_D=10$ .....	137
Figure 6.4-11. Chemical heat release rate histories. The red line indicates the case where $Re_D=0$ . The blue line indicates the case where the case where $Re_D=5$ . The orange line indicates the case where $Re_D=10$ . ....	138
Figure 6.4-12. Temporal evolution of heat transfer rates to the droplets. The red line indicates the case where $Re_D=0$ . The blue line indicates the case where the case where the $Re_D=5$ . The orange line indicates the case where $Re_D=10$ . ....	139
Figure 6.4-13. Dependence of critical droplet size on boiling temperatures representing the range of the 10%-40% recovery temperatures. The blue dashed vertical line indicates the variation in droplet sizes due to the differences in viscosity for the droplet size at the boiling temperature of 493 K. ....	142
Figure 6.4-14. The maximum droplet sizes in between the successful/unsuccessful ignition cases versus the boiling temperatures representing the range of the 10%-40% recovery temperatures. The initial fuel temperatures are at 220 K and 300 K. The blue dashed vertical line indicates the variation in droplet sizes due to the differences in viscosity for the droplet size at the boiling temperature of 493 K.....	143
Figure 6.4-15. $dQ/dD$ derived from the Rosin-Rammler distribution (Equation 17) for $X=20$ and $q=3$ (blue), 5 (orange), and 10 (green). ....	144
Figure 6.4-16. The temperature profiles as a function of time since the spark is introduced for three droplet size distribution based on the Rosin-Rammler distribution. ....	145
Figure 6.4-17. The chemical heat release rates as a function of time since the spark is introduced for three droplet size distribution based on the Rosin-Rammler distribution. ....	145
Figure 6.4-18. The liquid fuel vaporization rates as a function of time since the spark is introduced for three droplet size distribution based on the Rosin-Rammler distribution. ....	146
Figure 7.1-1. Schematic of the proposed paradigm for forced ignition of liquid fuel/air mixture in gas turbine combustors .....	149

## LIST OF SYMBOLS AND ABBREVIATIONS

$\phi$	Equivalence ratio
ASTM	American Society for Testing and Materials
PLIF	Planar Laser Induced Fluorescence
PDPA	Particle Doppler Phase Analyzer
NJFCP	National Jet Fuel Combustion Program
PSR	Perfectly Stirred Reactor
P	Ignition Probability
$N_{\text{success}}$	Number of Successful Events
$P_{A2}$	Absolute Ignition Probability of fuel A2
CEM	Controlled Evaporator Mixer
MFC	Mass Flow Controller
CDF	Cumulative Distribution Function
PDF	Probability Density Function
$\mathcal{L}_v$	Latent heat of vaporization
h	Convective heat transfer coefficient
SMD	Sauter Mean Diameter
NJFCP	National Jet Fuel Combustion Program
HEFA	Hydro-processed Ester and Fatty Acids
$\sigma$	Surface tension
$\mu$	Kinematic viscosity
$\nu$	Dynamic viscosity
DCN	Derived Cetane Number

LIL Lean Ignition Limit, defined as the lowest  $\phi$  where ignition can occur



## SUMMARY

The rapid growth in the aviation industry means increasing consumption of jet fuels, which is leading to greater interest in alternate and sustainable fuel sources. The overall properties of these alternative fuels can be designed to meet existing standards. Nevertheless, the compositional differences between alternative and conventional fuels can lead to important variations in chemical and physical properties that impact engine performance. For example, ignition is of paramount importance to ensure reliable operation, especially in extreme conditions like cold starts and high altitude relights. For aircraft engines, ignition is the process of creating self-sustaining flames starting with a high-temperature source located near a combustor liner. This thesis is devoted to studying the differences in ignition behavior due to the variations in fuel composition.

Fuel variations in ignition are studied in a well-characterized test facility that is readily amenable to modeling and simulation. The experiments employ a sunken-fire ignitor, like those typically employed in aircraft engines, operating at 15 Hz with  $\sim 1.25$  J spark energy. Performance differences among fuels are characterized through their ignition probabilities. To understand both the chemical and physical fuel effects on ignition, both prevaporized fuels and liquid fuel sprays are examined. The purpose of prevaporizing the fuel is to remove the process of liquid to gas transition and to focus on combustion chemistry alone. In the forced ignition of liquid fuel sprays, which mimics the situation encountered in aviation gas turbine engines, both physical and chemical properties of the fuel are relevant. Statistically significant differences between fuel ignition probabilities are observed. The droplet heating time is shown to correlate well with ignition probability. A particle Doppler

phase analyzer (PDPA) is used to study droplet size distribution near the ignitor. These droplet distribution measurements can be useful for future CFD modeling.

In addition to differentiating fuel performances through ignition probability, advanced diagnostic techniques are employed to understand the evolution of a spark kernels as it interacts with combustible mixtures. These techniques include high speed OH planar laser induced fluorescence, OH\* chemiluminescence, and schlieren imaging. The results reveal the entrainment of ambient fluid into the convecting spark kernel, the decomposition of vaporized jet fuel in the high temperature kernel, and the transition from local “hot spots” within the spark kernel to a self-sustaining flame.

In addition to the experiments, reduced order modeling is used to better understand the physics and chemistry of ignition for both prevaporized and liquid fuels. Chemical differences are found to depend on the relative distribution between intermediate breakdown products (e.g., ethylene, propene and isobutene) from the parent fuels, as these intermediates have drastically different chemical rates as a function of temperature. The energy transfer mechanisms important in the ignition of liquid fuel sprays are also identified. The chemical heat release and the dilution cooling rates are orders of magnitudes larger than the heat required for the droplets’ heating and vaporization. However, the droplet heating time is shown to have the largest impact on ignition performance.

# **CHAPTER 1:**

## **INTRODUCTION AND LITERATURE REVIEW**

Combustion is the process of converting chemical energy into thermal energy[1]. The thermal energy can then be converted into useful works through machines such as internal combustion (IC) engine and turbine engines. Liquid-fueled turbines are widely used in aviation industry. The successful operation of the gas turbine engines depends on many combustion processes. These combustion processes include ignition and flame stabilization. In recent years, the introduction of non-petroleum based alternative jet fuels into the existing turbine engine infrastructures has introduced the issue of uncertainties on the reliable operation of the engines. These next generation alternative jet fuels need to be properly researched and certified prior to wide usage. This thesis focuses on studying the ignition performances of alternative jet fuels, with the goal of identifying the key fuel differences that contribute to successful ignition.

### **1.1 Motivation**

As jet fuel production methods through non-fossil fuel sources are maturing, the replacement of fossil fuel-based jet fuel by alternative sources is becoming a reality. These alternative fuel production approaches include the Fisher-Tropsch process, hydrotreating organic compounds, and direct fermentation of sugars. The fuel produced through these processes are termed “synthetic paraffinic kerosene” (SPK) and “hydrotreated renewable jet” (HRJ) fuels. In contrast to petroleum-based jet fuels, these alternative jet fuels contain less variety of chemical compound groups. These fuels are commonly used as mix-ins with

conventional jet fuels, and the mix-ins are referred to as “drop-in” fuels. Reliable operation is of paramount importance to aircraft. Mixing alternative hydrocarbon fuels with conventional kerosene fuel introduces uncertainties to the aircraft engines’ operations, such as ignition. From the standpoint of ignition, these new fuel blends need to perform like the conventional jet fuels to be acceptable. To ensure consistent aircraft performance after introduction of synthetic fuel, ASTM (American Society for Testing and Materials) established standards in 2016 and 2017 to certify engine performance and specify acceptable fuel properties after synthetic fuel introduction. In ASME D4054-16[2], standard procedures were established for testing and approving new jet fuel blends. ASME D4054-16 further specifies that only the original equipment manufacturers (OEM) of gas turbine combustors can approve a fuel blend. In ASME D7566-17a [3], the acceptable range of physical properties and chemical compositions was specified. Costs for OEM fuel certification can be high due to expensive engine operation and costs of fuel production. Initial screening through laboratory testing can be a reasonable choice. Not only is the cost of laboratory testing less expensive, but also laboratory testing can give more insight into the fuels’ performance in a controlled environment. The National Jet Fuel Combustion Program (NJFCP)[4] was established to study effect of blending nonconventional fuel sources into current jet fuels. The fuels tested in this study are provided by NJFCP. This study uses laboratory testing to understand the effect of jet fuel composition on forced ignition in a well-controlled, easy-to-model test facility. More specifically, this research focuses on the transition of a spark kernel into a growing self-sustained flame.

## 1.2 How ignition occurs in gas turbine combustors

Before proceeding with a literature review of forced ignition in gas turbine engines, it is helpful to have a proper understanding of the ignition process in a gas turbine engine.

Figure 1.2-1 illustrates the ignition process in a liquid spray-fueled combustor.

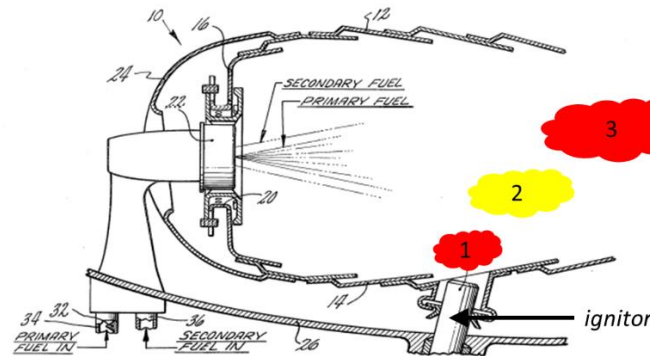


Figure 1.2-1. Modified schematic of a combustion chamber from [5]. Cloud 1 represents the initial high temperature plasma generated from the ignitor. Cloud 2 represents cooled ignition kernel after interacting with an air layer with little/no fuel present. Cloud 3 represents ignition kernel transitioning into a self-sustaining flame after interaction with fuel/air mixtures.

In conventional gas turbine engines, the very first step in forced ignition is to create a spark<sup>1</sup> through an electrical discharge (cloud 1 in Figure 1.2-1). This spark kernel is ejected into a region with little to no fuel, because to ensure long life ignitors are typically placed away from the combustion zone where the gas temperature is high. During this initial period, the ignition kernel entrains the surrounding air with little to no fuel. As the kernel entrains surrounding fluids, the size of the kernel will grow, and its temperature will decrease, as illustrated by cloud 2 in Figure 1.2-1. After a short transition time through this

<sup>1</sup>In this thesis, the term “spark” means the very high energy density plasma generated by electrical discharge; the term “spark kernel” or “kernel” will refer to the high-temperature gas after the plasma cools down due to interaction with cold surrounding fluids.

air layer, the spark kernel starts to interact with flammable fuel/air mixtures, and if ignition is successful, it generates a self-sustaining flame (cloud 3 in Figure 1.2-1). This succession of events describes the first phase of successful ignition in an aeroengine combustor.

The second phase of the ignition process concerns the ability of the flame to propagate upstream and grow in the non-uniform, turbulent combustor flowfield. Strong turbulence can severely stretch and quench the self-sustained flame kernel. Furthermore, the flame kernel must propagate upstream to a location where flame-stabilization can occur. In typical gas turbines, one or two igniters are used to initiate combustion in a dozen or more burners (Figure 1.2-2). Thus during the third phase of successful ignition, the flame must propagate and stabilize all the combustor cups (this is called light around). A successful engine lightoff requires each of these three phases of the ignition process to be successful.

The focus of this research is the first phase of the ignition process, namely generation of self-sustaining flame kernel from a spark kernel. The generation of a self-sustaining flame can most clearly demonstrate the differences among the fuel blends in initiating a flame. The success of the second and third phase will depend on the success of the first phase, and the specific geometry of a combustor.

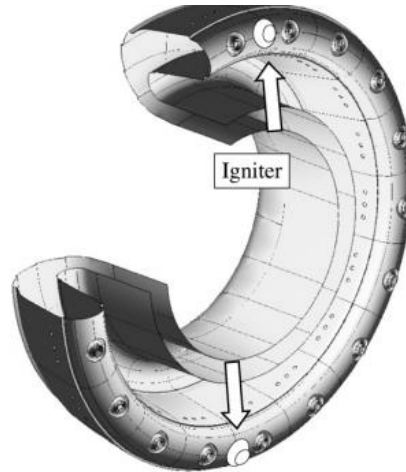


Figure 1.2-2. A CAD drawing of the VESTA manufactured by Turbomeca. Two igniters are used to ignite 18 burners. 14 burners are shown. Adapted from [6].

Although a successful ignition event is shown in Figure 1.2-1, the outcome of any one ignition event is stochastic, meaning that an electrical discharge may or may not lead to a self-sustaining flame kernel [7, 8]. There are multiple sources of stochasticity for ignition. First, there is the breakdown and discharge process in the igniter, where the duration and location of the current path depends on the instantaneous conditions between the electrodes. Second, when spark kernel expands away from the ignitor, strong shear layers are induced by the high velocity gas, and thus the turbulence in the ignition kernel is strong. Strong turbulence can affect the entrainment rate of surrounding fluids and thus introduce variations in the spark kernel development. The droplet distribution in space is also stochastic in time. Different spark kernels will not experience the same droplets as the kernels develop. Turbulence in the flow can also quench a flame. Given the probabilistic nature of ignition, one or even a few ignition event measurements of a fuel are insufficient to characterize its ignition performance; thousands of ignition events are necessary.

### 1.3 Literature Review

#### 1.3.1 Fuel effect on ignition in gas turbine engines

In a paper published by A.H. Lefebvre [9] in 1985, the ignition performance of fuels of various composition was analyzed based on experimental data from various studies in actual gas turbine combustors [10-15]. In that paper, expressions were developed that correlate the minimum fuel/air ratio for successful engine lightoff to: combustor design, combustor operating parameters, average droplet sizes, and the fuel's heating value. The minimum fuel/air ratio for lean lightoff  $f_{LLO}$  was given as

$$f_{LLO} \propto \frac{\dot{m}_{A, primary}}{V_c P_3^{1.5} e^{T_3/300}} \times \frac{D^2}{\lambda \times LHV} \quad (1)$$

where  $\dot{m}_{A, primary}$  is the mass air flow rate in the primary zone,  $V_c$  is the volume of the primary combustion zone,  $D$  represents the Sauter Mean Diameter (SMD) of the overall spray, and LHV is the lower heating value of the fuel.  $\lambda$  is an effective vaporization constant, and its definition can be found in Equation 22 in [9]. It should be noted that this correlation for lean lightoff has the exact same form as that developed for lean blow out (LBO) in the same paper (Eqn 27 in [16]). In some cases, the LLO correlations show good matching between the predicted fuel/air ratio and the measured fuel/air ratio, such as shown in Figure 1.3-1. In other cases, however, this equation produces a poor correlation with measurements, such as that in Figure 1.3-2.



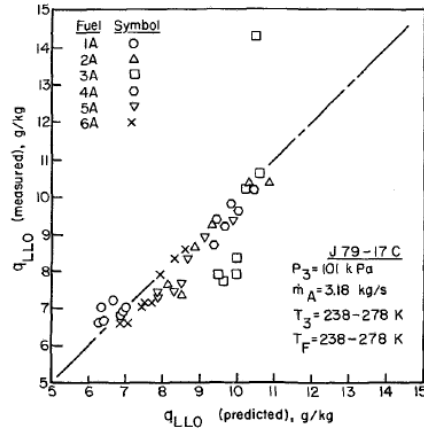


Figure 1.3-1. Comparison of measured and predicted values of  $q_{LLO}$  for J79-17C combustor, adapted from [16]. Compositions of fuels (1A – 6A) is provided in [16].

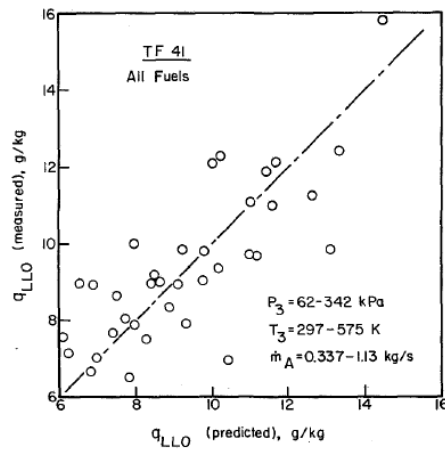


Figure 1.3-2. Comparison of measured and predicted values of  $q_{LLO}$  for a TF41 combustor for various fuel blends, adapted from [16].

The partial success of Lefebvre's expression in correlating ignition results suggests that it captures some key physical process that control ignition, such as the impact of droplet size. However, the poor results in some cases also indicate other important physical processes or fuel properties may be overlooked. Contrary to the significant difference

among fuels in their ignition performances, in a later study [17], the ignition performances of various fuel blends are shown to have little differences.

To pinpoint the relevant parameters during ignition, Lefebvre referred to a standard model for the minimum energy required to ignite a premixed fuel-air mixture based on the ability of a laminar spherical flame to propagate in a self-sustained manner [18]. More precisely it is when the heat release from the spherical flame is greater than conduction cooling to the surrounding gas. The minimum supplied ignition energy,  $E_{min}$ , is given by the following equation

$$E_{min} = c_{pA}\rho_A\Delta T_{st}(\pi/6)d_q^3 \quad (2)$$

where  $c_{pA}$  is the heat capacity of air,  $\rho_A$  is the density of air,  $\Delta T_{st}$  is the temperature between the initial air temperature and the stoichiometric burning temperature, and  $d_q$  is the quenching distance. For a monodispersed spray in a quiescent environment [19], the quenching distance can be expressed as

$$d_q = \left[ \frac{\rho_F D_0^2}{\rho_A \phi \ln(1 + B_{st})} \right]^{0.5} \quad (3)$$

where  $\rho_F$  is the density of the fuel,  $D_0$  is the droplet size of the monodisperse spray,  $\rho_A$  is the density of the air,  $\phi$  is the equivalence ratio, and  $B_{st}$  is the Spalding mass transfer number. This minimum ignition energy accounts for the effect of droplet size and fuel vaporization process. A smaller quenching distance will give a smaller minimum ignition energy, meaning that ignition can be achieved easier. High  $\phi$ , large  $B_{st}$  (fast vaporization

rate), and small droplet sizes will all give a smaller quenching distance. When the droplets sizes are small or significant, the flame speeds (laminar or turbulent) are used in the calculation of  $d_q$  account for the chemical reaction rates [18]. Later literature reviews will show why this ignition model may not be appropriate and descriptive for modern gas turbine combustors.

Before droplets can vaporize quickly, they first need to approach a boiling temperature. When the combustor is already burning and temperatures are high, droplets can quickly reach this fast vaporization condition, and droplet heat-up may not be important. However, during start-up of gas turbine engines, the temperature of surrounding gas is usually much lower than 1000 K, as can be seen in Figure 1.3-3. For cold start and high-altitude ignition, the fuel temperature is ~100-200 K below the initial boiling point for most jet fuels. The rate of droplet heating can be a significant process that is not accounted for in Lefebvre's correlation.

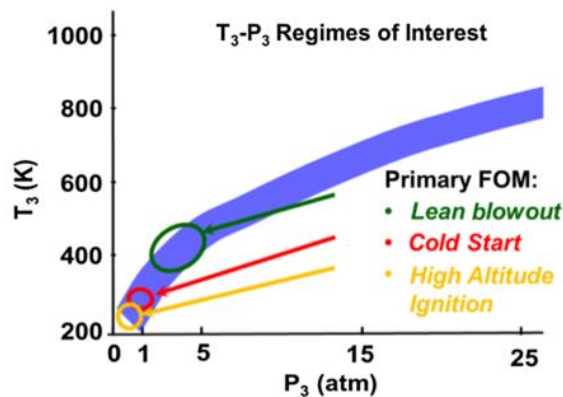


Figure 1.3-3. The range of combustor inlet conditions for primary figure of merits (FOM) that include lean blowout, cold start, and high-altitude ignition, adapted from [4].

### *1.3.2 Forced ignition*

The jet engine ignition studies described in the previous section relied primarily on measurements of lean light off limits in jet engines or combustor rigs. Only a few studies have explored the details of the forced ignition process in conditions like those found in turbine engine combustor. Most forced ignition studies that have utilized advanced techniques such as optical diagnostics or computational modelling to explore the physics of forced ignition have focused on premixed and/or quiescent conditions.

As discussed in §1.2, the spark kernel in a gas turbine combustor will need to travel through a region with little to no fuel before interacting with a flammable mixture. The requirement for the spark kernel to interact with air prior to flammable mixture makes the ignition process in a gas turbine engine different from other configurations, such as the ignition process in a spark ignition (SI) engine, in which the spark kernel is generated within the flammable mixture as shown in Figure 1.3-4.

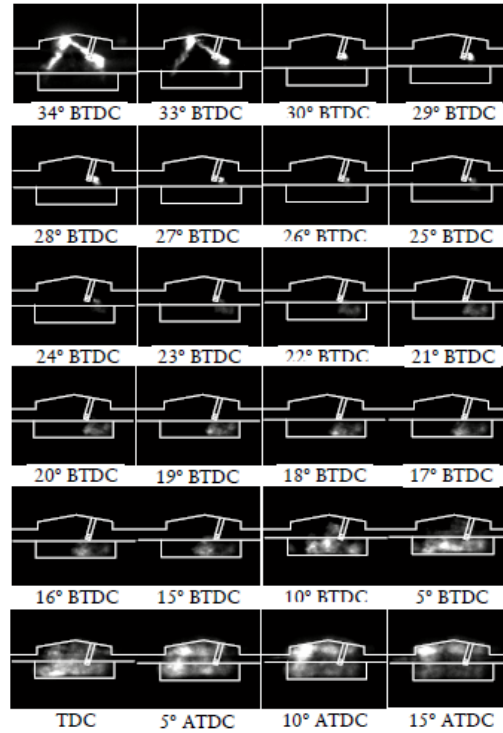


Figure 1.3-4. Combine PLIF and emission signal of an ignition sequence in an SI direct injection (DI) engine [20]. TDC stands for top-dead-center. A and B stands for after and before. A spark is generated at 34° BTDC. The angles are the crank angles.

The reason that the spark kernel can be ejected from the igniter is due to the special configuration of the igniter. In an electrode gap type spark plug, the sparks are generated in between the electrode gap. The sparks will expand in all directions due to high pressure induced by high temperature. However, the spark will not be travelling with a bulk velocity (unless in a convecting flow). Figure 1.3-5 [21] shows a CFD simulation of a spark generated from two electrodes. The spark is expanding and traveling downstream in a convecting flow.

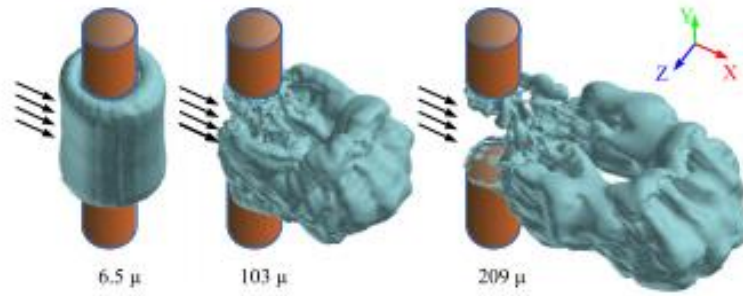


Figure 1.3-5. CFD simulation of a spark discharge from two electrodes in a convecting air flow [21].

Jet engine combustors generally employ surface discharge igniters [22]. There are two types of surface discharge igniters: one is the flush fire igniter and the other is the sunken fire igniter. The primary difference between the two types of igniter is whether the central electrode and the grounded electrode is separated by an air gap or not. The insulator is coated with semiconductor materials to facilitate breakdown [5]. For the sunken fire igniter used in the current research, the grounded electrode is made to be taller than the central electrode, such that the expanding hot gas will be directed away from the igniter. The igniter on a gas turbine engine will operate repeatedly for a fixed duration; generally lightoff should occur within this time period. The energy and repetition rate of the sparks are controlled by an external circuit (the exciter) that supplies electricity to the igniter.

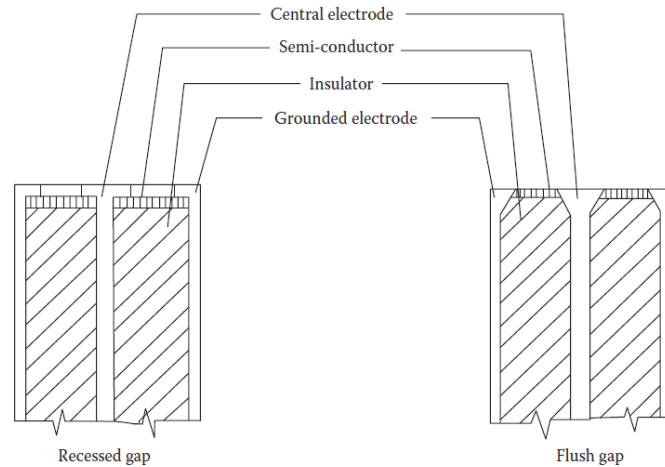


Figure 1.3-6. Cross-sections of the two types of surface discharge igniters [22]. Left: Sunken fire igniter with recessed gap; Right: Flush fire igniter with flush gap.

This spark kernel ejection process gives the kernel a structure like a pulsed jet. More discussion on the pulsed jet like structure is given in §2.1. In Sforzo's dissertation [23], an optically accessible facility was developed to understand the ignition of methane/air mixtures with a gas turbine type ignitor in a two-dimensional mixing flowfield. This ignition rig used a splitter plate to separate the combustible flow from an air flow with little to no fuel. The spark kernel had to first travel through the air gap before reaching the combustible flow. The width of the air gap was adjusted by repositioning the splitter plate. The parameters that were controlled include the splitter plate height, the average velocity of the cross flow, the temperature of the crossflow, and the equivalence ratios of the combustible flow and the near-kernel flow. This study compiled a large number of ignition probabilities at different conditions, and a linear regression analysis was used to understand the relative importance of each parameter. A tornado chart of the t-ratio of the various terms used to correlate the data is shown in Figure 1.3-7. The width of the splitter plate

( $h_{splitter}$ ) turns out to affect the outcome of ignition most, followed by the temperature of the flow.

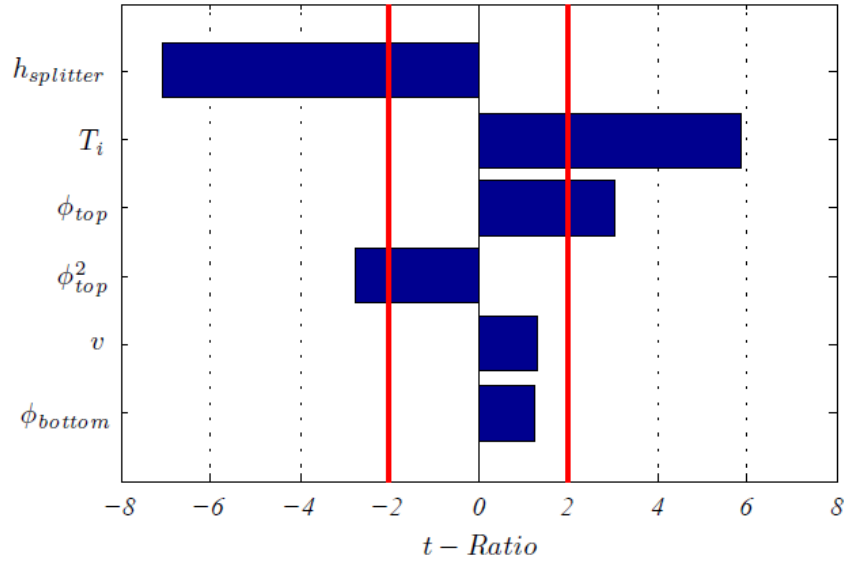


Figure 1.3-7. t-ratio from a multivariable linear regression model for predicting ignition probability [23].

Based on the turbulent entraining kernel structure, Sforzo used a perfectly-stirred reactor model to understand the effect of entrainment and chemical reactions on ignition. The author then used a support vector machine (SVM) to analyze a large number of simulations and classify conditions for which ignition would occur. The success in using the model to predict the experimental results shows the validity of using the PSR to simulate the forced ignition process.

#### 1.4 Thesis objectives and organization

The general objective of this dissertation is to understand the initial ignition process of forced ignition for liquid fuels. The general objective can be divided into two more specific



sub-objectives. The first sub-objective is to understand the effect of fuel chemistry on forced ignition. Autoignition studies of jet fuels typically employ initial temperatures of 800-1300 K. The instantaneous temperature of the ignition kernel when interacting with the fuel can be well above 2000 K. At such high temperatures, chemical reactions can deviate from those at lower temperatures. The second sub-objective is to understand the effect of liquid fuel sprays on the forced ignition process. In many combustion studies involving droplets, the heating phase of the droplets is often assumed negligible, and the combustion processes are controlled by the vaporization rate. This is a reasonable assumption when the combustor temperature is high. However, for forced ignition in turbine engines, where ambient temperatures are often insufficient to vaporize the fuel, ignoring the droplet heating can mean neglecting an important piece of physics.

The remaining portions of this thesis are divided into six chapters. Chapter 2 provides additional background information on the structure of a pulsed jet, which in many ways resembles the flow created in the post-breakdown conditions of a jet engine ignitor. It also provides basics on one of the diagnostic methods employed in the thesis, planar laser induced fluorescence. Next, Chapter 3 introduces the approaches, both experimental and modelling, taken in studying forced ignition of alternative jet fuels. The results of the thesis are presented in the next three chapters. Chapter 4 describes the experimental findings from high-speed, imaging diagnostics employed to understand the initial kernel development using various fuel under prevaporized conditions. Chapter 5 covers experiments and analysis of ignition of prevaporized fuels that identifies the effect of chemical differences among fuels. Chapter 6 extends the work to experiments on forced ignition of liquid fuel sprays and reduced order modeling of the interactions between a hot spark kernel and

droplets that lead to successful forced ignition. Finally, Chapter 7 summarizes the contributions and impacts of this thesis work, and provides recommendation for future works.

## **CHAPTER 2:**

### **BACKGROUND**

The two sections in this chapter introduces the structure of a pulsed jet and the planar laser induced fluorescence (PLIF). The spark kernels ejected from the sunken fire igniter are pulsed jets of high temperature air. An understanding of the pulsed jet structure is helpful in analysing the forced ignition process. PLIF is a commonly used technique in combustion diagnostics.

#### **2.1 Vortical structure of a pulsed jet**

As indicated previously, the spark kernels generated by a sunken fire igniter exit the igniter cup like a pulsed jet. Therefore, it is helpful to have a basic idea of the physics related to a pulsed jet. The goal here is to highlight the entrainment nature of a pulsed jet and the trajectory of a pulsed jet in a cross-flow. As the pulsed jet is ejected, the strong shear between the ejected fluid and the surrounding fluid will induce a “roll-up” structure [24]. A direct consequence of this roll-up structure is the entrainment of the surrounding fluids. The experiments performed by Oclay and Krueger [25] showed clearly this roll-up structure and the entrainment. In their experiments, the velocity of a pocket of dyed fluid in the nozzle is controlled such that the pressure used for pushing the fluid increase and then decrease. They defined a normalized time  $t^*$  by dividing by the time during which pressure is applied to push the fluid out of the nozzle. The rise and decay times of the pressure pulse were also controlled.

Figure 2.1-1 shows the fluorescence of the pulsed jets through the jets' center plane for two different jet velocity profiles. The jets are marked by white colors. The entrainment of the surround fluid (dark) by the two vortex pairs are clearly shown. The differences in the top and bottom rows show that the differences in the velocity profile can induce different entrainment behaviors.

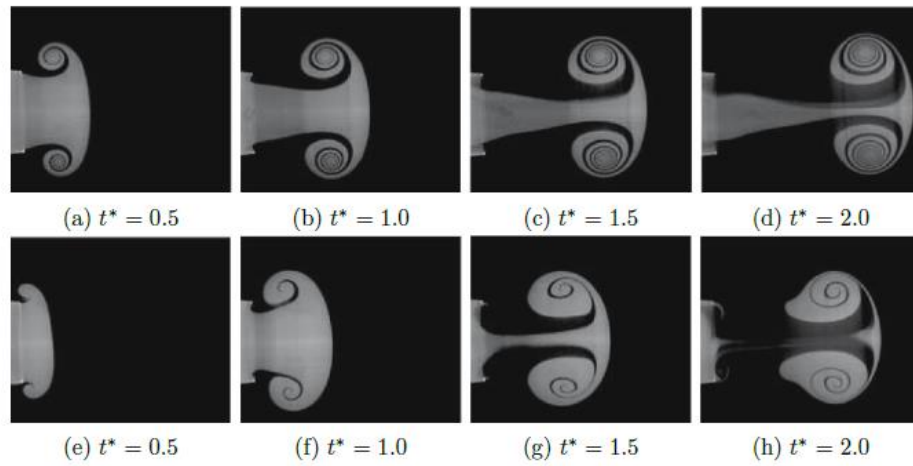


Figure 2.1-1. The fluorescence image through the pulsed jets' center planes. The top row shows a fast rise in the pressure driving the pulse and then a slow decay in the pressure. The bottom row shows the opposite case, in which the pressure rises slowly and decays quickly. Adapted from [25].

The kernels created in a combustor are ejected into the combustor and convected downstream through the cross-flow. The trajectories of the ejected kernels determine when they will interact with the flammable mixtures. Johari [26] studied pulsed jet trajectories in cross-flows based on the momentum ratios between the jet and the cross flow. The jet trajectories were given as

$$\frac{y}{d} \propto \left( \sqrt{\frac{\rho_j U_j^2}{\rho_{cf} U_{cf}^2}} \times \frac{x}{d} \right)^{1/4} \quad (4)$$

where  $\rho_j$  is the density of the jet,  $\rho_{cf}$  is the density of the cross flow,  $U_j$  is the velocity of the jet,  $d$  is the diameter of the nozzle, and  $U_{cf}$  is the velocity of the cross-flow. From this equation we can see that for a spark, the temperature of the fluid in the spark is high, and the density is therefore low. For a lower density, the same change in  $x$  will give a smaller change in  $y$ . This equation can also be used to estimate the jet velocity.

## 2.2 Planar Laser Induced Fluorescence (PLIF)

PLIF [27, 28] is a laser-based technique that uses a laser sheet at a wavelength chosen to excite specific species to an upper energy level which can then decay through spontaneous emission. Figure 2.1-1 is an example of using PLIF where a specific dye is used as the target species. For combustion diagnostics, certain species of interest can be excited to fluoresce. One of the species of special interest in combustion is the OH radicals, and the OH radicals are targeted for this research (OH PLIF). A microscopic description of the laser induced fluorescence (LIF) is shown in Figure 2.2-1.

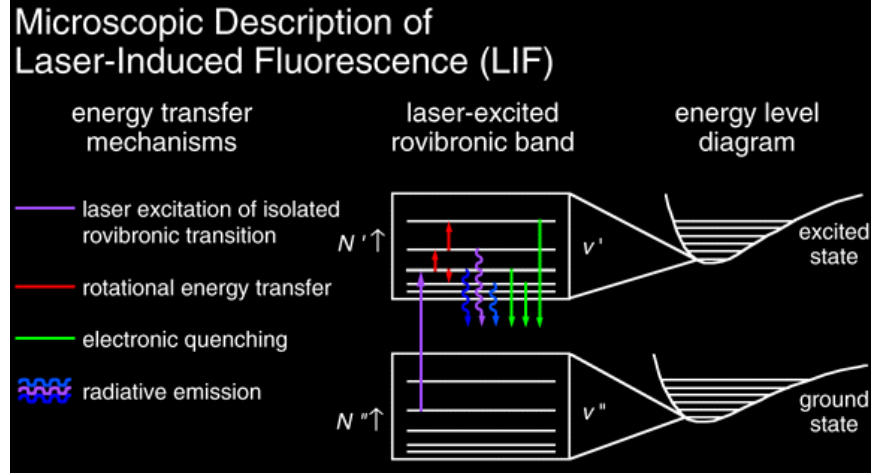


Figure 2.2-1. Energy level diagram of LIF [29].

The fluorescence equation can be used to quantitatively relate the recorded fluorescence signals to the physical fluorescence process. The fluorescence equation is

$$S_f = \frac{E_p}{A_{las}} \times gB \times N_{abs} f_{v''j''} \times \frac{A}{A + Q} \times \eta_c \quad (5)$$

where  $S_f$  is the recorded fluorescence signal per volume,  $E_p$  is the laser pulse energy,  $A_{las}$  is the cross-sectional area of the laser sheet,  $g$  overlap integral of the absorption and laser line shapes,  $B$  is the Einstein coefficient for absorption,  $N_{abs}$  is the number density of the target species,  $f_{v''j''}$  is the population fraction of the absorbing rotational-vibrational levels,  $A$  is the spontaneous emission rate,  $Q$  is the electronic quenching rate, and  $\eta_c$  is the efficiency of the optics. Through using the fluorescence equation, the species concentrations [30], temperature [31, 32] can be measured.

## **CHAPTER 3:**

### **APPROACH**

This chapter describes the methods employed in this thesis for studying forced ignition of alternative jet fuels. First, the ignition facility is described, which employs a readily modellable, optically accessible test section. Next, the chapter describes the fuels provided by National Jet Fuel Combustion Program (NJFCP). These fuels include conventional jet fuels, alternative jet fuels, and surrogate fuels. Then, the measurement approaches used to characterize the ignition process and flow conditions are presented. Finally, a modelling approach used to analyze and interpret the ignition results is described. For gaseous fuel, a constant-pressure, ideal-gas perfectly stirred reactor (PSR) is used in two stages to simulate the two stages of ignition. This PSR model will be referred to as the ignition kernel model. A droplet heating and vaporization model is then coupled to the PSR model to study the role of droplet heating and vaporization on ignition kernel dilution and heat release.

#### **3.1 Ignition facility**

The ignition facility used for this dissertation is inherited from a previous research, studying forced ignition of methane/air mixture. This facility is designed to test forced ignition in turbine engine-like environment. In gas turbine combustors, igniters are generally placed near the walls of the combustors, so that the generated spark kernels need to traverse through a region of flowing air with little to no fuel before reaching combustible mixtures. The rest of this section will describe the modified experimental facility designed for prevaporized and liquid jet fuel testing, respectively.

### 3.1.1 Prevaporized fuel ignition facility

Figure 3.1-1 show the ignition facility for prevaporized fuels. The facility was used to recreate important flowfield conditions near igniters in actual gas turbine combustors.

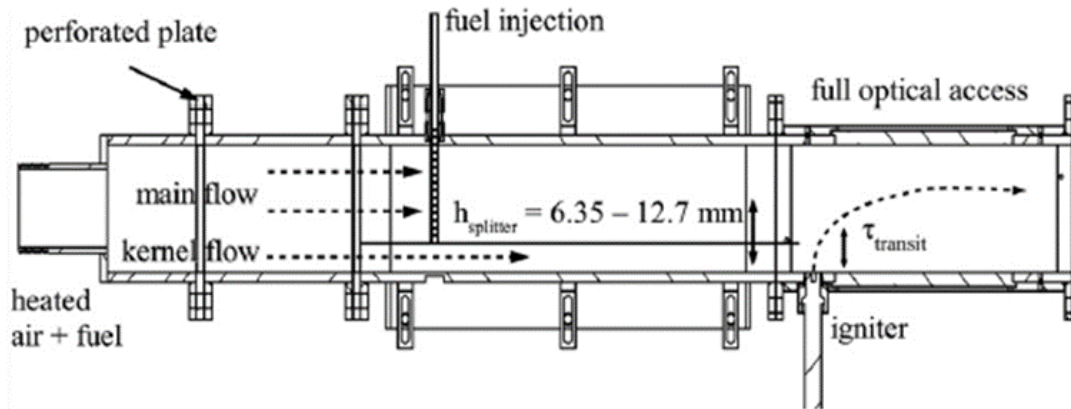


Figure 3.1-1. Schematic of test facility for prevaporized fuels, adapted from [23].

The dashed square box highlights the test section where ignition events were observed. The height, width, and length of the test section are 54.0, 85.7, and 215.9 mm, respectively. The walls of the test section are equipped with quartz windows, allowing full optical access to the test section. Inflow air was preheated to 478 K and regulated to target a 12 m/s mean flow velocity in the test section. A perforated plate after the inlet is used to produce a uniform flow velocity. Downstream of the perforated plate, a 0.635 mm thick steel plate separates the heated air flow into an upper main flow and a lower kernel flow. The main flow is fed a prevaporized fuel and carrier air gas mixture through three fuel-injection bars spanning across the main flow path. The fuel injection bars are placed ~70 cm upstream of the ignitor, allowing thorough mixing between air in main flow and vaporized fuel/air mixture. The kernel flow is pure air flow. The test section features full quartz windows on the sides and small windows on the top and bottom for optical access. The height of the



splitter plate is adjustable between 6.35 and 12.7 mm above the floor of the test section. The splitter is fixed into the side walls. The height of the splitter plate is adjusted by adjusting the height of the side walls. In this study, the splitter plate is set at 6.35 mm.

A commercial sunken-fire igniter studied previously [9,13], produced sparks with a nominal deposition energy of 1.25 J/spark at a frequency of 15 Hz. After each electrical discharge, the resulting high temperature, high pressure air in the cavity ejects into the cross-flow. The time between discharges is sufficiently large such that all remnants of the high temperature kernels or ignited flames are swept from the test section before the next discharge (and there is no flameholding in the test section). The top surface of the igniter is raised 3.18 mm above the test section floor to improve ignition probability.

To test gaseous fuels, the liquid fuel first needs to be prevaporized prior to entering the test facility. In addition, it is important to prevent recondensation of the vaporized fuel. To achieve fuel vaporization, a Bronkhorst controlled evaporator mixer (CEM) is used. A stream of liquid fuel and a stream of air are sent into the CEM. To avoid fuel condensation, the temperature of the flowing air that carries the vaporized fuel is set to be 477.6 K. The air flow temperature cannot be too high, or it might lead to fuel pyrolysis and chemistry occurring prior to encountering the high-temperature spark kernel. The tubing schematic of the fuel delivery system is shown in Figure 3.1-2. Liquid fuels are filled into a cylinder. The cylinder is then pressurized with industrial grade nitrogen at ~13.8 bar. Temperatures of the fuel and air when entering the test section are monitored. The test conditions are listed in Table 1. The nominal velocity of air flow is calculated based on the volumetric air flow rate and the area of the test section.

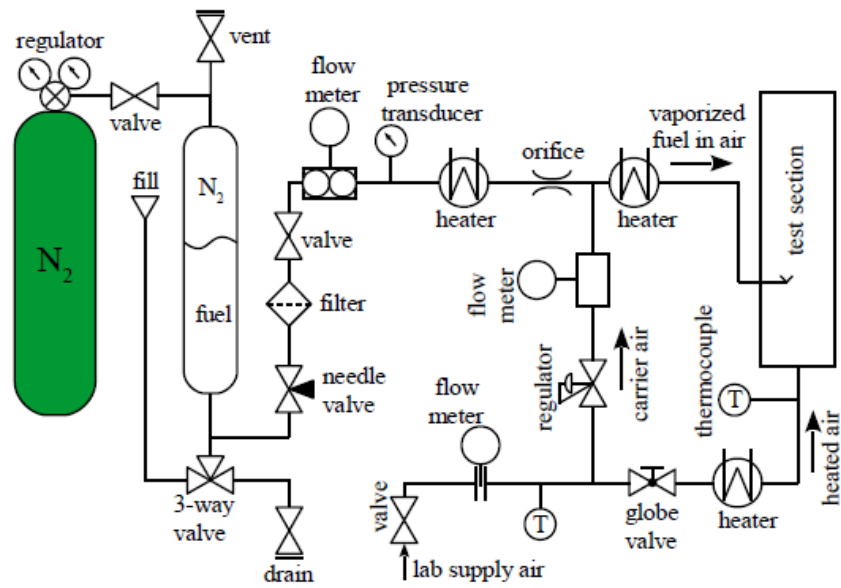


Figure 3.1-2. Schematic of fuel and air delivery system.

Table 1. Test conditions for prevaporized fuels.

Nominal air velocity	12 m/s
Air temperature	477.7 K
Fuel Temperature	470 K
$\phi$	0.5-0.7

### 3.1.2 Liquid Fuel Spray Ignition Facility

To test liquid fuel sprays, the facility is modified to allow the inclusion of a spray nozzle. Schematic of the modified rig for spray ignition is shown in Figure 3.1-3.

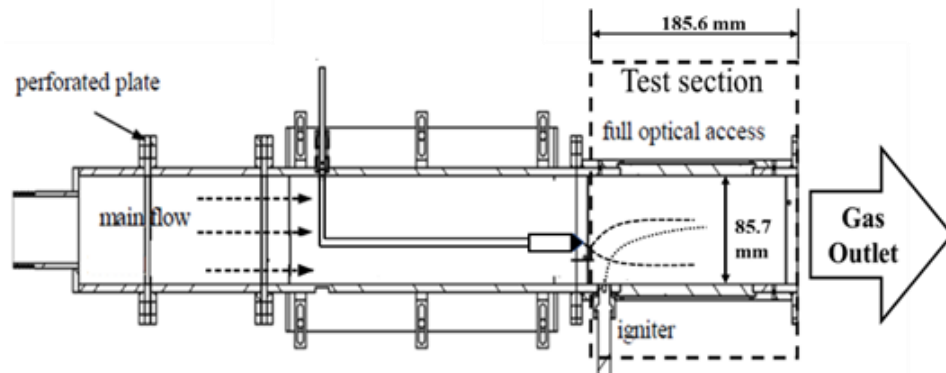


Figure 3.1-3. Schematic of test facility modified for liquid fuel spray, adapted from [23].

Compared to the facility in Figure 3.1-1, the modified facility replaces the gaseous fuel injection system with a liquid fuel injection system; no changes were made to the test section or the perforated plate used to laminarize the flow. The liquid fuel supply system is shown in Figure 3.1-4. It is a modification of the gaseous fuel supply system shown in Figure 3.1-2. Since the liquid fuels do not need to be vaporized, the fuel vaporizer is removed, and liquid fuels are directly fed into the test section.

A Hago M1 nozzle is used to create the spray. While the Hago M1 nozzle is advertised as a solid cone atomizer, it is in fact a pressure-swirl atomizer. However, unlike a classical pressure-swirl atomizer, it does not produce a hollow cone spray [33]. The Hago atomizer has an orifice diameter of 0.254 mm. The atomizer tip is positioned 15 mm above and 5.0 mm upstream of the igniter, which is located along the bottom wall of the test section. Both the atomizer and igniter are placed in the midplane of the rig. The relative positioning of

the atomizer and igniter is chosen to make sure little or no fuel is present right above the igniter to mimic the expected conditions in an engine combustor. In fact, it was noted that significant impingement of fuel at the igniter will cause unrepeatability in ignition probabilities. The absence of droplets close to the igniter is verified using the absence of visible scattering from a HeNe laser beam passing 10 mm above the igniter. Later PDPA measurement also confirmed the absence of Liquid fuel droplets above the igniter.

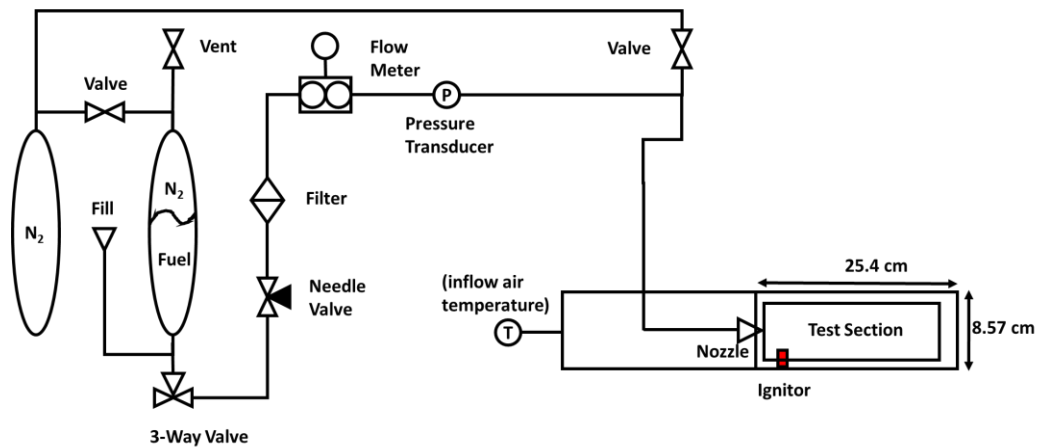


Figure 3.1-4. Liquid fuel supply for spray testing.

To understand the effect of fuel chilling on ignition, a fuel chiller is incorporated into the fuel supply system after the tests for the room temperature fuels are complete. The chiller is made with stainless steel coils immersed in polyglycol/water mixture. The fuel lines are insulated to reduce fuel warming prior to injecting into the test section. The chiller can chill the fuel down to  $-27\text{ }^{\circ}\text{C}$  when entering test section. The test conditions for fuel spray ignition are given in Table 2.

Table 2. Test conditions for liquid fuel spray ignition.

Nominal air velocity	10 m/s
Air temperature	300 K
Fuel Temperature	297 K /246 K
$\phi$	0.55

### 3.2 Description of Jet Fuels

The fuels tested in this work were provided by the National Jet Fuel Combustion Program (NJFCP). The fuels are grouped into three categories. Category A fuels contain three conventional jet fuels. A1 is JP-8, which is a widely used, versatile fuels for military vehicles. JP-8 can also serve as a diesel fuel replacement. A2 is jet-A, which is used for commercial airlines. A3 is JP-5, which is a jet fuel commonly by aircrafts on an aircraft carrier. Due to the fuel is stored on aircraft carriers, JP-5 has higher flash point than the other two A fuels.

The second category is the category C fuels. These fuels were designed to have properties at the limits of the requirements for current jet fuels, or to examine the impact of fuels with properties unlike typical distillate fuels, e.g., narrow boiling point ranges and less fuel complexity. This category also includes some current alternative jet fuels or alternative fuels blended with conventional jet fuels. The C1 fuel is composed primarily of C-12 and C-16 highly branched isoalkane (99%), and it has a low cetane number. C2 is a mix of iso-paraffin and trimethylbenzene, and this composition gives C2 a bimodal

distillation curve. C3 is designed to have high viscosity at jet fuel specification limit. C4 is C1 blended with C-9 to C-12 isoalkanes so that the boiling characteristics of C4 is like that of jet fuels. C5 is a fully formulated fuel with narrow boiling range, i.e., C5 boils at a single temperature like a pure fuel. C7 is designed to have high cycloparaffin content. C8 contains high aromatic content. C9 is composed of 100% hydro-processed esters and fatty acids (HEFA) fuel, and it has the highest cetane number that is achievable by any 100% HEFA fuel.

The third category are the surrogate fuels. These fuels are composed of a limited number of components that simulates real fuel behaviors. Three surrogate fuels are tested. Surrogate 1 (S1) is composed of 59.3% of n-dodecane, 18.4% of iso-octane, and 22.2% of 1,3,5 trimethylbenzene. Surrogate 2 (S2) is composed of 52.6% of n-hexadecane, 25.1% of iso-octane, and 22.2% of 1,3,5 trimethylbenzene. Technical grade n-dodecane (nD) is composed of 95% of n-dodecane and 5% of other straight-chain alkanes. Table 3 gives a summary of the fuel descriptions. More information fuel properties and compositions are given in Appendix A.

Table 3. Brief description of tested fuels.

<i>Fuel Name</i>	<i>Fuel Description</i>
<i>A1</i>	JP-8
<i>A2</i>	Jet-A
<i>A3</i>	JP-5
<i>C1</i>	94.5% of C12 and C16 iso-paraffin, low cetane number
<i>C2</i>	Primarily iso-paraffin + trimethylbenzene, bimodal distillation curve
<i>C3</i>	JP-5 blended with farnesene, high viscosity fuel
<i>C4</i>	C1 blended with C9 to C12 isoparaffin, simulates Jet-A boiling characteristics
<i>C5</i>	Fully formulated fuel, narrow boiling temperature range
<i>C7</i>	Blended, maximum achievable cycloparaffin (~62% vol)
<i>C8</i>	Fuel with high aromatic content
<i>C9</i>	Fully synthetic fuel with highest Cetane number
<i>S1</i>	59.3% of n-dodecane, 18.4% of iso- octane, and 22.2% of 1,3,5 trimethylbenzene
<i>S2</i>	52.6% of n-hexadecane, 25.1% of iso-octane, and 22.2% of 1,3,5 trimethylbenzene
<i>nDodecane (nD)</i>	95% of n-dodecane, 5% of other n- alkanes

### 3.3 Ignition probability measurement

To characterize the fuel composition effects on ignition, single-event probabilities are measured. Many factors can influence the outcome of ignition, including chemical reaction rates, variation in the spark kernel creation and ejection process, the turbulent behavior of the kernel interaction with the cross-flow, and variations in the spray distribution due to differences in fuel physical properties. Assuming systematic variation

in temperature and aerodynamic effects are consistent for all fuels, large enough statistics will reveal differences in ignition due to the fuels' chemical and physical properties.

### *3.3.1 Diagnostic Approach*

A commercially available sunken fire igniter operating at 15 Hz, powered by a Unison ignition exciter, is used to generate the sparks needed for ignition. Each spark releases approximately 1.25 J. The ignition events are captured by a Photron SA3 camera with 8-bit digitization. The camera's field of view captures a portion of the test section from the igniter to 15 cm downstream of the igniter. The unfiltered camera records broadband emission. The camera is synchronized to spark events via external TTL signals generated by an SRS DG 535 digital delay generator. A timing diagram for a spark event and its recording is depicted in Figure 3.3-1. The reference signal,  $T_0$ , is triggered by a photodiode signal of the spark emission. A 2 ms delay is set on the delay generator to prevent the camera from recording the emission from the spark plasma. Each camera exposure lasts for 5 ms. Therefore, a successful ignition is defined as the presence of chemiluminescence after 2 ms past the spark discharge. A sample image of a captured ignition event is shown in Figure 3.3-2.



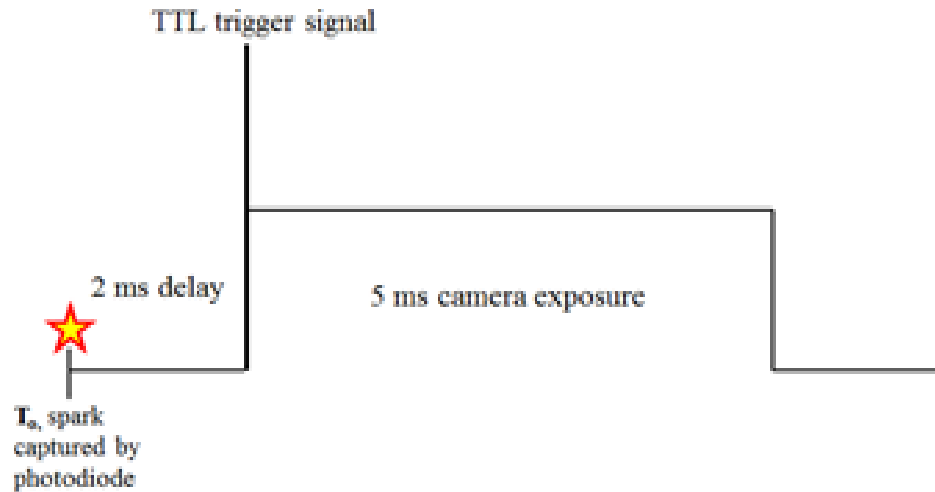


Figure 3.3-1. Timing diagram for measurement of ignition probability.



Figure 3.3-2. A sample image of a successful ignition event with room temperature fuel spray, with the camera exposure synchronized according to timing signals in Figure 3.1-1.

### 3.3.2 Probability and uncertainty calculation

Thousands of ignition events are acquired for each fuel. An ignition event is defined as the process of a spark discharge interacting with a flammable mixture. Sparks will lead to self-sustaining flames in successful ignition events, whereas no self-sustaining flame is

present for a failed ignition event. The exciter controls the ignition to generate sparks at 15 Hz for 8 s. This repetition rate combined with the cross-flow velocity ensures that subsequent ignition kernels, nor any flames produced by them, can not interact with each other; thus each ignition event can be treated as independent. A run is defined as all the spark events in an 8 s operation of the ignitor. After the 8 second run, the repetition rate decrease from 15 Hz to 1 Hz. For each run, ~110-114 ignition events are captured. The success/failure nature of independent ignition events means the ignition statistics can be characterized through binomial statistics. The ignition probability is calculated as

$$P = \frac{N_{success}}{N_{total}} \quad (6)$$

where  $P$  is the successful ignition probability,  $N_{success}$  is the number of successful ignitions, and  $N_{total}$  is the total number of attempts. The 68% uncertainty bound for a binomial distribution is calculated as

$$\varepsilon_p = \sqrt{\frac{P(1 - P)}{N_{total}}} \quad (7)$$

The ignition probabilities acquired at different conditions can have largely different absolute ignition probabilities. For easy comparison between different test conditions, ignition probabilities of different fuels are scaled with respect to that of fuel A2, which is the standard Jet-A fuel. The relative probability  $P_r$  is

$$P_r = \frac{P - P_{A-2}}{P_{A-2}} \quad (8)$$

The uncertainty of the normalized probability can be calculated through uncertainty propagation as

$$\epsilon_{P_r} = \sqrt{\left(\frac{\epsilon_P}{P_{A-2}}\right)^2 + \left(P * \frac{\epsilon_{P_{A-2}}}{P_{A-2}}\right)^2} \quad (9)$$

### 3.3.3 Repeatability

Statistically significant data is based on hundreds to thousands of sparks tested for each of the 14 fuels. Producing such a large data set required conducting experiments in a number of different trials on different days. To ensure data acquired on different days were repeatable, some of the fuels were retested on multiple days. Figure 3.3-3 shows repeatability results with fuel A2 and C1 on two days. For both C1 and A2, data taken on day 1 is within the uncertainty of data taken on day 2.

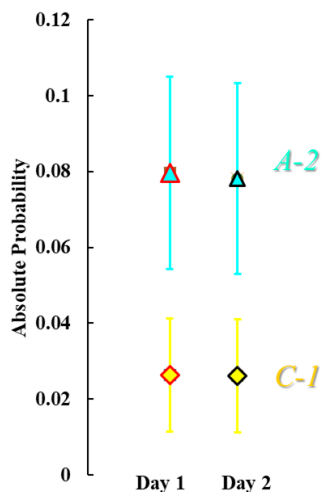


Figure 3.3-3. Absolute probabilities for fuels A2 and C1 of room temperature ignition acquired on two different days.

### 3.4 High speed diagnostics

To better understand how spark kernel interacts with flammable mixtures, high speed diagnostics are employed. The evolution of the ignition kernels was characterized by high speed images acquired nearly simultaneously from three imaging systems: a schlieren setup, a planar laser-induced fluorescence (PLIF) system tuned to excite and detect the OH radical, and a ultraviolet (UV) emission system designed to capture chemiluminescence from electronically excited OH, denoted as OH\*. A small time delay between the OH PLIF and chemiluminescence systems was used to prevent interferences from the PLIF signal on the chemiluminescence image. The light sources used for the OH and schlieren setups are described first, followed by the imaging systems used to collect the three signals.

#### 3.4.1 Schlieren Imaging

Schlieren imaging is a commonly used technique in diagnosing compressible and reacting flows. The most common version of this technique works by first passing

(nominally) parallel light through the region of interest. This light is then focused to a point or a line and blocked by an opaque object before entering the viewing device. The variation in density gradient experienced by the light causes refraction. The refracted light is captured by the viewing device. The hot ignition kernel was imaged with a point-blocked schlieren system to detect the density gradient between the hot kernel and lower temperature surrounding flow, as utilized in a previous work [8]. The system consisted of a point light source (a 50 watt halogen lamp passing through a 0.4 mm diameter hole), two off-axis parabolic condensing mirrors (0.5 m diameter and 1 m focal length), and an opaque point spatial filter to block unrefracted light as depicted in Figure 3.4-1.

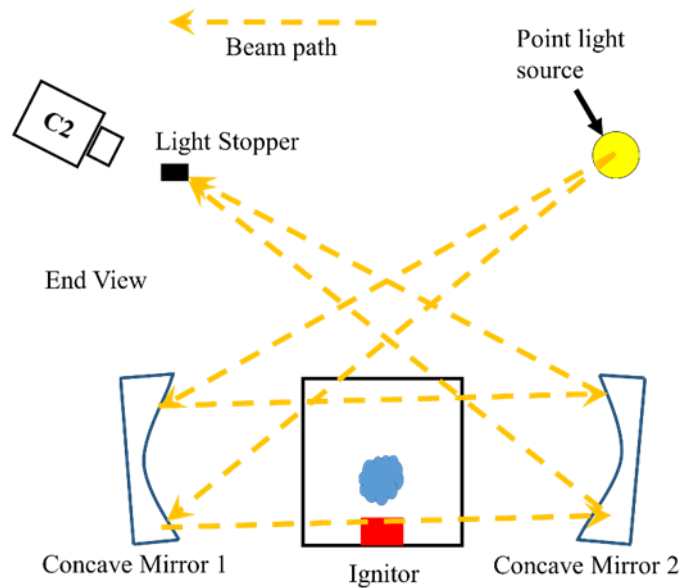


Figure 3.4-1. Profile schematic of schlieren illumination and imaging configuration (not to scale); C2 is the schlieren imaging camera.

### 3.4.2 $\text{OH}^*$ Chemiluminescence

$\text{OH}^*$  chemiluminescence provides a line-of-sight indicator of important chemical reactions occurring within the ignition kernel.  $\text{OH}^*$  is generally a good indicator of

chemical reaction zones for hydrocarbon fuels. A filter is applied to target emission from OH\*. As the filter will significantly reduce the light intensity, a light intensifier is used to enhance the image quality.

Table 4. Summary of the imaging components.

	Camera	Intensifier	Lens f, f/#	Filter center, FWHM (nm)
<b>PLIF</b>	Photron SA5	Lambert HiCATT	Cerco 45 mm, 1.8	315, 15
<b>Emission</b>	Photron SA5	LaVision IRO	Cerco 45 mm, 1.8	320, 40
<b>Schlieren</b>	Photron SA1	None	Nikon 270 mm, 5.6	None
<b>Timing</b>	Photron SA3	None	Nikon 20 mm, 4	None

### 3.4.3 OH Planar Laser Induced Fluorescence (PLIF)

An Edgewave Nd:YAG laser operating at 10 kHz, emitting approximately 50W at 532nm was used to pump a tunable wavelength Sirah Credo dye laser, which was then frequency doubled, resulting in an output of 2W of ~283 nm emission with a pulse duration

of roughly 10 ns. The laser was tuned to excite the  $Q_1(7)$  transition in the  $A^2\Sigma(v'=1) \leftarrow X^2\Pi(v''=0)$  band (also designated laser as the (1,0) band) of the OH molecule. The excitation wavelength was optimized for OH fluorescence by tuning the dye laser and observing LIF from a propane-air Bunsen flame. Fused silica lenses were used to form and direct a laser sheet approximately with  $30\text{ mm} \times 70\text{ mm}$  into the test section, illuminating the region of expected early kernel development.

#### *3.4.4 Imaging system and synchronizaton*

Three 8-bit high-speed cameras captured the individual PLIF, chemiluminescence, and schlieren signals. As the 10 kHz detection systems could not be synchronized to the 15 Hz exciter that controlled the igniter discharge, a fourth camera operating at a higher framing rate was used to determine the delay between the high-speed images and the discharge pulse. Table 4 provides a summary of the imaging components. A top view of the relative position of the four cameras with respect to the test section is shown in Figure 3.4-3. A 10 kHz TTL signal from a gate and delay generator was used to trigger the three image system cameras and the Edgewave Nd:YAG pump laser. Thus, the pump laser, PLIF camera, chemiluminescence, and schlieren cameras were synchronized.

A Photron SA5 camera (C4) equipped with a Lambert HiCATT intensifier (I2) was used to capture fluorescence from OH radicals. The PLIF camera operated in externally synchronized mode, with the intensifier synchronized to the camera frame rate. The gates of the intensifiers were set such that only the PLIF camera could capture emission from laser-induced fluorescence. The relations between the two intensifiers and the laser pulse is shown in the timing diagram of Figure 3.4-2. A bandpass filter centered at 315 nm with

15 nm FWHM was placed in front of the lens to pass red-shifted OH fluorescence in the (1,1) and (0,0) vibrational bands. During data acquisition, approximately 1 s of video was recorded at a resolution of 896×848 pixels.

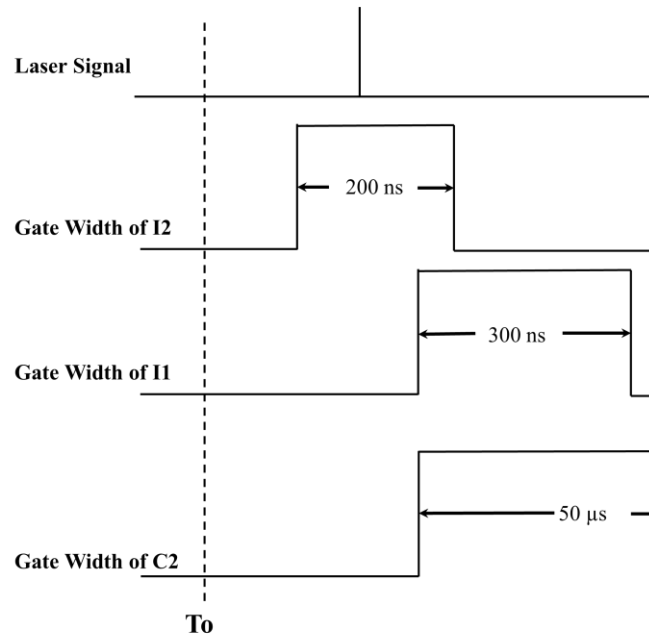


Figure 3.4-2. Timing relations of the beginning of TTL signal (To), laser signal, gate opening of intensifier for chemiluminescence camera (I1), gate opening of intensifier for the PLIF camera (I2), and gate opening of the schlieren camera (C2).

A second Photron SA5 camera equipped with a LaVision high speed IRO intensifier was used to capture emission from the kernel. The bandpass filter (centered at 320 nm) installed on the lens was used to detect primarily OH\* chemiluminescence, though any UV emission in this wavelength range is also captured. The camera and the intensifier were synchronized to the same 10 kHz signal used by the Nd:YAG pump laser and the OH PLIF system. The size of the recorded images (in pixel dimensions) was identical to the PLIF camera.



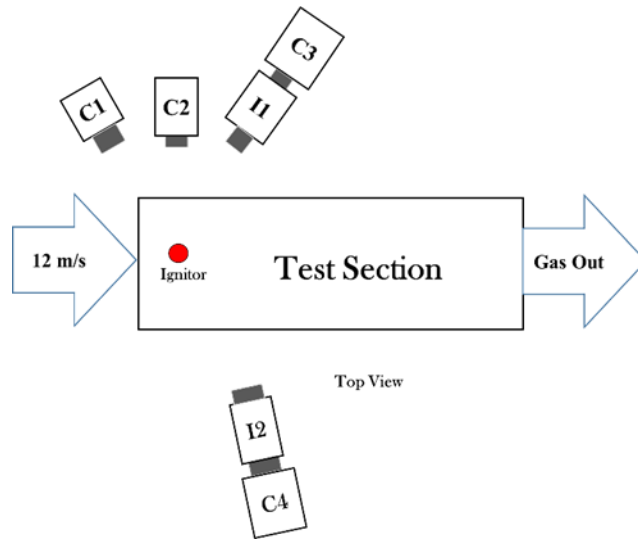


Figure 3.4-3. Top view schematic of test section with relative position of the (C1) timing camera, (C2) schlieren camera, (C3) chemiluminescence camera, and (C4) PLIF camera. intensifiers on the (I1) chemiluminescence camera and (I2) PLIF camera are also depicted.

A Photron SA1 camera, also externally synchronized to the 10 kHz triggering signal, was used to capture schlieren images, with a pixel resolution of  $704 \times 704$ . Finally, the fourth camera (Photron SA3), without spectral filtering, was used to image the emission from the plasma discharge. The resolution of this camera was  $512 \times 104$  pixels, focusing on a small field of view directly above the igniter. It was operated at 60 kHz but synchronized to the 10 kHz external TTL signal, and thus also synchronized to all the other camera systems. With its higher framing rate, the uncertainty in the time delay between the diagnostic images and the discharge event was reduced from 0.1 ms to 0.016 ms.

### 3.4.5 Image processing

#### 3.4.5.1 Kernel Velocity

The trajectory path and velocity of the hot air kernel were obtained from the high speed schlieren images. The images were first background subtracted based on an image taken before the kernel was created (i.e., before the discharge), as illustrated in Figure 3.4-4. A Sobel edge tracking algorithm was then used to track the edge of the kernel's boundary. A constant threshold value was used to ensure consistency in edge tracking. The coordinates of the kernel edge closest to the x-axis were obtained and transformed into distances from the igniter based on a calibration plate image taken prior to testing. Velocities were calculated from the differences in distances between frames.

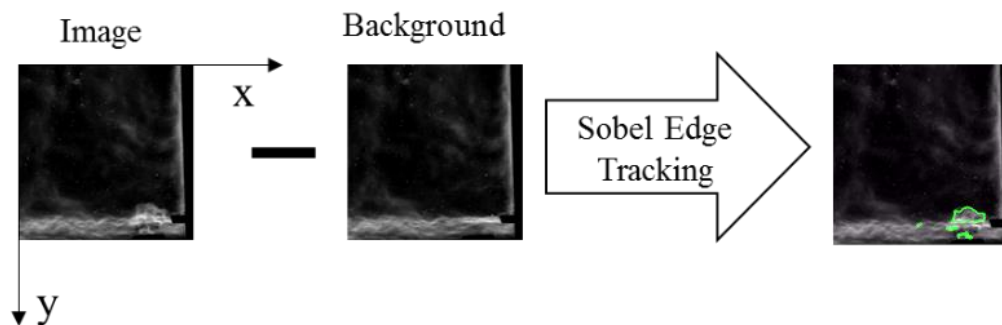


Figure 3.4-4. Depiction of edge-tracking algorithm used to obtain kernel velocities.

#### 3.4.5.2 Image Registration and Alignment

The PLIF, schlieren and chemiluminescence cameras were positioned at different angles with respect to the test section. For the images in the three cameras to be properly compared, their different fields of view and orientation need to be corrected to match. In

the beginning of each day's experiments, images of a transparent plate with equally spaced dots (2 mm spacing, 0.5 mm diameter) were acquired (Figure 3.4-5). These dots were used to dewarp the images so that images in each camera were aligned with same field of view. Since the field of view of the schlieren camera (C2, Figure 3.3-3) was positioned perpendicular to the test section, calibration images from the schlieren camera were used as the reference image for the other two cameras.

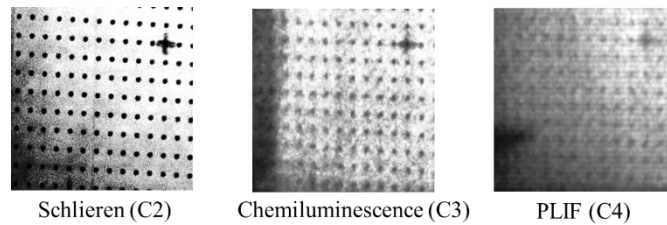


Figure 3.4-5. Calibration images acquired before experiments for registration. Schlieren camera (C2) was used as reference for chemiluminescence (C3) and PLIF (C4) cameras.

The pixel positions of the dots on each camera were determined manually. The corresponding dots in the schlieren camera and the non-schlieren camera formed matching pairs. These pairs were then used to obtain transformation matrices (using standard Matlab image processing functions), and the transformation matrices were applied to the images using a built-in dewarping function. As the positions of the dots were selected manually and the pixel areas of the dots are not negligible, uncertainties exist when aligning the dots in different images. In addition, the camera matching is based on data from the image plane defined by the registration plate. The schlieren and the chemiluminescence images, however, are line-of-sight measurements; thus the registration process should not be expected to provide excellent alignment of the images.

### 3.4.5.3 Contrast Enhancement and Gray Scale Inversion

To enhance the ability to observe spark kernel development in the PLIF and schlieren images, the contrasts of the gray scale images are linearly adjusted with constant multipliers. The constant multipliers are chosen through trial and error, such that the brightness of the kernel is enhanced without saturation. The contrast adjustment algorithm can be expressed as  $\text{new image} = \text{constant multiplier} \times \text{raw image}$ . The constants used for PLIF and schlieren are 3.0 and 2.0 respectively. The Matlab code for the image registration is provided in the Appendix B.

In addition, because human perception is better at detecting dark details on white background than detecting bright details on dark background, the images presented in the results section are inverted. The inversion is achieved through first creating a matrix with the same size as the aligned and registered images. The values in each pixel of this matrix are set to be 255, representing the maximum of the dynamic range. This matrix can be pictured as a pure white image. The original image is then subtracted from the pure white image and an inverted image is obtained.

## **3.5 Droplet distribution measurement**

For combustion phenomena involving droplets, the physical transition from liquid to gas prior to fast heat-releasing chemical reactions can have profound influence. For example, during forced ignition, the droplets will first need to be heated to its vaporization temperature. Subsequently, energy is required for vaporization. As the droplets are heated and vaporized, the ignition kernel will be quenched due to entrainment of surrounding fluids. The droplet size largely determines the heat-up time, and thus the extent of kernel

cooling. Therefore, measurement of droplet sizes can help understand the effect of physical properties on forced ignition.

The PDPA system consists of a Coherent Innova 90C Argon/Krypton laser, a TSI Flow and Size Analyzer (FSA) Model 3500, a TSI Bragg cell, a TSI TM 50 series transmitter, and a TSI RV 70 series receiver. The Innova 90C laser generates a continuous wave laser beam at ~1.2 W with two wavelengths at 514.5 nm (argon) and 647.1 (krypton). A beam splitter then separates each of the two wavelengths into two coherent beams at the same wavelength. The Bragg cell is used to create moving fringes in one of the split beams by slightly changing the frequency, so the directions of velocities can be distinguished. The transmitter emits the four beams with a focal length of 363 mm from the transmitter lens. The measurement volume created by the intersecting beams is in the shape of approximately a cylinder with 80  $\mu\text{m}$  diameter by 150  $\mu\text{m}$  length. The angle between the line of sight of the receiver and the laser beam is  $\sim 135^\circ$ , and the working distance of the receiver from the focal position is  $\sim 300$  mm. The top-down view of the relative positions of the components in the PDPA system and the data acquisition system is shown in Figure 3.5-2. The laser Doppler signal acquired by the receiver is passed to the photo detector module (PDM), which essentially samples photonic signals and transforms them into electrical signals. The flow and size analyzer (FSA) acquires these electrical signals and converts them into information about droplet sizes and velocities based on Doppler shifts. The FlowSizer software then presents these analyzed results. In addition to data presentation, the FlowSizer can also set the downmix frequency in the Bragg cell (an acousto-optic modulator), the burst threshold of the PDM, the photomultiplication of the PDM, and the signal to noise (SNR) level on the FSA. The settings of these parameters

control the range of velocities and droplet sizes, and they also help reduce noise. A listing of these parameters is given in Figure 3.5-1.

	Channel 1	Channel 2
PMT Voltage (V)	430	450
Burst Threshold (mV)	30	30
Band Pass Filter (Hz)	2 - 20 M	2 - 20 M
SNR	Medium	Medium
Downmix Freq. (MHz)	28	30

Figure 3.5-1. Select PDPA parameters.

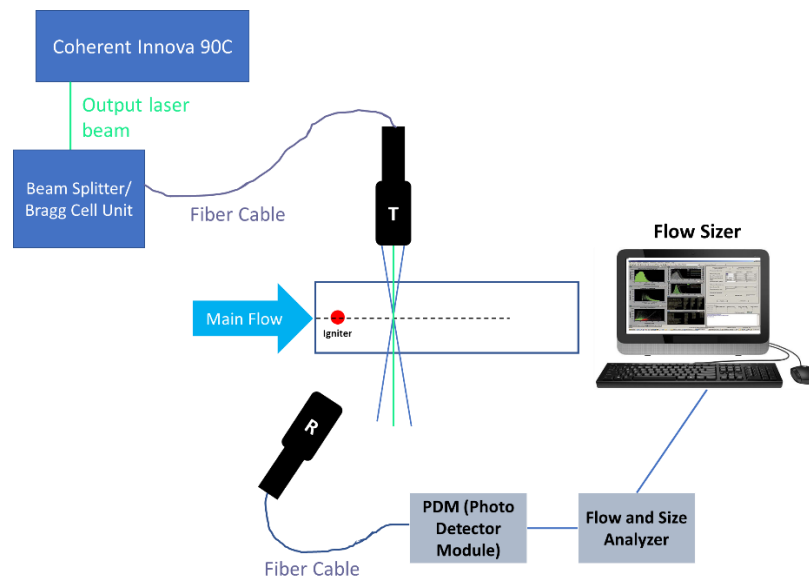


Figure 3.5-2. Top-down view of the schematic of the PDPA system setup. T is the transmitter that emits laser beams. R is the receiver that acquires laser Doppler signals.

The droplet size measurements are taken of fuel sprays at conditions in Table 2, for the fuel temperature at 294.3 K. Measurements are taken for fuels A2, C1, C3, C5, C9, and n-dodecane. The PDPA system is mounted on a three-axis Parker linear positioner controller by a Newport M3000 motion controller. Measurements are taken at three locations along the centerline of the nozzle exit, at 10 mm, 20 mm, and 30.4 mm respectively. At each centerline location, the measurements start at the centerline and move towards the bottom wall in 1 mm increments. For C3, a spanwise measurement is taken at the nozzle centerline location (10 mm). This spanwise measurement is helpful to check the symmetry of the spray and the measurements.

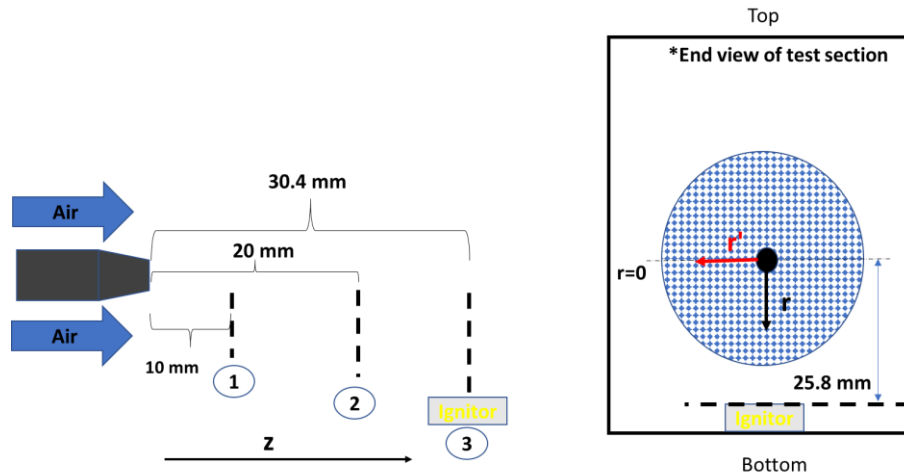


Figure 3.5-3. Location of PDPA measurements. Left: 3 centerline locations where measurements are taken. Right: Measurements are taken radially downward at each location:  $r$  is the transverse direction, and  $r'$  is the span-wise direction.

The Sauter Mean Diameter (SMD) is often used in combustion studies as a representative droplet size of a spray, as the SMD (also denoted  $D_{32}$ ) represents the ratio of the overall volume to the overall surface area. For a pressure-swirl atomizer, the empirical correlation given for SMD by Lefebvre [22] for a pressure swirl atomizer is

$$D_{32} = 2.25\sigma^{0.25}\mu_L^{0.25}\dot{m}_L^{0.25}\Delta P_L^{-0.5}\rho_A^{-0.25} \quad (10)$$

where  $\sigma$  is the surface tension,  $\mu_L$  is the kinematic viscosity,  $\dot{m}_L$  is the mass flow rate through the nozzle,  $\Delta P_L$  is the pressure drop across the nozzle, and  $\rho_A$  is the density of the surrounding air.

### 3.6 Reduced-order forced ignition modeling approach

#### 3.6.1 Two-stage perfectly stirred reactor model

In order to simulate the behavior of an entraining spark kernel, and following a previous study [8], a perfectly stirred reactor (PSR) is used to model the post discharge kernel development. In the first stage of kernel development, the kernel travels through an air layer with little or no fuel present. To model this first stage, a PSR is initialized with 1.25 J, the energy delivered to the ignitor. The volume of the PSR is set to be the volume of the cup of the sunken fire ignitor. The initial mole fraction is set to be 21% O<sub>2</sub> and 79% N<sub>2</sub>. The ambient pressure of the surrounding air is set at 1 atm, and its temperature set according to test conditions. The pressure of the PSR kernel is then allowed to expand to equilibrate with the ambient pressure. A mass flow controller is used to transport ambient fluid into the kernel, simulating the kernel growth and mass entrainment process of the kernel. The mass entrainment rate is determined from schlieren imaging of the kernel obtained experimentally. A free source chemical kinetics software, Cantera [34] (version 2.3.0), is used in the simulation. The species equation [35] solved by the PSR is



$$m \frac{dY_k}{dt} = \sum_{in} \dot{m}_{in} (Y_{k,in} - Y_k) + \dot{m}_{k,gen} \quad (11)$$

where  $m$  is mass of the PSR kernel,  $Y_k$  is the mass fraction of the  $k^{\text{th}}$  species,  $Y_{k,in}$  is the mass fraction of  $k^{\text{th}}$  species entering the PSR kernel, and  $\dot{m}_{k,gen}$  is the mass generation of the  $k^{\text{th}}$  species. The energy equation solved in a constant pressure PSR is

$$m \frac{dT}{dt} = \sum_{in} \dot{m}_{in} (h_{in} - \sum_k h_k Y_{k,in}) - \sum_{in} h_k \dot{m}_{k,gen} \quad (12)$$

where  $C_p$  is the heat capacity of the kernel,  $h_{in}$  is the total enthalpy (enthalpy of formation + sensible enthalpy) of gas entering the kernel,  $h_k$  is the enthalpy of the  $k^{\text{th}}$  species in the PSR,  $Y_{k,in}$  is the mass fraction of the  $k^{\text{th}}$  species in the PSR,  $\dot{m}_{in}$  is the mass flow rate into the kernel, and  $\dot{m}_{k,gen}$  is mass generation rate (creation/destruction) of the  $k^{\text{th}}$  species.

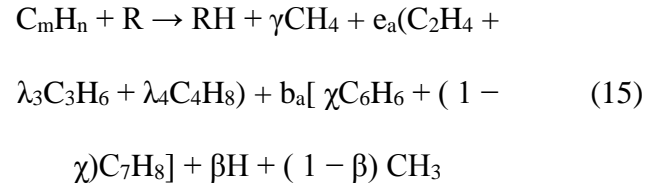
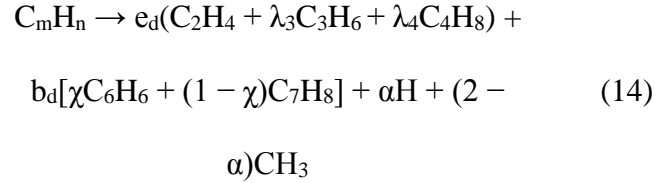
In this model, the effect of diffusive heat transfer between the kernel and the ambient air is ignored. This simplification assumes that mass entrainment and heat release have the dominant impact on the temperature of the kernel. This approximation is justifiable if one performs an order of magnitude analysis on the effect on temperature due to the heat loss rate from diffusion, the dilution from entraining cold ambient fluid, and the chemical heat release rate. Heat transfer due to diffusion is of  $\mathcal{O}(10^{-3} \text{ J/s})$ , whereas the dilution and chemical heat release rate are of  $\mathcal{O}(100 \text{ J/s})$ . The heat transfer due to diffusion can be approximate with Fourier's law, where

$$\frac{Q}{\Delta t} = -kA \frac{\Delta T}{\Delta x} \quad (13)$$

where  $k$  is the thermal conductivity,  $A$  is the area of the kernel,  $\Delta T$  is the temperature gradient, and  $\Delta x$  is the thickness of the thermal boundary layer. For typical kernel conditions,  $k \sim \mathcal{O}(10^{-3} \text{ J/m-k})$ ,  $A \sim \mathcal{O}(10^{-5} \text{ m}^2)$ ,  $\Delta T \sim \mathcal{O}(10^3 \text{ K})$ , and  $\Delta x \sim \mathcal{O}(10^{-3} \text{ J/s})$ . This gives a diffusive heat transfer rate of  $\mathcal{O}(10^{-3} \text{ J/s})$ . The order of magnitude of the dilution cooling and the chemical heat release noted above will be justified in later simulation results.

The first stage of the kernel PSR ends when the kernel starts interacting with the fuel/air mixture - a time that can be determined from the schlieren data. At this point, the ambient fluid entraining into the second stage PSR is a fuel/air mixture with an equivalence ratio that can be set to be the same as the equivalence ratio used in testing. The equivalence ratio can be calculated using the C/H ratio and molecular weight of the fuel. A conceptual model is shown in Figure 3.6-1. The Hybrid Chemistry (HyChem) fuel mechanisms [36], which were developed for the NJFCP fuel, are used. The HyChem model is a lump fuel pyrolysis model. Although all jet fuels contain a wide variety of large chain hydrocarbons, the HyChem mechanisms (Figure 3.6-2) utilize the rate limiting effect of the intermediate species after the original fuel breakdown in combustion reactions. The initial products of original fuel breakdown are limited to an important few (ethylene, propene, iso-butane, 1-butane, benzene, and toluene). USC II mechanism [37] is then used to further oxidize these intermediate products into final combustion products. The HyChem model assumes that the thermal decomposition of the fuel molecules occurs before oxidation of the

decomposition product. The original fuel breakdowns mechanisms are categorized into self-pyrolysis (C-C fission) and energetic particles attack (radical scission). The detailed fuel breakdown mechanism is shown in the reaction steps below.



where  $\alpha$ ,  $\beta$ ,  $\chi$ ,  $\lambda_i$  and  $\gamma$  are independent variables whose values depend on experimental values. The dependent variables  $e_d$ ,  $e_a$ ,  $b_d$  and  $b_a$  can be calculated from conservation of species.

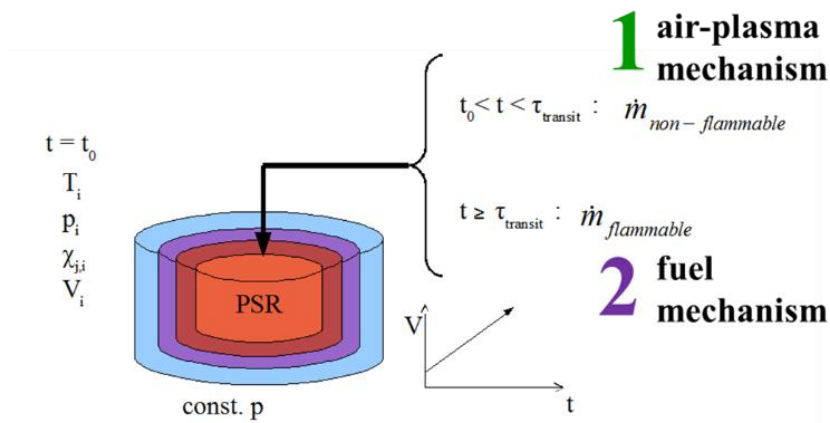


Figure 3.6-1. Setup of two stage perfectly stirred model. Adapted from [38].

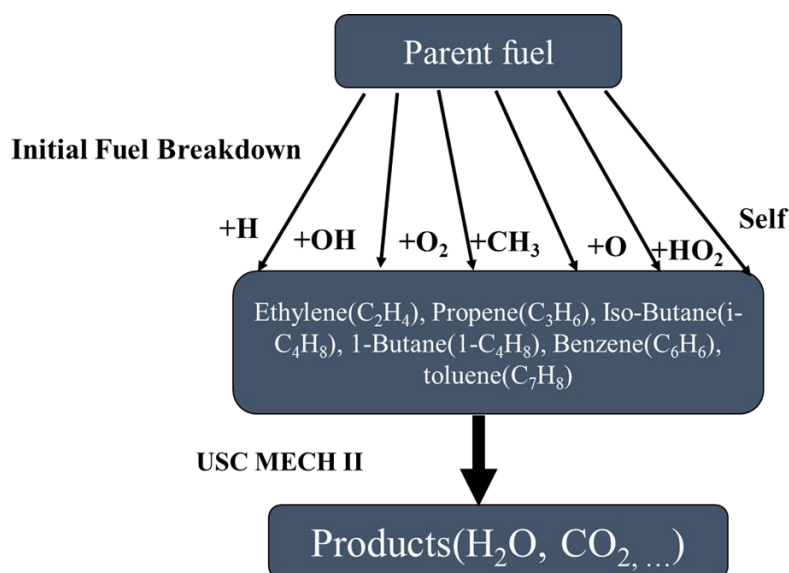


Figure 3.6-2. Schematic for hybrid chemistry approach in breaking down large fuel molecules.

### 3.6.2 *Reduced-order liquid spray ignition model.*

#### 3.6.2.1 Overall model construction

To incorporate droplet heating and vaporization, physical models for droplet heating and vaporization are used. The module that handles droplet heating and vaporization is built upon the existing perfectly stirred reactor model. The solver for the stirred reactor model is implemented in Cantera. As for droplet heating, the lump analysis model is used by assuming the droplet sizes are small. This assumption is valid as majority of the measured droplet sizes are generally less than 20  $\mu\text{m}$  and the calculated Biot numbers are less than 0.3. A conceptual model of the coupling between the PSR and the fuel heating and vaporization module is shown in Figure 3.6-3.

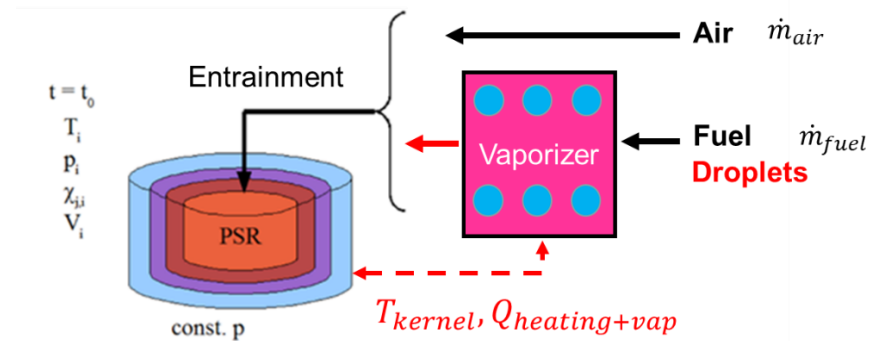


Figure 3.6-3. Conceptual model PSR modeling with droplet vaporization.

From a programming perspective, a more detailed construction of the reactor model is presented in Figure 3.6-4. The entire program is written in Python. Modular and object-oriented programming techniques are widely used in this program. Overall, the program is divided into two parts, as shown by the two dashed boxes in Figure 3.6-4. Inside the upper dashed box, this module describes the gas phase reactions solved in a constant-pressure PSR, by Cantera. The constant pressure PSR is used to model the expanding kernel, as explained in section 3.6.1. In addition to the PSR, two species reservoirs are used to contain the ambient air and the vapor fuel. The interaction between the PSR and the two reservoirs is realized through two mass flow controllers (MFC). The MFCs set the mass flow rate of substances transporting from the reservoirs to the PSR. The mass flow rate from the air reservoir to the kernel is chosen to be a constant based on kernel expansion rate data from the schlieren images. For the mass flow controller that controls gaseous fuel flow rate between the fuel reservoir and the PSR, the mass flow rate is set based on the vaporization rate calculated by the function vaporizer in the lower dashed box.

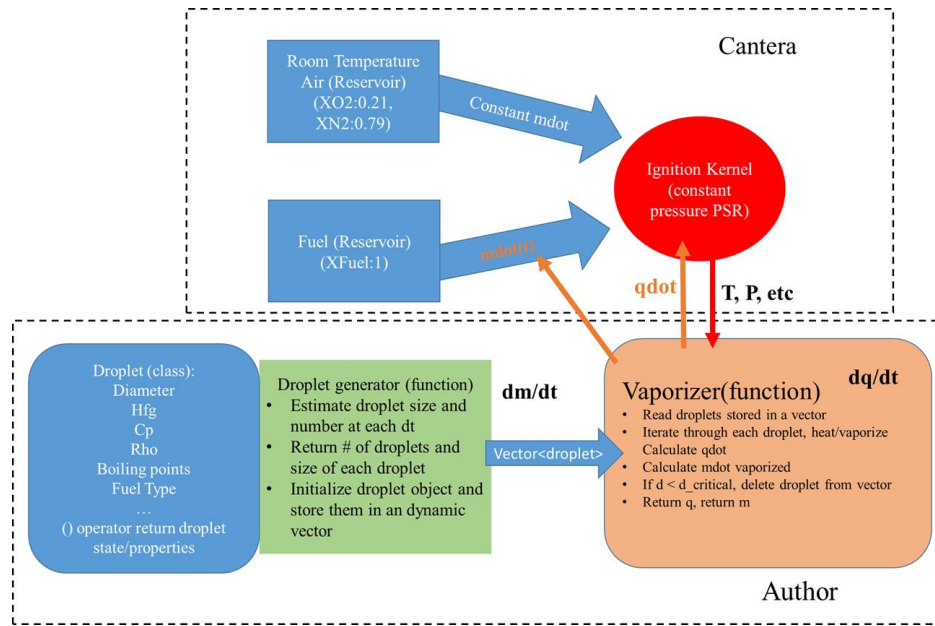


Figure 3.6-4. Descriptions of the modules used to achieve liquid droplet vaporization and chemical reaction in gas phase.

The primary objectives of this second module are to:

1. Create a class “Droplet” that stores important droplet properties, such as diameter, density, molecular weight, and so on. Each instance of the Droplet class will represent a single droplet. See droplet.py in Appendix E for a list of properties.
2. Create a function “entrainer” that generates droplets at each time step.
3. Create a function “vaporizer” that heat up the liquid droplet to their wet-bulb temperatures and vaporize the liquid droplets.

The following subsections describe the droplet entrainment module and the vaporizer in greater details.

### 3.6.2.2 Droplet Entrainment

Two vectors will need to be provided for the droplet entrainment. One vector is  $d\_arr$ , which stores the diameters of the droplet. The other vector is  $Y\_arr$ , which stores the mass fraction of each droplet diameter. The  $d\_arr$  and  $Y\_arr$  can be assigned values arbitrarily. However, a Rosin-Rammler distribution is commonly used to describe the cumulative volumetric size distribution [33]. The distribution is given by

$$1 - Q(D) = \exp\left(-\left(\frac{D}{X}\right)^q\right) \quad (16)$$

where  $Q(D)$  is the cumulative volumetric distribution (CDF),  $D$  is the droplet size,  $X$  is the characteristic size for which 63.2% of the droplets are contained in droplets with sizes less than  $X$ , and  $q$  characterizes the “spread” of droplet sizes. A large  $q$  indicates small variation in droplet size distribution, whereas as a smaller  $q$  indicates a wider spread in droplet sizes. The probability density function (PDF) of  $Q(D)$  can be obtained by taking the derivative of  $Q$  with respect to  $D$ ; the result is

$$\frac{dQ(D)}{D} = \frac{q}{D} \exp\left(-\left(\frac{D}{X}\right)^q\right) \left(\frac{D}{X}\right)^{q-1} \quad (17)$$

Given some liquid mass of  $m$ , the fraction of mass within each diameter is  $m \cdot dQ/dD$ . Now knowing the amount of mass in each size  $D$ , one can then simply distribute the fractional mass into droplets of diameter  $D$ .

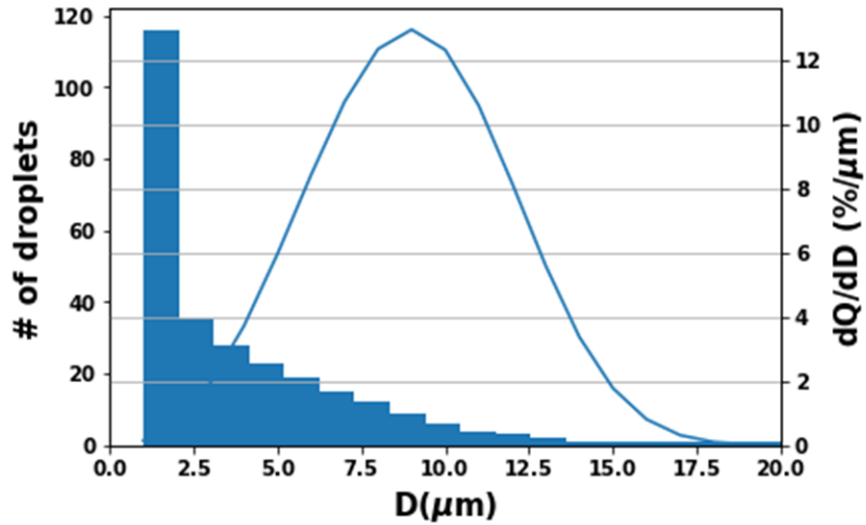


Figure 3.6-5. Example of droplet distribution based on a Rosin-Rammler distribution,  $X=10$ ,  $q=3.8$ . A total mass of 1 mg is used to obtain the number of droplets in each diameter.

### 3.6.2.3 Vaporizer

The purpose of the vaporizer is to heat up and vaporize the droplet. The temperature of the vaporizer (which is not the same as the droplet temperature) is set to be the temperature of the ignition kernel. The vaporizer function is called on each of the droplets. During a time step  $\Delta t$ , the droplet's temperature will first be checked. If the droplet's temperature is lower than the current wet-bulb temperature, the droplet will be heated towards its wet-bulb temperature. The wetbulb temperature is the steady-state temperature reached by the droplet at fast vaporization. The droplet will not reach the boiling temperature due to vaporization cooling. Due to small droplet size and hence small Biot number, the heat transfer rate inside the droplets are assumed infinite. In other words, the droplets will have uniform temperature, and the surface temperature is same as the internal droplet temperature. While the droplet is heating, vaporization will also occur as there exists a mass gradient in fuel species. The vaporization rate can be calculated by finding the



Spalding number based on the surface mass fraction, and the surface mass fraction can be calculated from the Clausius-Clayperon relation and Raoult's law [1]. The governing energy equation is

$$m \times c \times \frac{dT}{dt} = \dot{Q} - \dot{m} \times \mathcal{L}_v \quad (18)$$

where  $m$  is mass of the droplet,  $c$  is the heat capacity of the liquid fuel,  $T$  is the temperature of the droplet,  $t$  is time,  $\dot{Q}$  is the convective heat transfer,  $\dot{m}$  is the mass evaporation rate, and  $\mathcal{L}_v$  is the latent heat of vaporization. The convective heat transfer,  $\dot{Q}$ , is calculated as

$$\dot{Q} = h \times \pi \times d^2 \times (\tilde{T} - T) \quad (19)$$

where  $h$  is the convective heat transfer coefficient and  $\tilde{T}$  is the ambient temperature. The convective heat transfer coefficient is defined as

$$h = \frac{Nu \times k}{L} \quad (20)$$

where  $Nu$  is the Nusselt number,  $k$  is the thermal conductivity of the liquid, and  $L$  is a characteristic length that is set to the ratio of volume to surface area for a spherical droplet. The Nusselt number,  $Nu$ , is based on a model developed by Abramzon and Sirignano [39]. The expression for the Nusselt number is given in Appendix D. The mass vaporization rate is expressed as

$$\dot{m} = 2\pi\overline{\rho}_g D_{Fa} R_D Sh_O \ln(1 + B_M) \quad (21)$$

where  $\overline{\rho}_g$  is the average density of the gaseous mixture,  $D_{Fa}$  is the binary diffusion coefficient,  $R_d$  is the radius of the droplet,  $Sh_O$  is the Sherwood number, and  $B_M$  is the mass-based Spalding number, defined as

$$B_M = \frac{Y_s - Y_\infty}{1 - Y_s} \quad (22)$$

where  $Y_s$  is the fuel mass fraction on the droplet surface, and  $Y_\infty$  is the fuel mass fraction far from the droplet.  $Y_\infty$  is assumed to be 0. The binary diffusion coefficient of n-dodecane and air is used, because average molecular fuels of these jet fuels is closest to that of the n-dodecane. The calculation of the binary diffusion coefficient can be found in [40]. The droplet Reynolds number  $R_D$  can be calculated as

$$Re_D = \frac{U_{rel} D}{\nu} \quad (23)$$

where the  $U_{rel}$  is the velocity of the droplet relative to the surrounding fluid,  $D$  is the diameter of the droplet, and  $\nu$  is the dynamic viscosity of the surround fluid. For a single 10  $\mu\text{m}$  radius, n-dodecane droplet in 880 K air with 10 m/s relative velocity and 300 K initial temperature, the temperature and radius profile as a function of time is shown in Figure 3.6-6. The corresponding vaporization rate and the heat transferred to the droplet are shown in Figure 3.6-7. The results from [40] under the same conditions is presented in

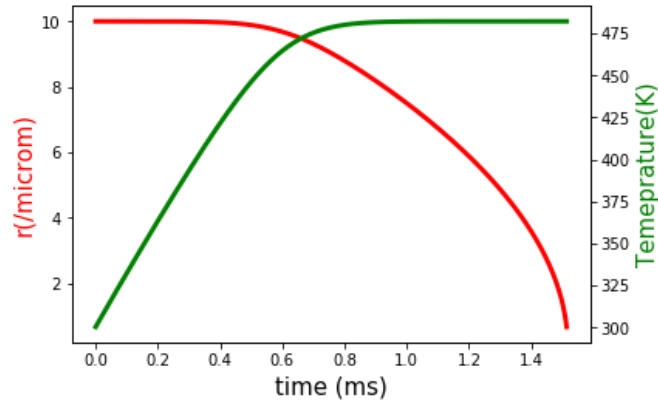


Figure 3.6-6. Radius (red) and Temperature (green) profile for a 10  $\mu\text{m}$ , n-dodecane droplet heating and vaporizing in 880 K ambient air with a relative velocity of 10 m/s.

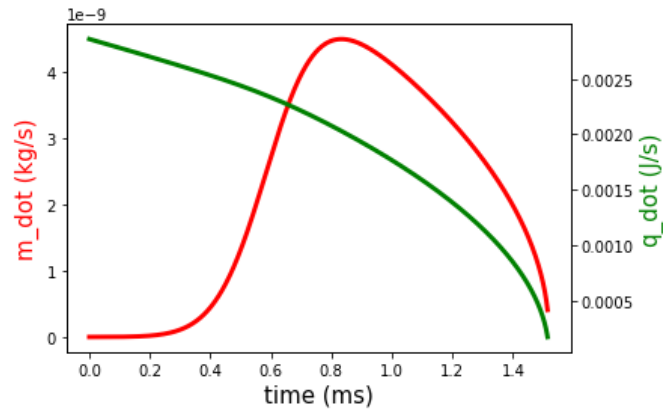


Figure 3.6-7. The vaporization rate  $\dot{m}$  (red) and the heat transferred to the droplet  $\dot{q}$  (green) profile for a 10  $\mu\text{m}$ , n-dodecane droplet heating and vaporizing in 880 K ambient air with a relative velocity of 10 m/s.

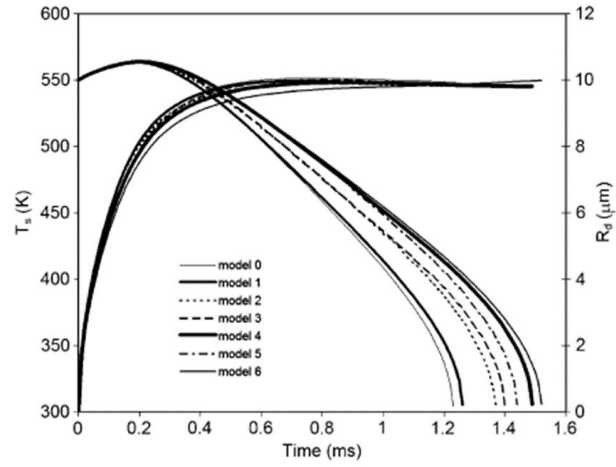


Figure 3.6-8. Results for a 10  $\mu\text{m}$  radius n-dodecane droplet in 880 K environment at 10 m/s relative velocity from [40]. Model 4 is from Abramzon and Sirignano[39].

## **CHAPTER 4:**

### **SPARK KERNEL STRUCTURE**

For the sunken fire igniter, the spark kernel ejects vertically from the igniter into a horizontal crossflow. This chapter reports on a set of high-speed imaging diagnostic experiments used to reveal the structure of the spark kernel and its evolution at early times as the kernel moves into the crossflow. Prevaporized fuel is used in the experiments as the liquid droplets (including their impact on the test section windows) would interfere with the imaging diagnostics. Like a pulsed jet, the spark kernel is expected to entrain surrounding fluids, as introduced in §2.1. Schlieren imaging is used to confirm the entrainment structure and obtain the rate of entrainment. Chemiluminescence and PLIF imaging are used to examine presence of fuel chemistry during early times in the forced ignition process.

#### **4.1 Ignition process revelation via high speed diagnostics**

##### *4.1.1 Spark kernel characterization*

For all the ignition studies presented here, the inflow velocity, and air and fuel temperatures were controlled and held nearly constant during experimental runs, so as to isolate fuel composition effects. Of course, another important influence on successful ignition is the strength of the spark kernel generated by the igniter. As the number of igniter pulses characterized during the high-speed imaging experiments was limited to a statistically insignificant set, it is important to determine whether the shot-to-shot behavior of the igniter could be a controlling influence in the experimental results. To this end, the

schlieren images were used to characterize the repeatability of the early spark kernel behavior.

During early times, before significant heat release, the behavior of the kernel should be controlled by the initial plasma discharge conditions that create the kernel. Specifically, the ejection velocity of the kernel from the cavity will be controlled by the pressure impulse created by the discharge, which in turn is a function of the energy deposited during the discharge. Thus, the vertical velocity of the kernel can be used as a good indicator of the spark kernel energy. The vertical velocity is calculated by using the translation of the top edge of the kernel in between frames.

Figure 4.1-1 provides time-histories of the kernel velocities for A2 runs, conditionally averaged over multiple igniter pulses, with successful events separated from failed cases. As expected, the kernels decelerate as they interact with the crossflow. More importantly, the velocity difference between the two cases is generally much less than 10%. Furthermore, the difference is less than 2% at the first measurement time after the kernel discharge. The one time where there is a measured difference above 10%, at  $\sim 0.1$  ms, is likely due to limitations in the image processing algorithm's ability to reliably identify the kernel edge as it emerges from the mixing layer. Figure 4.1-2 provides similar results for successful ignition events for the three different fuels. Again, the initial velocities after the discharge are nearly the same for all three fuel cases. The velocities at later times are also similar, with no systematic differences observed.

Thus, it is reasonable to conclude that the deposited spark energy is not varying enough between successful and unsuccessful cases to be the controlling factor for ignition. In

addition, the deposited spark energies are similar for all three fuel tests - so any fuel differences observed are unlikely to be a result of igniter non-repeatability. Therefore, any shot-to-shot variations in the ignition events are probably attributable to changes in mixing between the kernel and the crossflow.

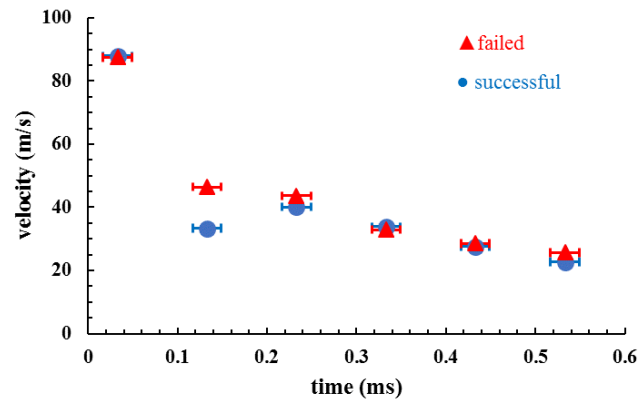


Figure 4.1-1. Vertical velocity histories of the spark kernel, determined from the high-speed schlieren images, averaged over three successful and unsuccessful ignition events. For the A2 fuel. The horizontal bars show the uncertainty in time after the spark discharge due to triggering of the camera.

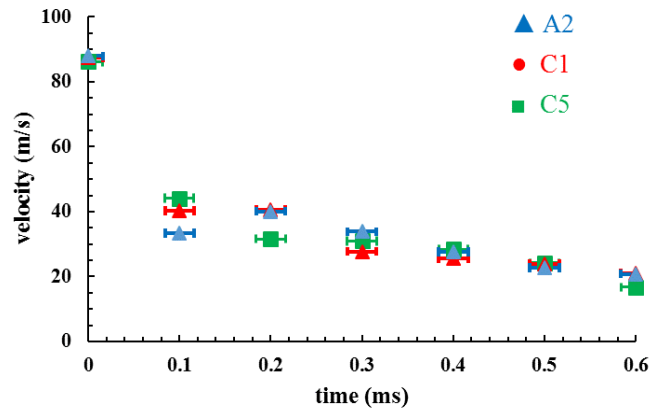


Figure 4.1-2. Vertical velocity history of the spark kernels for each of the fuels tested, each averaged over three successful events.

The schlieren imaging results can also be used to estimate the volumetric growth rate of the kernel by assuming symmetry about an axis passing through the centroid of the 2-dimensional schlieren kernel. The volumetric growth based on 40 schlieren movies is given in Figure 4.1-3. Assuming an air density of the spark at 2000 K and 1 atm, the mass entrainment rate is 60 mg/s.

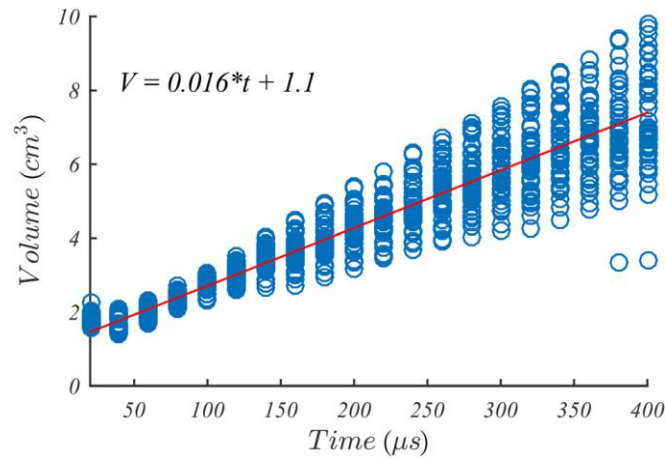


Figure 4.1-3. Volumetric growth of the spark kernel following discharge, obtained from high-speed schlieren data.

#### 4.1.2 Ignition characterization – fuel A2

One way to characterize the ignition behavior of a spark kernel is to compare the evolution of a successful kernel with that of a kernel that fails to produce a sustained flame. As a growing flame will have a corresponding increase in heat release, and thus chemiluminescence, we would expect the spatially integrated signal captured by the emission camera to increase in time for successful ignition. To examine this, the signal from each emission image was background corrected and spatially integrated over the field



of view, then normalized by the number of pixels in the integration region. Figure 4.1-4 shows the resulting values as a function of time for two spark pulses from an A2 experimental run: a successful ignition event and a failure.

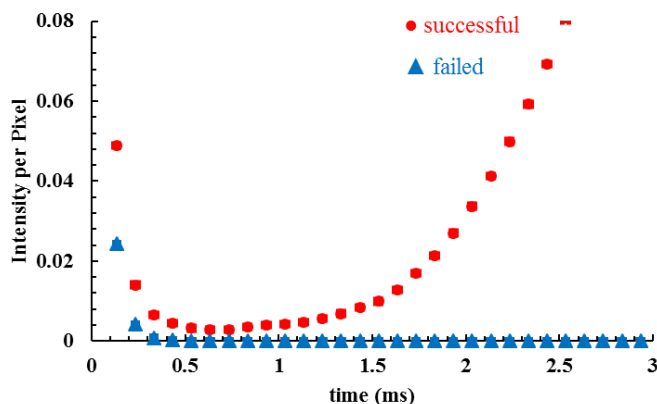


Figure 4.1-4. Intensity per pixel versus time for a successful ignition event and an unsuccessful event for fuel A2.

At early times (below 0.5 ms), both events show a decreasing signal. At least in part, this is due to broadband emission from the decaying spark plasma that passes through the 320 nm bandpass filter on the camera. Thus the captured emission signal at early times can be a combination of plasma emission and chemiluminescence. For the unsuccessful event, the emission signal reaches the camera background level between 0.3-0.4 ms. For the successful event, the signal decreases until ~0.6 ms, at which point it rises continuously. Moreover, it never drops as low as the unsuccessful event. Thus, we can conclude that the emission signal after 0.5-0.6 ms is solely due to flame emission (primarily OH\* based on the optical filter employed) and that “ignition” has occurred by this time (if not much earlier). Furthermore, the time required to reach a minimum intensity can be used to

characterize successful ignition. This time can be defined (arbitrarily) as the ignition delay time.

What is unclear from this spatially integrated analysis is what happens before this time, as one might expect chemical reactions could occur as soon as the hot kernel reaches the fuel-air mixture in the region above the splitter plate. To examine the early time behavior of the kernel, we now turn to the simultaneous information from the three high speed imaging systems: emission, PLIF and schlieren. Example images from three successful ignition events using the A2 fuel are shown in Figure 4.1-5, Figure 4.1-6, and Figure 4.1-7. Similar images for a failed event from the same experimental run are shown in Figure 4.1-9. Recall as described in Chapter 3, a process using a registration image was used to match the different cameras. As noted there, the matching was only partially successful, as can be seen by the vertical mismatch between the top of the emission region and the top of the schlieren region in the first image.

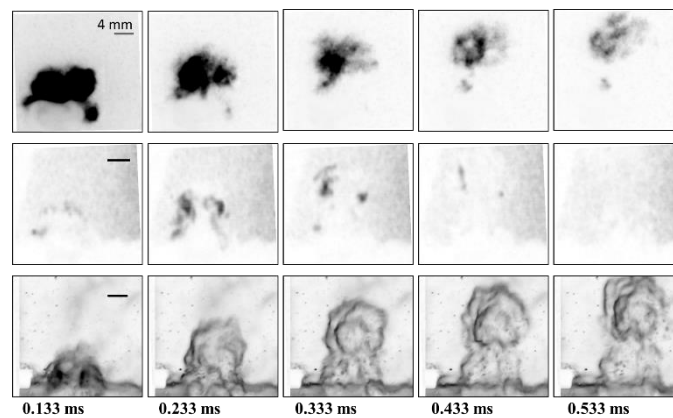


Figure 4.1-5. Sequence of simultaneously acquired emission (top), PLIF (middle) and schlieren (bottom) images for early times from a successful ignition event with the A2 fuel; the event is the same used in Figure 4.1-4. The crossflow direction is left to right in the images.

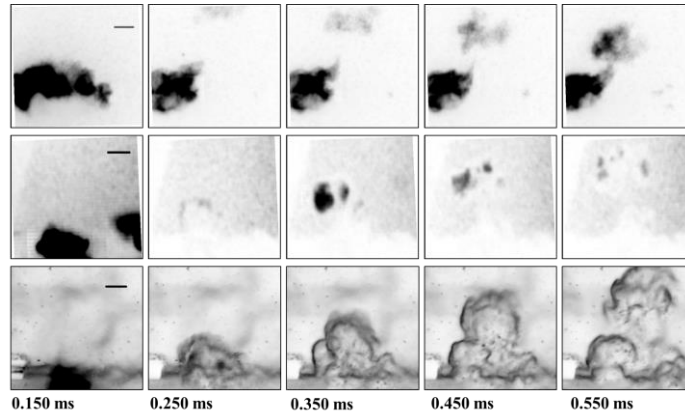


Figure 4.1-6. Successful ignition with A2, case 2.

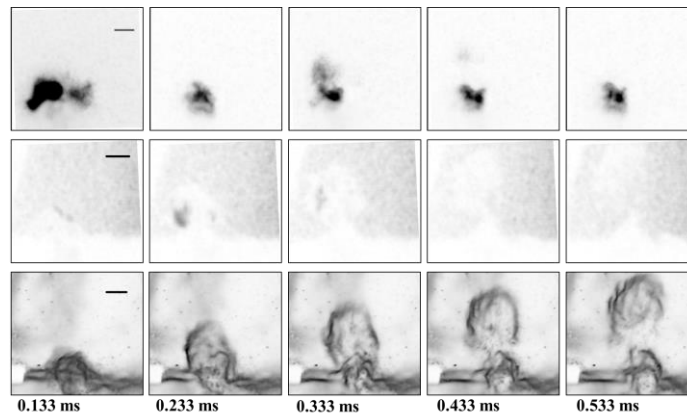


Figure 4.1-7. Successful ignition with A2, case 3.

As expected from the results of Figure 4.1-4, the overall UV emission captured by the chemiluminescence camera decays during these early times after the kernel is created. In addition to the peak intensities dropping, the size of the emitting region of the kernel also shrinks. On the other hand, the schlieren images show an increasing kernel size, with the kernel resembling a pulsed jet. Since the schlieren demarks large density gradients (i.e., between the cold crossflow and hot kernel) while the plasma emission from the kernel should be a strong function of its temperature, the logical interpretation of these results is the kernel is mixing with the crossflow. Thus the overall size of the hot gas region is

increasing, but the kernel's (average) temperatures is decreasing. Furthermore, the emission comes primarily from the upper portion of the kernel; the long trailing tails from the kernel seen in the schlieren images likely represent only "warm" gas.

The mixing of the hot kernel with the fuel air mixture has already occurred before the first image shown (0.133 ms), as evidenced in the schlieren image, where the top of the kernel is located above the splitter plate (seen as the rectangular dark shadow in the lower left edge of the image). Based on the velocity measurements presented above, the top edge of the kernel should reach the mixing layer within 60  $\mu$ s after the spark discharge.

The PLIF images in Figure 4.1-5 (middle row) display two notable features. First, the fluorescence is nearly uniform in distribution within the region illuminated by the sheet. This results from components of the A2 fuel that fluoresce. The relative uniformity in the fluorescence in the upper regions indicates the evenness of the fuel seeding in the upper flow, while the lack of signal in the lower portion of the images verifies the absence of fuel in the flow beneath the splitter plate.

The second notable feature is the behavior of the PLIF signal in the region of the kernel (as demarked by the schlieren signal). Much of the kernel does not produce a PLIF signal, presumably because there is much less fuel within the kernel compared to the crossflow. There is, however, a region of quite strong signal within a narrow portion of the kernel. This is most evident in the PLIF image at 0.233 ms, coming from a highly convoluted structure within the kernel region marked by the schlieren, but nearer the kernel's edges. Moreover, the region containing PLIF signal overlaps a portion of the emission region. This increased fluorescence occurs in all the PLIF images of Figure 4.1-5, but it peaks in

the 0.233 ms image, with the region of bright fluorescence rapidly decreasing with time. Furthermore, this signal comes only from the region of the kernel that has passed into the upper (fuel-air containing) region. Thus, we can conclude that the source of the signal is associated with the high temperature kernel air interacting with entrained fuel (and air). By the 0.533 ms image, the kernel's PLIF signal is limited to a few small regions.

The specific species that give rise to this early time PLIF signal is unclear. While the laser and camera bandpass filter were set to excite and detect OH fluorescence, a number of hydrocarbons are broadband absorbers in the UV and can produce fluorescence (as evidenced by the signal coming from the A2 fuel components). For example, possible fuel pyrolysis includes benzene and toluene, both of which exhibit UV excited fluorescence that might be detected by the 320 nm bandpass filter employed here. So, the kernel's PLIF signal may be produced by species associated with either fuel pyrolysis or oxidation (and heat release).

At later times, ~0.6-2.1 ms (Figure 4.1-8), we see that the region of PLIF signal begins to grow, eventually becoming a self-sustained flame. At these times, the signal is likely due primarily to OH PLIF. It is also interesting to note that by 1.1 ms, it is difficult to identify a region without fuel in the upper portion of the flow. Presumably, the mixing of the fuel-air mixture with the kernel has preceded to such an extent that there is little high temperature, unmixed "pure" kernel fluid left.

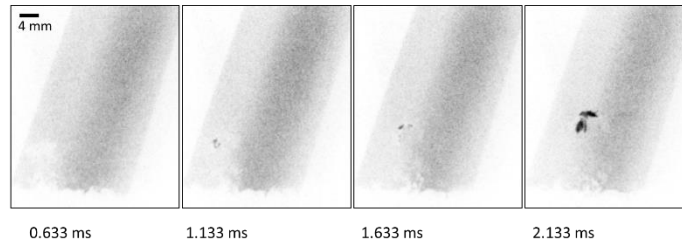


Figure 4.1-8. Sequence of PLIF images for later times for the successful A2 ignition event depicted in Figure 4.1-5.

To help interpret the early time results from the successful ignition event, we again compare them to a case of failed ignition (Figure 4.1-9). As before, both emission and PLIF signals occur after the spark discharge. In contrast to the successful ignition event, however, the signals decrease more quickly, essentially disappearing by  $\sim 0.5$  ms. If the PLIF signal from the kernel is associated with chemical reactions involving fuel, as suggested above, the similar temporal behavior for the PLIF and emission signals also suggests that at least part of the emission is due to chemical reactions, i.e., chemiluminescence, especially after the first 0.1-0.2 ms.

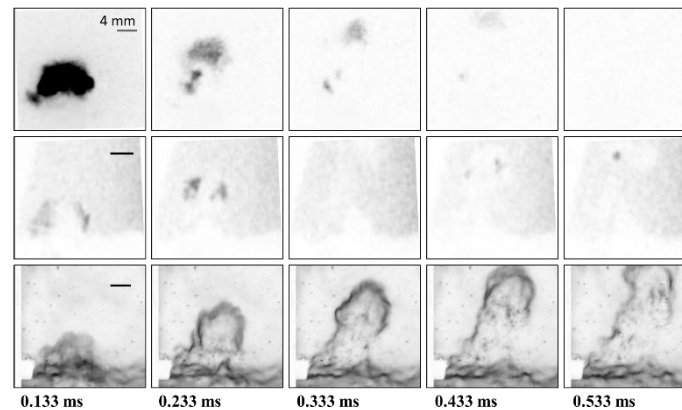


Figure 4.1-9. Sequence of simultaneously acquired emission (top), PLIF (middle) and schlieren (bottom) images for early times from a failed ignition event with the A2 fuel; the event is the same used in Figure 4.1-4.

It is reasonable to conclude that at least partial oxidation of the fuel, with some heat release, is occurring within the first few hundred microseconds for both failed and successful ignition events. In addition, the rate and extent of these reactions is greatest in the first 0.1-0.2 ms after the igniter discharge (or shortly after the kernel begins entraining the fuel-air mixture). The decrease in reactions after this time may be due to the decrease in kernel temperature resulting from the mixing of the hot kernel with cold reactants. Of course, this would also suggest that any heat release from fuel oxidation is more than offset by cooling due to entrainment and mixing. Given the small spatial extent of the PLIF and chemiluminescence signals at 0.533 ms, whether ignition is successful depends on the relative amount of heat release and dilution in a quite small region of the kernel. If the heat release is inadequate or the mixing too rapid, the temperature will rapidly decrease, extinguishing the reactions.

#### *4.1.3 Ignition characterization – fuel comparison*

Similar high-speed imaging results were also acquired for two other fuels, C5 (Figure 4.1-10, Figure 4.1-11, and Figure 4.1-12) and C1 (Figure 4.1-13 and Figure 4.1-14). The most noticeable difference between these results and the A2 images is the lack of PLIF signal from the unreacted fuel. Neither of the C fuels contain cyclo-paraffins, while they are a significant component of A2 (see Appendix A). Thus, they are a possible source of the fuel PLIF seen in A2. On the other hand, both the C5 and C1 fuel PLIF images do exhibit the same kernel PLIF signals recorded for the A2 fuel. Since the parent fuel produces no fluorescence, this provides further support that the source of the fluorescence is a species produced by chemical reactions between the high temperature kernel and the entrained fuel-air mixture.

As with the A2 results, the emission and PLIF signals decay after the first few hundred microseconds for both fuels. There is a notable difference between the C5 and C1 data; both the emission and PLIF are more pronounced and cover a greater portion of the kernel for the C5 fuel compared to C1.

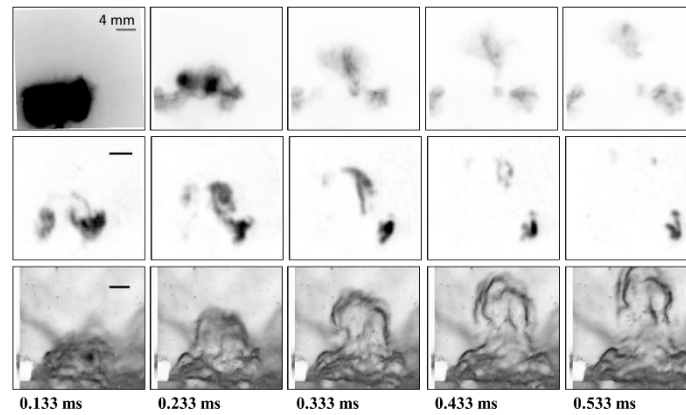


Figure 4.1-10. Sequence of simultaneously acquired emission (top), PLIF (middle) and schlieren (bottom) images for early times from a successful ignition event with the C5 fuel.

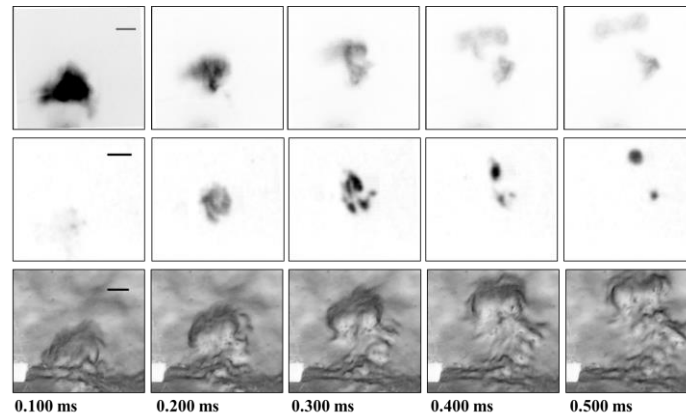


Figure 4.1-11. Successful ignition with C5, case 2.



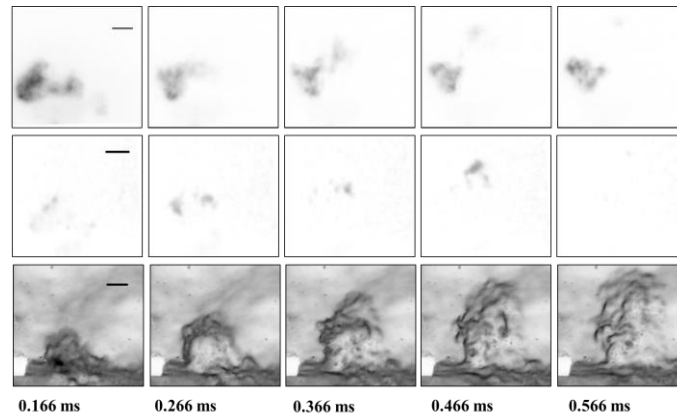


Figure 4.1-12. Successful ignition with C5, case 3.

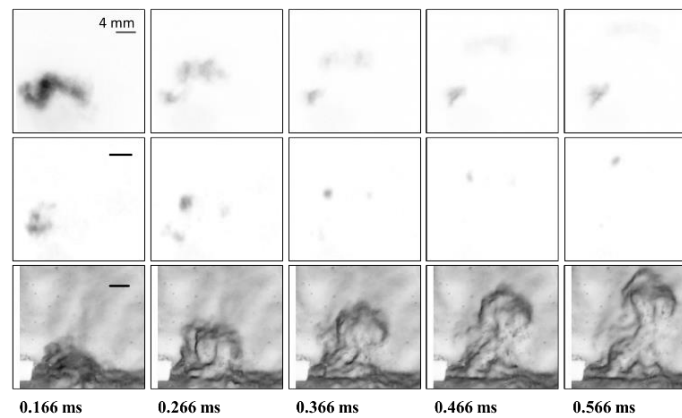


Figure 4.1-13. Sequence of simultaneously acquired emission (top), PLIF (middle) and schlieren (bottom) images for early times from a successful ignition event with the C1 fuel.

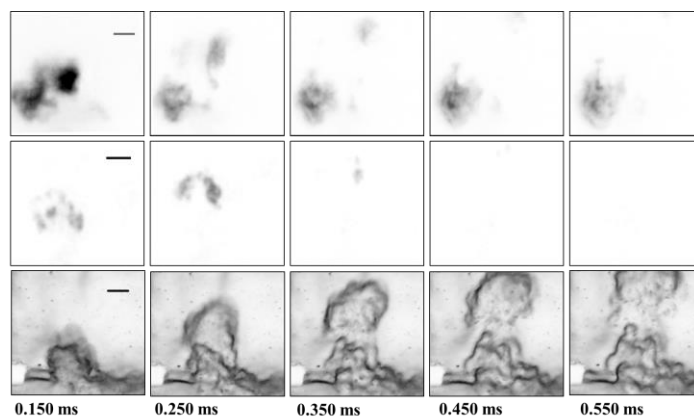


Figure 4.1-14. Successful ignition with C1, case 2.

The C5 data (Figure 4.1-10) also exhibit another feature not shown in the A2 and C1 images sequences, a bifurcated ignition kernel. This is most visible in the PLIF image sequence, where a structure appears to break from the main kernel and stays closer to the lower wall. Not only does this structure lack a vertical (upward) velocity, it also does not decay in size or intensity like the upward moving kernel. A corresponding structure of roughly the same size is evident in the chemiluminescence image. At later times, this second structure leads to a self-propagating flame that is independent of the flame produced by the upward moving kernel. The lack of decay observed in this structure suggests that it does not undergo the same amount of mixing with cold fluid compared to the main kernel. This behavior occurs in some sequences for all three fuels.

Finally, we can compare the ignition performance for the three fuels. The spatially integrated emission/chemiluminescence data for the A2, C1, and C5 fuels are shown in Figure 4.1-15, averaged over three successful ignition events for each fuel. As expected from the images shown previously, the emission initially decays for all the fuels before eventually rising as the self-sustained flame grows.

Ignition delay times based on the minimum values in these profiles are listed in Table 5. The ignition delays for C5 and A2 are the same (~0.5 ms), but about 0.3 ms faster than for C1. In addition to the much longer delay, the C1 fuel also has the slowest rate of increase in chemiluminescence/emission signal. This may correlate to the lack of aromatics in the C1 fuel.

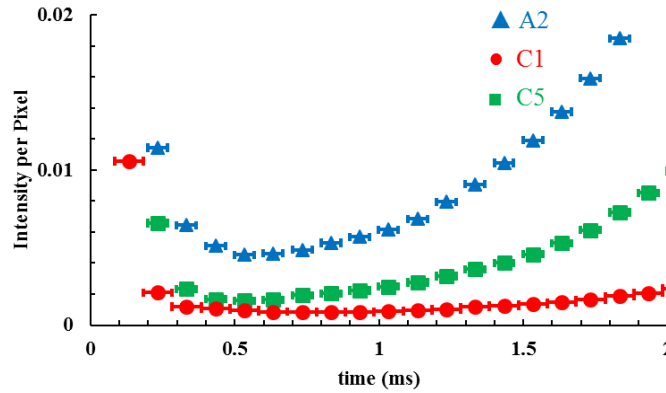


Figure 4.1-15. Spatially integrated and background corrected emission camera intensities for three fuels. Each data point represents the average over three successful ignition events.

Table 5. Ignition delay time based on minimum values obtained in Figure 4.1-15.

Fuel	A2	C1	C5
Turnaround	0.53	0.84	0.53
Time (ms)	$\pm 0.034$	$\pm 0.05$	$\pm 0.034$

## 4.2 Chapter summary

In this chapter, high speed (10 kHz) imaging is used to monitor the ignition kernel development in prevaporized fuel (A2, C1 and C5) and air mixtures. The ejection velocities

of the kernels, found from the schlieren imaging are essentially the same for successful and unsuccessful cases. The schlieren results also provide a measure of, the volumetric growth rate of the kernel.

The PLIF results show that chemical reactions occur within tens of microseconds after the kernel starts interacting with the fuel. This early strong fluorescence signal weakens over time for both the successful and the unsuccessful ignitions. After  $\sim 0.6$  ms in the kernel's existence, the fluorescence signal for the successful case becomes more intense at a few ("hot") spots, which then grow into a self-sustained flame. For the unsuccessful case, the fluorescence signal disappears. The simultaneous emission imaging results confirm these important time scales. The evolution of the spatially integrated chemiluminescence signals are used to define ignition delay times for each successful event. Different delay times are seen for the different fuels; A2 and C5 have similar delay times, whereas C1 takes longer to ignite.

## **CHAPTER 5:**

### **FORCED IGNITION OF PREVAPORIZED FUEL/AIR MIXTURE**

In the previous chapter, high speed diagnostics are used to observe the early physical and chemical evolution of a spark kernel and differences in this behavior for three prevaporized jet fuels. This chapter examines a more direct measure of differences in ignition due to fuel chemistry, specifically the ignition probabilities of hundreds of ignition events for each of eleven fuels. The properties that lead to a more favorable fuel chemistry are explored using both the experimental results and simulations using the two-stage, reduced order model for forced ignition presented in Chapter 3.

#### **5.1 Effect of equivalence ratio and fuel performance ranking**

The ignition probabilities with prevaporized conditions were measured for three category A fuels (A1, A2, A3), five category C fuels (C1, C2, C3, C4, and C5), and three surrogate fuels (S1, S2, and n-dodecane). The descriptions of these fuels can be found in §3.2.

For the eight category A and C fuels, ignition probabilities were acquired for equivalence ratios (of the main flow) ranging from 0.6 to 0.8. The dependence of the (binned) ignition probabilities on equivalence ratio is presented in Figure 5.1-1 for each fuel. The binning is achieved by averaging the probabilities within a bin of  $\Delta\phi=0.04$ . Each data point represents the average probability for hundreds of spark events. For all the fuels, when the equivalence ratio decreases, the ignition probability also decreases. As the equivalence ratio drops, the flammability limits of these hydrocarbon fuels are also

approached; so this trend is not surprising, though the reason for the decrease in probability is not necessarily a function of the relative flammability of the fuel. Moreover as the equivalence ratio increases, the probabilities increase at different rates for each of the fuels.

A previous study [8] has shown that the absolute ignition probability depends on several factors including the height of the splitter plate and the temperature of the cross-flow fluid; both were fixed in the current study. Thus, the relative differences in the absolute ignition probability is a good indicator for comparing fuel performances in transitioning into a self-sustaining flame. As the ignition probabilities changes appear rather linear with different slopes and same starting position, the ranking of ignition probabilities at one equivalence can represent the overall performance. The equivalence ratio chosen for comparison is 0.675, because there are data taken at this equivalence ratio and the ignition probabilities are high enough for all the fuels that the relative uncertainties are reasonable.<sup>2</sup>

The results of ignition for prevaporized fuel/air mixture at an equivalence ratio of 0.675 is shown in Figure 5.1-2. The rankings are based on the relative ignition probabilities with respect to that of A-2, as defined in Chapter 3. Among the A fuels, A1 has the highest probability, followed by A3 and then A2. Among the C fuels, C5 has the highest ignition probability, and C1 has the lowest ignition probability. For the two surrogate fuels tested, S1 has a higher ignition probability than that of S2. The fuel ranking provides the relative fuel performances in forced ignition. However, it is more important to understand the

---

<sup>2</sup>It should be pointed out that low single-event ignition probabilities are not unreasonable for aeroengine combustors. For example if the ignition probability for each spark event is just 4%, then within 150 shots the probability of at least one ignition spark transitioning into a flame is 99.8%, which is rather high.

underlying factors that control the differences in forced ignition. In prevaporized ignition, only differences in the fuel's chemical properties should significantly impact ignition performance. To understand the potential effects that fuel composition has on forced ignition, we can see how the ignition performances correlate to specific fuel (chemical) properties.

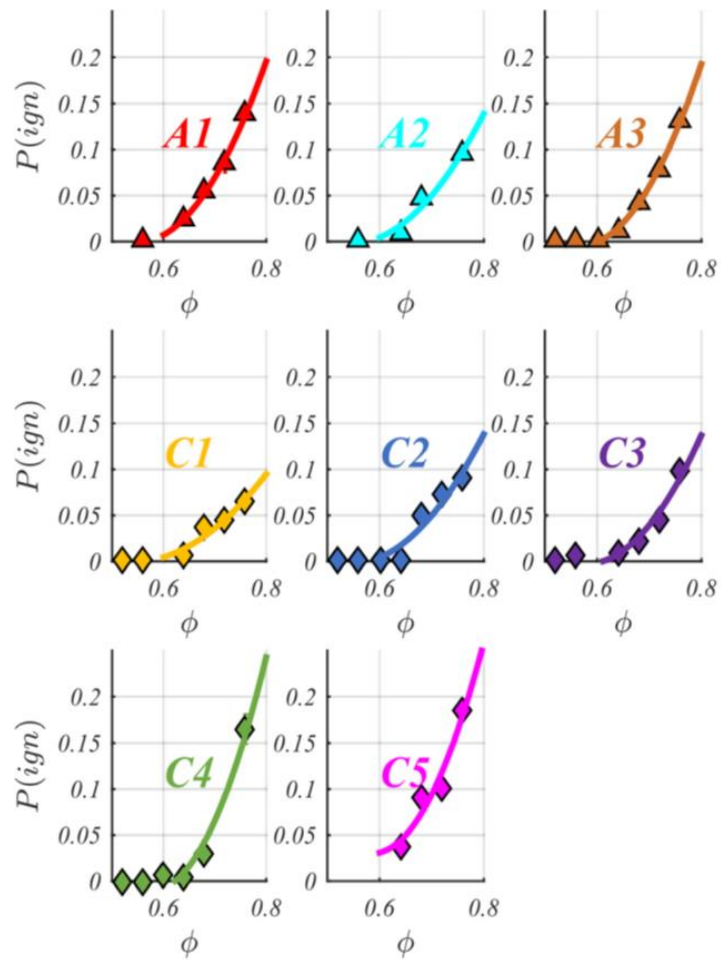


Figure 5.1-1. Binned Ignition probability data. Each data point contains ~300 ignition events.

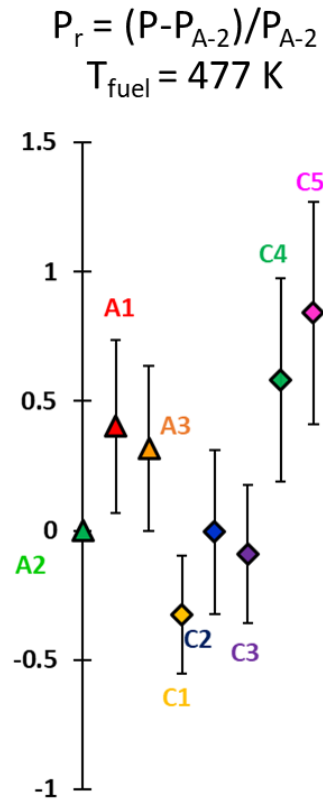


Figure 5.1-2. Ranking of relative ignition probability with respect to that of A2 for prevaporized fuel/air mixtures. The equivalence ratio of the main flow is at 0.675.

One such property often used for rating jet fuels is the derived cetane number (DCN); it is based on a fuel's ability to autoignite at specific conditions. DCN is calculated based on the cetane number [41], which is determined experimentally with an ignition quality tester. The DCN is considered a good indicator of the fuel's chemical reactivity, with DCN of 100 representing the most chemically reactive and 0 the least. The correlation of the relative ignition probabilities to the DCN is illustrated in Figure 5.1-3; no clear overall trend is observed. The fuel C1, which has the lowest DCN, also has a low ignition probability. Excluding C1, however, the data suggest the ignition probability increases with a decrease in DCN - a trend that is counter-intuitive based on the definition of DCN.



Furthermore, for fuels with DCN very close to that of A2, there are significant differences in ignition probability. For S2, which contains ~50% of n-hexadecane (cetane), the ignition probability comes out to be the lowest.

According to the ASTM standard [41], DCN is determined with an air temperature near 800 K. In forced ignition, the temperature of the hot air within the spark kernel can reach a few thousand degrees. Fuel chemistry can be significantly different at very high temperature as compared to the DCN test temperature. In conclusion, variations in the DCN, which is thought to be an indicator of fuels' chemical reactivity, do not appear to have a meaningful correlation to the variation in probability of forced ignition in the mixing layer flow facility.

Though DCN does not show good correlation, other measures of chemical composition may. The major groups of chemical compounds in these fuels include iso-paraffins, n-paraffins, aromatics, and cyclo-paraffins. The correlations to the fractional composition of these compounds are shown in Figure 5.1-4 through Figure 5.1-7. These simple (single) parameter correlations do not reveal any clear dependence on the amount of any of the major chemical groups in the fuel's composition. The next section explores the use of the reduced-order PSR model coupled to the HyChem mechanisms to provide more insight into the chemical reaction pathways that control forced ignition.

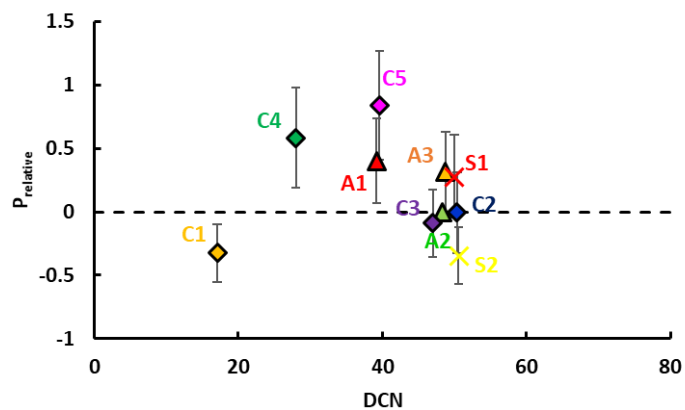


Figure 5.1-3. Relative ignition probability (vaporized fuel) compared to the fuel's DCN.

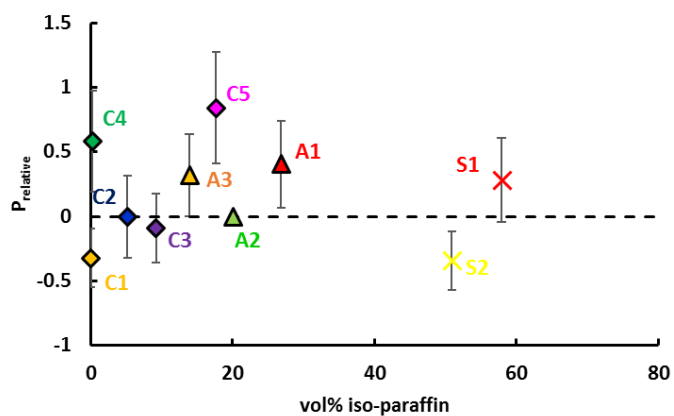


Figure 5.1-4. Relative ignition probability (vaporized fuel) compared to volumetric percentage of iso-paraffins.

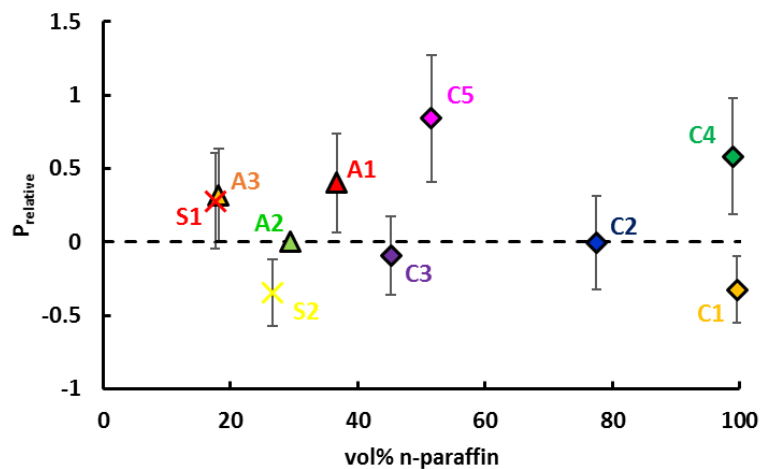


Figure 5.1-5. Relative ignition probability (vaporized fuel) compared to volumetric percentage of n-paraffins.

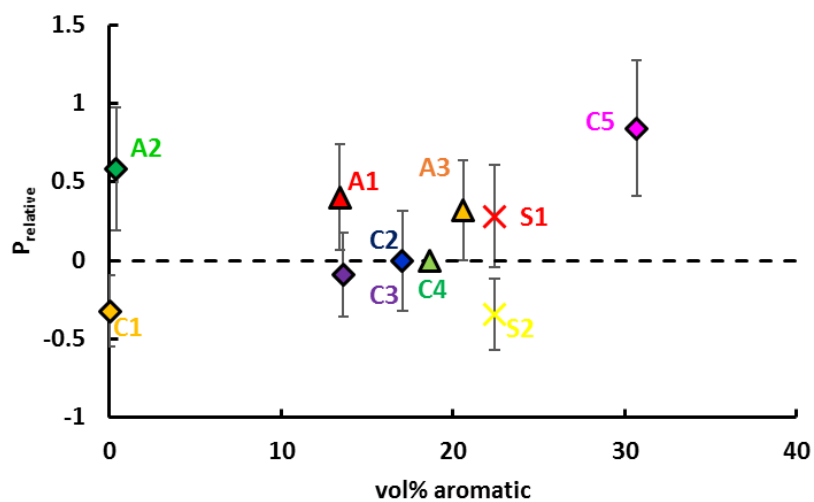


Figure 5.1-6. Relative ignition probability (vaporized fuel) compared to volumetric percentage of aromatics.

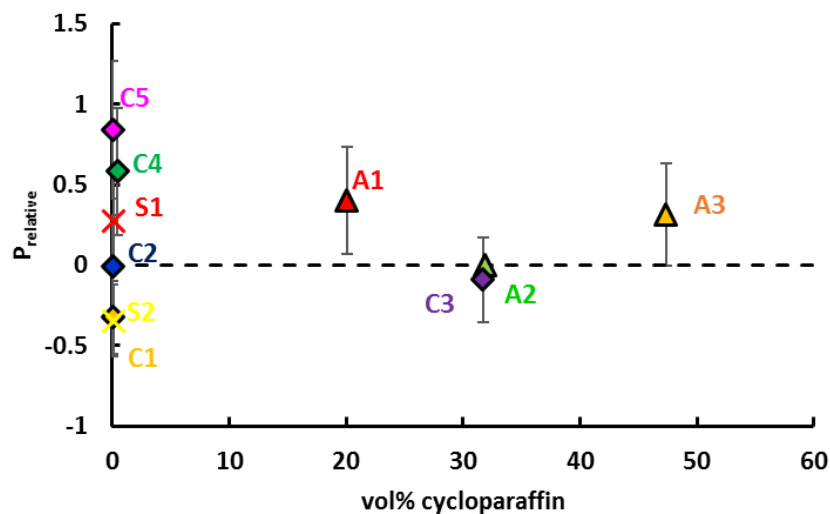


Figure 5.1-7. Relative ignition probability (vaporized fuel) compared to volumetric percentage of cycloparaffins.

## 5.2 Reduced order simulation results

### 5.2.1 Successful vs. unsuccessful ignition

The HyChem mechanisms [36] are available for the A1, A2, C1, C3, and C5 fuels. As described in §3.6.1, a two stage PSR model is used to simulate the kernel ignition process. The fuel mechanisms are calibrated based on species concentration data from autoignition experiments conducted in a shock tube and flow reactor measurements. The post-shock (autoignition) temperatures are varied between 800 K and 1300 K.

The reduced-order, entraining PSR model cannot predict ignition probabilities for a fixed (certain) set of flow conditions; fuel performance in the PSR can, however, be characterized by finding the lean ignition limit (LIL). This is also consistent with empirical approach used in [9] to characterize ignition performance of different fuel blends. To

simulate ignition at the test conditions in the current experiments, the transit time of the first stage is set at 80  $\mu\text{s}$ , the mass entrainment rate of the kernel is set at 60  $\mu\text{g/s}$ , and the ambient fluid temperature is 477 K. In the reduced order simulations, a successful ignition is defined when the temperature of the kernel can maintain a high value and does not approach the ambient temperature after  $\sim 500 \mu\text{s}$ ; this is what would occur in the absence of significant heat release due to continuous entrainment of ambient fluid. Example results of the kernel's temperature evolution for successful ignition and failed ignition cases are shown in Figure 5.2-1.

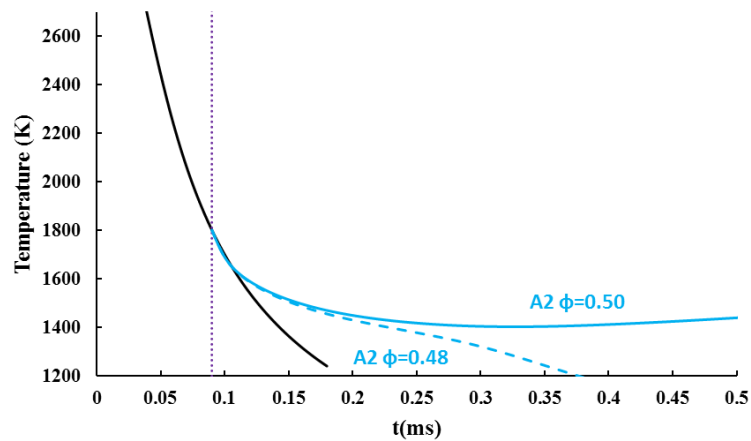


Figure 5.2-1. A successful ignition at  $\phi=0.50$  (blue solid line) and an unsuccessful ignition at  $\phi=0.48$  (blue dashed line). The solid black line represents the kernel temperature if no fuel is entrained. The second stage fuel entrainment starts at 0.09 ms. A spark is formed at  $t=0$ .

For fuel A2, the lean ignition limit occurs between  $\phi=0.48$  and 0.50. The solid black line indicates the kernel temperature if the kernel continues to entrain pure air with no fuel. If no fuel is present, the kernel temperature will decrease rapidly and reach  $\sim 1200 \text{ K}$  by 0.17 ms after the simulated spark event because the kernel must heat the entrained fluid.

The dilution cooling effect comes from the term  $\sum_{in} \dot{m}_{in}(h_{in} - \sum_k h_k Y_{k,in})$  in Equation 12.

At  $\phi=0.48$ , although the kernel temperature continues to drop, the rate of decrease is slower than when the kernel is entraining only air. This slower rate of decrease in temperature indicates that the fuel is causing heat release that helps sustain the kernel temperature, as given by the term  $\sum_{in} h_k \dot{m}_{k,gen}$  in Equation 12. The slope of the two cases entraining fuel and the case not entraining fuel deviate at around  $t=0.11$  ms. This suggests that there is no more than a  $30 \mu s$  chemical delay after the start of the second stage (when the kernel begins entraining a fuel/air mixture). To see more clearly the effect of dilution cooling and chemical heat release on the kernel's temperature, we can extract these two terms from the energy equation. The calculation of the heat release rate and the dilution cooling rate can be seen in Appendix B. The results for the chemical heat release rate and the dilution cooling are shown in Figure 5.2-2.

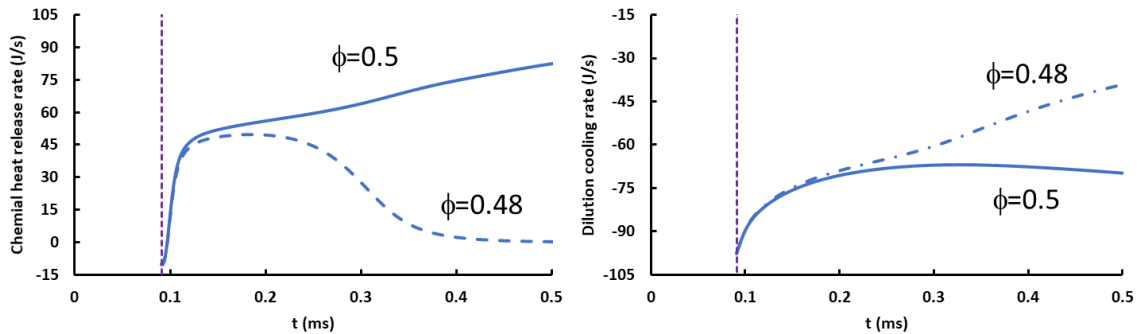


Figure 5.2-2. Chemical heat release rate and dilution cooling rate for the successful (solid blue) and the unsuccessful (dashed blue) as in Figure 5.1-1. The vertical dotted lines indicate the time when a flammable mixture starts being entrained.

In the two plots in Figure 5.2-2, the solid line indicates the successful case in Figure 5.2-1 when  $\phi=0.50$ , and the dashed line indicates the failed case when  $\phi=0.48$ . From the plot for the chemical heat release rate, we can see that in the first 8  $\mu\text{s}$  after the flammable mixture entrainment begins, the chemical heat release rate is negative. During this period, chemical reactions are taking energy from the kernel to dissociate the original fuel into intermediate products. Later, the heat release rate becomes positive for both  $\phi=0.50$  and  $\phi=0.48$ . As can be seen in the temperature profile (Figure 5.2-1) for  $\phi=0.48$ , the temperature for this unsuccessful ignition will drop slower than the temperature for the case where only air is entrained. This heat release rate shows that even through ignition is unsuccessful, chemical reactions are occurring that release heat. For the successful case, the heat release continues to rise and eventually reach a steady-state value. For the unsuccessful case, on the other hand, the heat release rate eventually decreases to zero, as the temperature of the kernel drops so much that the chemical reaction rates become too slow. In this example, this occurs at  $\sim 0.36$  ms corresponding to a kernel temperature of  $\sim 1400$  K.

The chemical heat release is the mechanism that sustains the chemical reactions, so that further heat releasing chemical reactions, i.e., combustion, is possible. If the temperature of the kernel is only controlled by the chemical heat release, the temperature will rise to the adiabatic reaction temperature (for the kernel's fuel-air ratio), and ignition will never fail no matter how lean is the fuel/air mixture. Therefore, a cooling mechanism is necessary. The fast entrainment structure of the kernel as observed in §4.1 indicates that cooling due to mixing with the cooler entrained fluid is the primary cooling mechanism.<sup>3</sup>

---

<sup>3</sup>Furthermore, diffusion between the kernel and ambient fluid was shown to be negligible in §3.6.1.

This mixing cooling will be referred to as dilution, as the hot kernel fluid is diluted by the colder ambient fluid.

The right graph in Figure 5.2-2 shows the dilution cooling rate. The negative values of the dilution cooling indicate a tendency to decrease the kernel temperature. Dilution effect are stronger when the temperature differences between the kernel and the entrained fluid are larger, since the kernel will need to heat the entrained fluid to a higher temperature. At early times after entrainment of the fuel/air mixture starts, the dilution cooling rates are similar for  $\phi=0.50$  and  $\phi=0.48$ . The slight change in composition does not affect the dilution rate. Later the dilution rate magnitude for the unsuccessful case ( $\phi=0.48$ ) decreases and approaches zero as the kernel temperature approaches that of the ambient fluid temperature. The dilution rate magnitude for the  $\phi=0.50$  first decrease and then increases to a steady state, as the chemical heat release can increase the temperature of the kernel so that the kernel will need to heat the entrained fluid to a higher temperature.

In summary, the temperature of the kernel is controlled by the chemical reactions and the dilution cooling. The chemical reaction will in general increase the kernel temperature, except that at early time, endothermic (heat absorbing) reactions associated with parent fuel decomposition require energy from the kernel. Dilution cooling always decrease the temperature of the kernel. A successful ignition is defined as that the chemical heat release can sustain the kernel at a high temperature. If the chemical heat release drops to zero, then the kernel ignition failed. The success of an ignition kernel is determined by two competing mechanisms: heat releasing chemical reactions and dilution cooling. If the kernel temperature drops below a certain threshold temperature ( $\sim 1400$  K), chemical reactions are



not sufficiently fast to overcome the dilution cooling. The main impact of equivalence ratio is to determine how much energy release can occur per unit mass of entrained fluid.

### 5.2.2 Fuel comparison: A2 vs. C1

As shown in Figure 5.1-2, the C1 fuel has the lowest ignition probability and therefore the worst ignition performance. As a reminder, ignition performance can also be characterized by the lean ignition limit. To check if the reduced order model can predict relative ignition performance, the lean ignition limit for A2 and C1 were simulated for conditions estimated to be similar to the test conditions. The results for the lean ignition limits of A2 and C1 are presented in Figure 5.2-3.

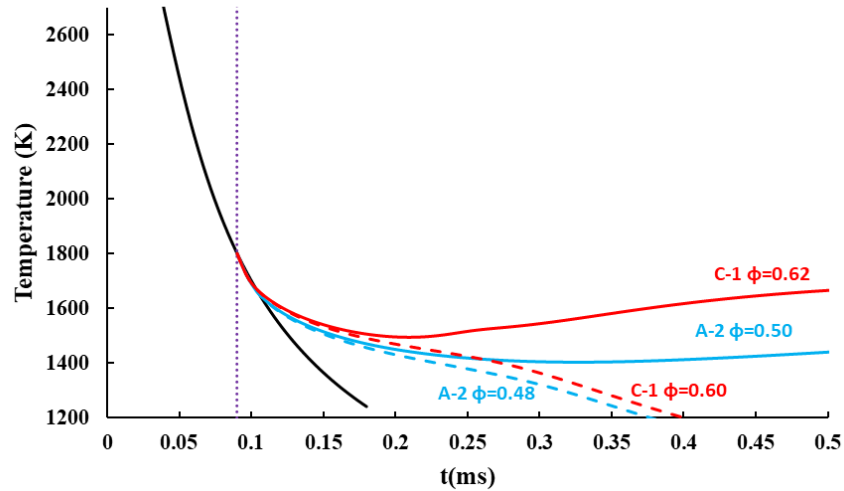


Figure 5.2-3. The bifurcation for the lean ignition limits for A2 and C1. The red curves show result for C1, and the blue curve show results for A2. The solid lines are for successful cases, and the dashed lines are for unsuccessful cases. The dark solid line shows the kernel temperature without fuel entrainment. The vertical dotted line indicates when fuel entrainment starts (at 0.09 ms).

From Figure 5.2-3, we can see that the lean ignition limit occurs for A2 in between an equivalence ratio of 0.48 and 0.50, whereas for C1 it occurs in between  $\phi=0.60$  and  $\phi=0.62$ .

A higher lean ignition limit means the fuel is harder to ignite, as more fuel is required to generate sufficient heat release. The heat release and dilution cooling rates for the four cases are shown in Figure 5.2-4. The left plot in Figure 5.2-4 shows the heat release after the kernel entrains fuel/air mixture. The four curves correspond to the four cases in Figure 5.2-3. As before, the chemical heat release rate is negative within the first 8  $\mu$ s after entraining the fuel/air mixture due to endothermic fuel decomposition. The A2 and C1 cases have approximately the same duration of negative heat release, thus the time required for the original fuel breakdown is approximately the same for both fuels according to the HyChem mechanisms. This will become clearer when we examine the species histories. Regardless of fuel, a richer flammable mixture will give more heat release, as evidenced by C1 at  $\phi=0.60$  and A2 at  $\phi=0.48$  and  $\phi=0.50$ . If the rates of parent fuel breakdown are fast, then the intermediate species will determine the rest of the heat release profile. At a time of  $\sim 0.22$  ms, the temperature for C1 at  $\phi=0.60$  starts to drop faster than for A2 at  $\phi=0.48$ . The heat release rate of C1 appears more sensitive to the change in temperature. The dilution cooling rate is a strong function of the kernel temperature. Higher kernel temperatures will give higher dilution cooling rates, and vice versa.

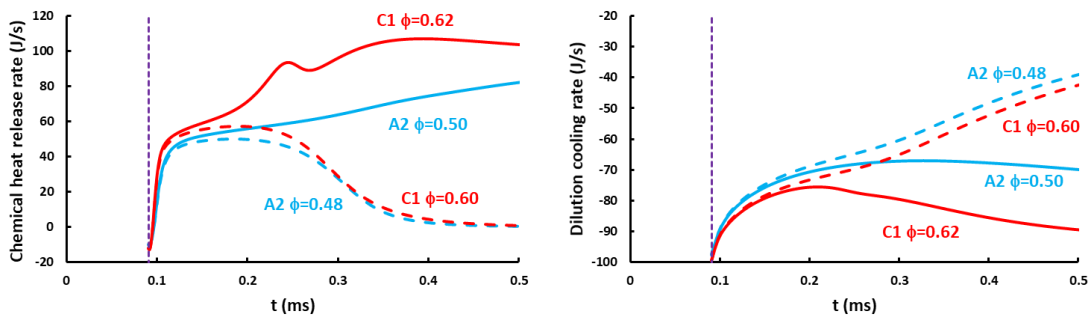


Figure 5.2-4. Chemical heat release rate and dilution cooling rate for the successful (solid blue) and the unsuccessful (dashed blue) as in Figure 5.2-3.

To discover why C1 is predicted to require more fuel to ignite than A2, we can look at cases where A2 succeeds and C1 fails at the same equivalence ratio. Based on the results in Figure 5.2-3, if  $\phi=0.60$  is chosen, A2 will ignite, but C1 will not. The temperature profiles of the ignition kernel for A2 and C1 at  $\phi=0.6$  is shown in Figure 5.2-5. As predicted, the case for A2 at  $\phi=0.6$  produces successful ignition. From the previous analysis, we know the kernel temperature is controlled by the heat release rate. Given that the heating values of A2 and C1 are similar and the heat and time required for the early endothermic fuel breakdown reactions are similar, we can hypothesize the reason for fast or slow exothermic reactions is that the concentration and reaction rates for the intermediate species are different.

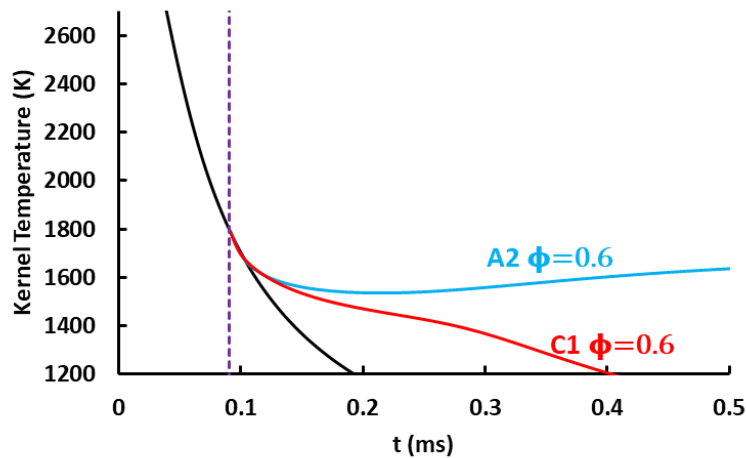


Figure 5.2-5. Ignition kernel simulation for A2 and C1 at  $\phi=0.6$ .

One of the assumptions for the HyChem mechanism [36] is that the exact chemical path for the decomposition of the original fuel is not important, rather the relative composition of the intermediate fuel products. In addition, the parent fuel decomposition rate is much faster than the rate at which the intermediate products react. Thus, the

intermediate product chemistry might be expected to control the ignition process when comparing different fuels. As outlined in §3.6.1, the primary intermediate products generated include H and CH<sub>3</sub> radicals, methane (CH<sub>4</sub>), ethylene (C<sub>2</sub>H<sub>4</sub>), propene (C<sub>3</sub>H<sub>6</sub>), isobutene (i-C<sub>4</sub>H<sub>8</sub>) and 1-butene (1-C<sub>4</sub>H<sub>8</sub>), benzene (C<sub>6</sub>H<sub>6</sub>), and toluene (C<sub>7</sub>H<sub>8</sub>).

As an example, the species mole fraction for the parent fuel and the intermediate products are shown for A2 in Figure 5.2-6 for the first 0.2 ms after fuel enters the kernel. The parent fuel decomposes as soon as it starts entering at 0.09 ms. The intermediate product concentrations peak at about the same time (within 10 μs after fuel is entrained) when the overall reactions becomes exothermic, and then these intermediate products are more rapidly converted on the path to the final products. To better observe the early time species concentration, the species profiles from 0.091 to 0.095 ms are plotted in Figure 5.2-7. Except for the radicals H and CH<sub>3</sub>, the relative concentration ranking of the more stable intermediate species is: ethylene > propene > benzene > toluene > 1-butene > isobutene > methane. Moreover, ethylene and propene account for most of the fuel products. The third species, benzene, has a concentration an order of magnitude below ethylene's.

For the failed C1 case at early times, the stable intermediate concentration (see Figure 5.2-8) rank as: isobutene > propene > ethylene > methane > 1-butene > benzene > toluene, with ethylene's concentration an order of magnitude below that of isobutene. The relative ranking of the C1 intermediate products at early times is consistent for a successful ignition, as seen in Figure 5.2-9 for  $\phi=0.62$ . Thus comparing A2 and C1 at times shortly after the fuel enters the kernel when it begins to decompose, we can see that the relative

concentrations of the fuel intermediates are largely different, and this may be related to the differences in the ignition performance.

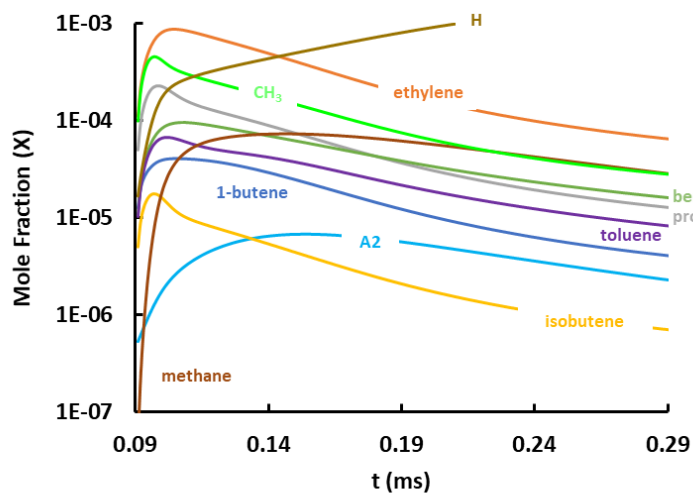


Figure 5.2-6. The mole fraction of the intermediate breakdown products in the kernel as a function of time after the kernel initiation for A2 at  $\phi=0.60$ . The fuel is introduced at 0.09 ms.

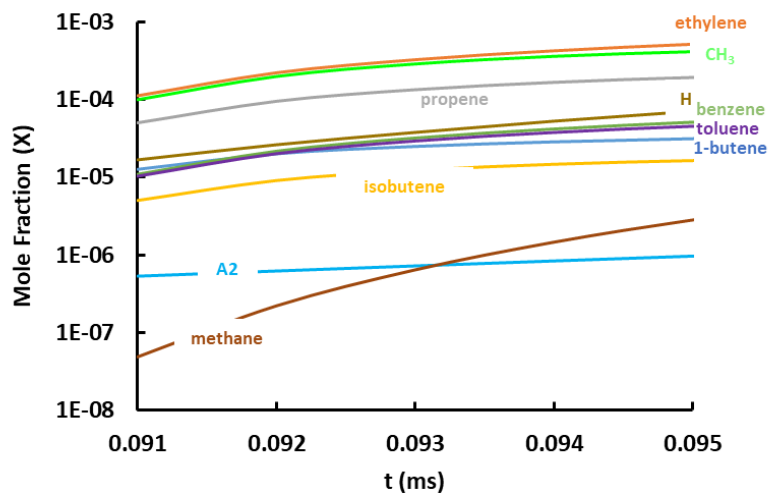


Figure 5.2-7. Intermediate A2 products for early times at conditions of Figure 5.2-6.

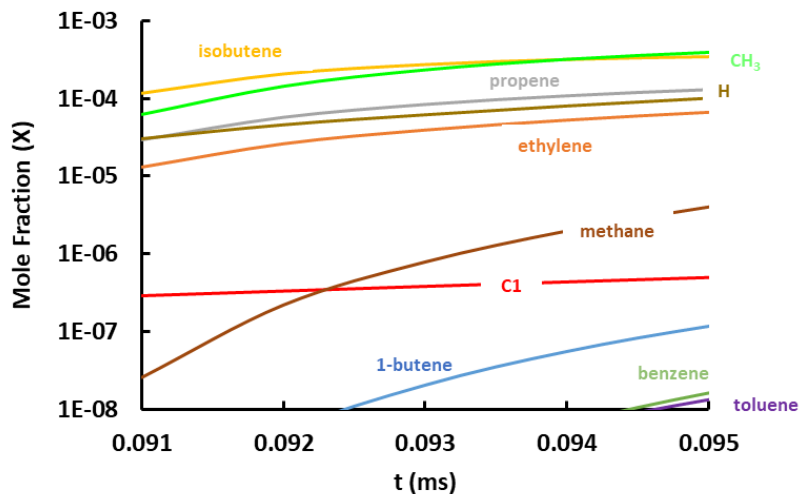


Figure 5.2-8. Intermediate fuel breakdown products for unsuccessful ignition kernel of C1 for  $\phi=0.60$  and early times after fuel introduction.

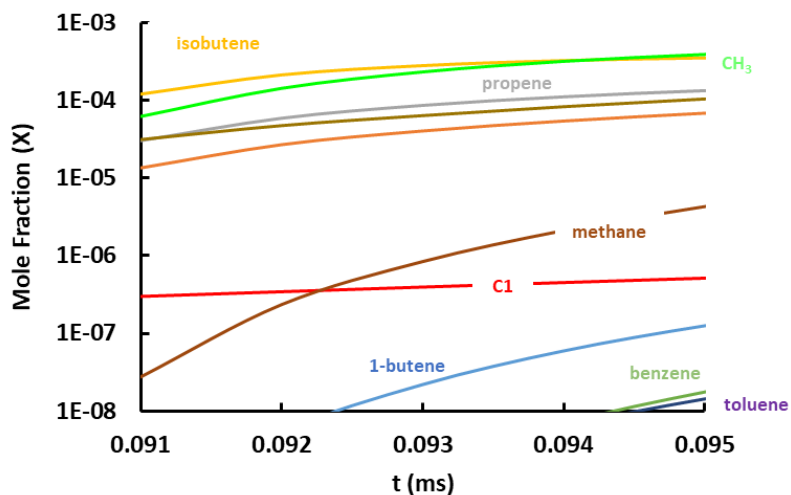


Figure 5.2-9. Intermediate fuel breakdown products for successful ignition kernel of C1 for  $\phi=0.62$  and early times after fuel introduction.

Autoignition of the intermediate species in air can give a preliminary understanding of the intermediates' reactivity. Autoignition simulations in a constant pressure reactor for the seven stable intermediate products were performed at initial temperatures of 1100-1800 K with  $\phi=1$ . The pressure of the reactor is set at one atmosphere, and the fuel mechanism used is USC II [37], which is also the backbone for the HyChem mechanisms. As an example of the autoignition histories, results are shown for benzene and isobutene, at 1400 and 1800 K in Figure 5.2-10. It is interesting to note that at 1800 K the autoignition delays of isobutene and benzene are almost identical. Whereas at 1400 K, the autoignition delay time of isobutene becomes almost five times longer than that for benzene. This shows that the fuel chemistry of some the intermediates should be much more sensitive to the temperature decay of the ignition kernel as it is diluted by entrainment. For example, the simulations presented above suggest the ignition kernel temperatures drops from values above 1800 K to levels approaching 1400 K in cases of successful ignition.

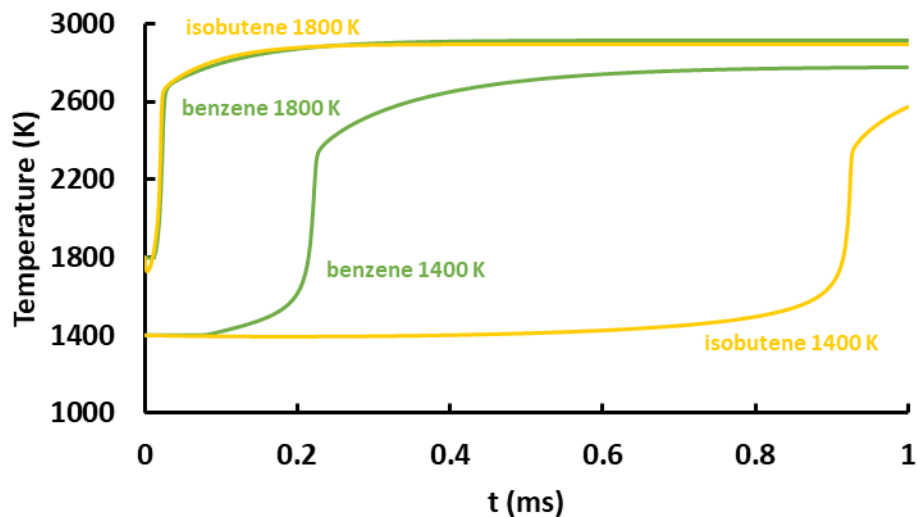


Figure 5.2-10. Autoignition of isobutene and benzene at 1800 K and 1400 K at one atmosphere and  $\phi=1$ .

A full comparison of the autoignition delays for the seven intermediates from 18000 to 1100 K is presented in Figure 5.2-11. At a low temperature like 1250 K, some intermediates (ethylene, benzene, and 1-butene) have relatively short delays, below 1 ms, while others (methane, isobutene, and toluene) have delays above 5 ms. Propene's reactivity is in between these two groups. Furthermore, ethylene has the fastest reactions over the whole temperature range. At high temperatures, such as 1800 K, all the intermediates except methane have autoignition delays below 20  $\mu$ s. So changes in the composition of the intermediates between fuels should have significant impact on the early time chemistry of an entraining kernel, and therefore its ignition success. For example, a fuel like C1 that forms primarily isobutene rather than ethylene (like A2) is less likely to ignite at lower kernel temperatures.

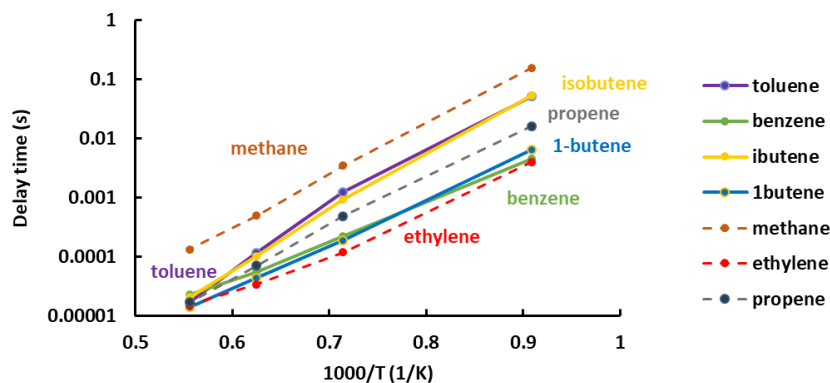


Figure 5.2-11. Autoignition delay time as a function of  $1000/T$  for intermediate species of the products from the original fuel break down



### 5.2.3 Fuel comparison for five fuels: A1, A2, A3, C1, C5

In the previous section, the forced ignition performance of the A2 and C1 fuels were investigated with the reduced order model. In addition to A2 and C1, [36] also provides chemical mechanisms for A1, A3, and C5. Thus the lean ignition limit of the five fuels can be simulated, and the LIL rankings compared to the intermediate product composition. The predicted LIL rankings are shown in Figure 5.2-12, at the conditions indicated in the figure. As lower LIL corresponds to easier ignition, based on the LIL results, the ranking for ignition performance from best to worst goes as: A1 > A2 > A3 > C5 > C1.

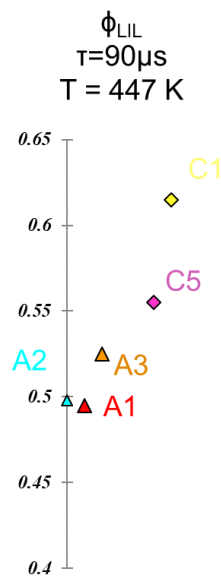


Figure 5.2-12. The lean ignition limit (LIL) for five fuels at conditions like the test conditions, with 90  $\mu\text{s}$  transit time and 60  $\mu\text{g/s}$  mass entrainment rate.

The autoignition study in the previous section showed that ethylene has the fastest chemistry of all the intermediates. Thus, it is possible that the relative amount of ethylene in the intermediates may be used as an indicator of the ignition performance. The early time ethylene concentrations for the five fuels at  $\phi=0.6$  are shown in Figure 5.2-13, for the

same conditions used in Figure 5.2-12. The relative amount of ethylene is consistent with the predicted lean ignition limits, e.g., A1 produces the most ethylene and has the lowest LIL, while the reverse is true for C1. It should be noted that for all these fuels except C1, ethylene is the most abundant of the fuel intermediates produced. Therefore, the ethylene level during early times can be a good indicator of the overall ignition performance. Clearly if two fuels produce similar amounts of ethylene, but it is not the major product, differences in the relative amount of the other intermediates would be important. For example, benzene would be more advantageous than propene.

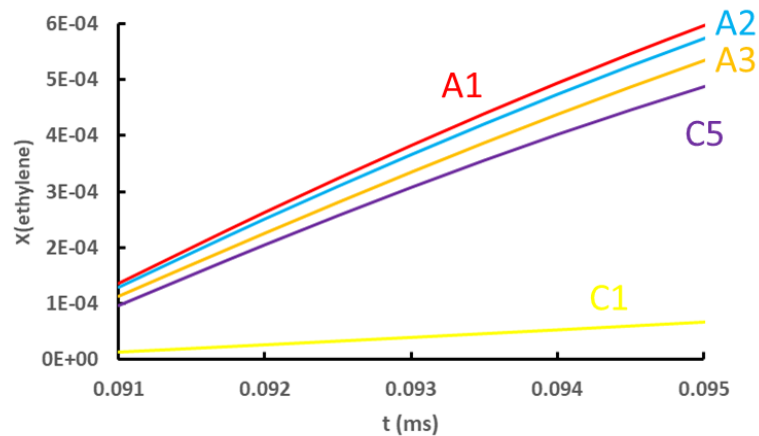


Figure 5.2-13. Ethylene concentration during early times after fuel entrainment for  $\phi=0.6$ .

The simulation results can be compared to the experimental ignition probability rankings shown previously in Figure 5.1-2; there the ranking from best to worst is: C5 > A1 > A3 > A2 > C1. This is similar to the simulations, except A3 was slightly harder to ignite in the simulations. However, the biggest difference is the C5 ranking, which was the easiest to ignite in the experiments, but predicted to be worse than all the A fuels in the modelling.

The conditions used in the above simulations likely do not correspond exactly to the test conditions. Some conditions were carefully measured in the experiments, such as the air and fuel temperatures, and air and fuel flow rates. However, some conditions can only be approximated, such as the time when the kernel starts entraining the fuel/air mixture ( $\tau_{\text{transit}}$ ), and the rate at which the kernel entrains the surrounding fluid. These two uncertain values,  $\tau_{\text{transit}}$  and the mass entrainment rate, can have a large impact on the early kernel temperature, which we have already shown strongly impacts the fuel chemistry. By varying  $\tau_{\text{transit}}$  and the entrainment rate, we can analyze the sensitivity of the lean ignition limit to these two parameters. Such a sensitivity analysis was performed, with one parameter varied at a time. The original simulation entrainment rate was 60  $\mu\text{g/s}$ , and the original transit time was 90  $\mu\text{s}$ . For the sensitivity analysis, the entrainment rate is tested at 30 and 120  $\mu\text{g/s}$  at  $\tau_{\text{transit}}=90 \mu\text{s}$ ; and the transit time is changed from 80  $\mu\text{s}$  to 100  $\mu\text{s}$  at the 30  $\mu\text{g/s}$  entrainment rate. The results are shown in Figure 5.2-14.

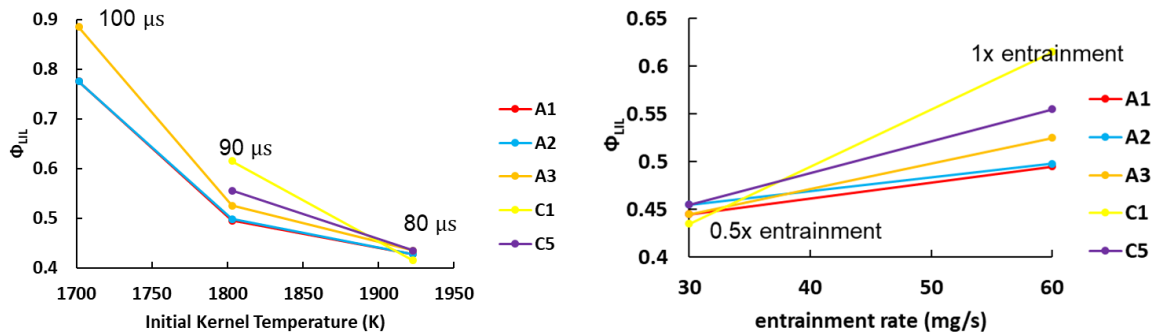


Figure 5.2-14. The left graph shows the sensitivity analysis on the  $\tau_{\text{transit}}$  time while keeping the mass flow rate fixed. The right graph shows the effect of changing the entrainment while keeping  $\tau_{\text{transit}}$  fixed.

As the kernel transit time (left of Figure 5.2-14) is increased to 100  $\mu\text{s}$ , only A1, A2, and A3 were able to ignite as the initial temperature is dropped by  $\sim 100\text{K}$ . At 100  $\mu\text{s}$ , A1

and A2 have the same LIL, while A3's is higher. If the transit time is decreased to 80  $\mu$ s, the differences in LIL also becomes small. This is reasonable as the chemical reaction rates of the intermediates are shown to be similar at high temperature. The sensitivity of C1 to the initial temperature can be attributed to the sensitivity of isobutene to temperature. At high kernel temperature (short transit time), C1 has fast chemistry. At low kernel temperature (long transit time), C1 has slow chemistry.

The effect of varying the entrainment rate is shown in the right graph of Figure 5.2-14. As the entrainment rate is decreased, the dilution cooling rate is also decreased, thus allowing the kernel to stay at higher temperature longer. As the entrainment rate is doubled to 120  $\mu$ g/s, none of the runs can produce a successful ignition. If the entrainment rate is too high, the dilution cooling effect on the kernel will be very strong. Even if a rich mixture is provided, the chemical heat release will never overcome the dilution cooling. C1 is very sensitive to the changes in the entrainment rate. This can again be attributed to the variation in the kernel temperature and the sensitivity to the temperature variations of isobutene, a primary intermediate of C1 decomposition.

The ranking of A1, A2, A3, and C1 matches the experimental results when the entrainment rate is between  $\sim 33$   $\mu$ g/s and  $\sim 37$   $\mu$ g/s. However, in the modeling for C5, its ignition performance is always worse than the A fuels, whereas in the experiments, its ignition performance was always better than all the other fuels. Thus we can conclude the simulations provide reasonable agreement with the experiment for all the fuels except C5. A possible reason is that the C5 fuel decomposition reactions or intermediate product distribution that were determined from shock tube experiments do not extrapolate well to

the higher temperatures existing in the forced ignition kernels. It is recommended to further investigate C5 decomposition at high temperature.

### 5.3 Chapter summary

The forced ignition probabilities of 11 prevaporized fuels were measured. The goal of vaporizing the fuel prior interacting with the spark kernel is to eliminate the effect of liquid fuel vaporization, so that the differences in ignition are purely caused by the differences in the fuel chemistry. Hundreds of ignition events were tested for each fuel at equivalence ratios ranging from 0.6-0.8. The ignition probabilities are shown to increase as the equivalence ratio increases. The fuels are ranked based on the ignition probabilities at  $\phi=0.675$ . Statistically significance differences are observed among fuels, meaning that the fuel chemistry indeed will influence ignition. Fuel C5 has the best ignition probability, and C1 has the lowest ignition probabilities. N-dodecane has similar ignition probability to that of A2. As for the two surrogates, S1 performs better than S2. This result hints that with other compositions being the same, n-deodecane may be more beneficial than n-hexadecane in forced ignition. Although the fuel chemistry is shown to have definite effects on the forced ignition process, the correlations to the major groups of chemical compounds and the derived cetane numbers reveal no clear trend. The reduced order model with the HyChem fuel chemistry is used to simulate the ignition process for the fuels A1, A2, A3, C1, and C5, to understand more of the fuel chemistry effect on the ignition process.

For nominal inputs conditions for the ignition simulation, the fuel A2 is shown to have a lower LIL than the fuel C1. The intermediate species from the parent fuel decomposition

is shown to differ largely for A2 and C1 fuel mechanism. The autoignition delay times of the intermediate species in neat air show that 1-butene, benzene, and ethylene have fast fuel chemistry as the temperature decreases, whereas isobutene, toluene, methane have slow chemistry as the temperature decreases. The LILs for five fuels A1, A2, A3, C1 and C5 are also obtained and the relative ethylene concentration is shown to correlate well to the ignition performance. Through adjusting the entrainment rate, it is possible to match the experimental rankings for all the fuels except C5. Thus, it is also recommended to have C5's fuel decomposition mechanism at high temperature reexamined.

## **CHAPTER 6:**

### **FORCED IGNITION OF LIQUID JET FUEL**

In the previous chapter, the ignition performance of prevaporized fuels was examined through experiments and reduced order modeling. The differences in relative amounts of the intermediate products produced from the parent fuels were shown to have a strong effect on the chemical kinetics and the heat release rate. The prevaporized ignition work demonstrated the impact of fuel chemistry on forced ignition. However, for aviation turbine engines, the fuels are injected into the combustor in the form of liquid sprays. The jet fuel needs to atomize and vaporize before the chemical reactions can produce heat release at offset the dilution cooling of the kernel. This phase transition adds complexity to the forced ignition process. In this chapter, the ignition performances of various fuels are first investigated by measurements of ignition probabilities. The droplet distribution measurements are presented. The detailed size distribution can help future CFD modeler when implementing detailed CFD simulations. A reduced order model that incorporates the droplet heating and vaporization is the used to study the effect of droplets on the ignition process. The effect of droplet distributions is investigated through the Rosin-Rammler relation.

#### **6.1 Ignition probability ranking**

As in the prevaporized study, average ignition probabilities were obtained based on more than 1000 spark events per fuel, and each fuel's ignition probability is scaled relative to the probability of A2. The methods for obtaining the uncertainty bars and probability

scaling are describe in §3.3, and the absolute ignition probabilities for each fuel are given in Appendix G.

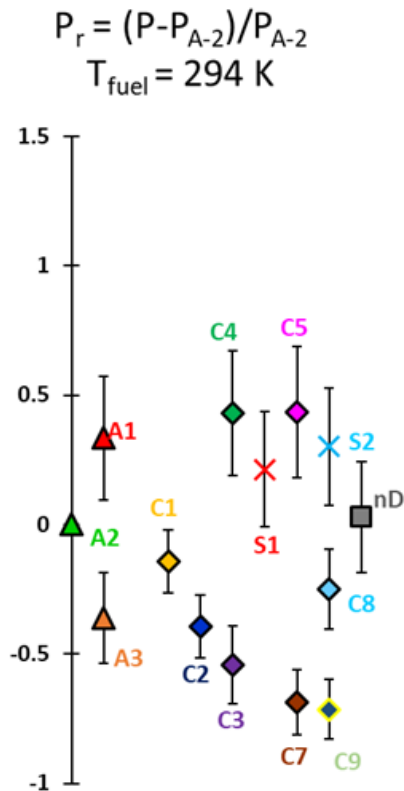


Figure 6.1-1. Probability ranking with probabilities scaled to the probability of A-2, with probabilities acquired under test conditions in Table 2 for room temperature fuels.

The results for ten room temperature fuels are shown in Figure 6.1-1, with uncertainty bars indicating the 68% confidence ( $1\sigma$ ) level. For comparison, ignition probability results for uniformly distributed, prevaporized fuels are shown in Figure 5.1-2. In the case of prevaporized mixtures, physical effects relating to vaporization and fuel distribution are removed, so chemistry differences between fuels should dominate.



Several differences can be noticed when comparing probabilities from the liquid and gaseous ignition tests. For the liquid sprays, fuels C2 and C3 have lower ignition probabilities than C1, whereas in the gaseous case, C2 and C3 have higher probabilities than C1. The prevaporized modeling suggested the low ignition probability of C1 could be caused by high concentration of isobutene as an intermediate breakdown product. In the case of liquid spray, however, C1 is easier to ignite than C2 and C3. Another fuel with significant change in ignition performance is S2. The major difference between S1 and S2 is that S1 is blended with ~50% of n-dodecane, while S-2 is blended with ~50% of n-hexadecane. The other 50% of the compositions are the same for S1 and S2. This suggests the physical fuel properties associated with the change in the straight chain alkane are the source of the significant difference in liquid spray versus prevaporized ignition. Finally, A3 has a higher ignition probability than A2 when prevaporized, but A3's ignition probability is lower for the liquid fuel spray.

To simulate cold startup conditions, the liquid fuels were also chilled to 246 K, and the resulting relative ignition probability rankings for the chilled fuel spray are shown in Figure 6.1-2. The chilled results include less fuels than the room temperature data. The reason for not testing some fuels at chilled conditions is that the freezing temperatures for the untested fuels are too high; these fuels will freeze at the bath temperature of the fuel chilling system.<sup>4</sup> For the fuels tested, the range of the relative ignition probabilities for the chilled fuels (-1.5 to 4.5) is larger than the range of the room temperature ignition probabilities (-1 to 1.5); still the relative rankings of the chilled fuel probabilities are generally consistent with the

---

<sup>4</sup>Using a higher bath temperature would not allow these fuels to be chilled to the required temperature at the point of fuel injection.

room temperature rankings. The C3 and C7 fuels rank slightly higher (close to A3) in the chilled fuel case, though this may result in part from the inability of the experiment to differentiate between the very low ignition probabilities that occur for these fuels under the chilled conditions, as evidenced by the increased relative uncertainties compared to the spread of ignition probabilities.

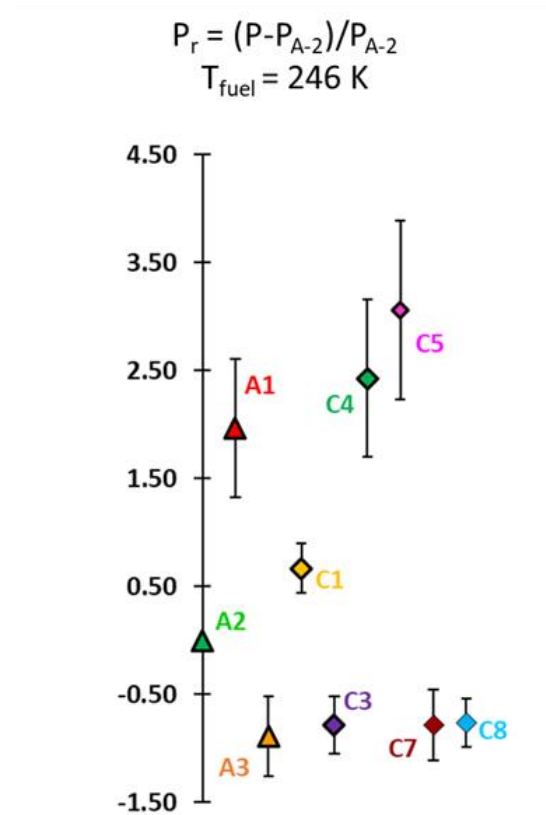


Figure 6.1-2. Probability ranking with probabilities scaled to the probability of A2, with probabilities acquired under test conditions listed in Table 2 for the chilled fuels.

As a start, we can analyze the impact of fuel temperature on ignition probability by considering the behavior of the fuel viscosity. Chilling the fuels should increase their viscosities. According to Equation 10, increasing the fuel viscosity will tend to increase the droplet size, and this in turn might be expected to hinder ignition (as per Equation 1).

The viscosities of different fuels respond differently to temperature changes. Given two viscosities at two temperatures, ASTM D341 [42] can help predict viscosities at other temperatures. A python code that uses ASTM D341 to predict viscosity as a function of temperature is provided in Appendix F.

The calculated viscosities as a function of temperatures for a selection of the fuels is shown in Figure 6.1-3. The viscosity of fuel C3 is the most sensitive to temperature, while C5 has the least sensitive viscosity. For a fuel temperature around 294 K, according the SMD equations (Equation 10), viscosities will contribute to a  $(5/2)^{0.25}=1.25$  times bigger droplet diameter for the high viscosity fuel (C3) than the low viscosity fuel (C5). When the temperature is lower, the high viscosity fuel will have a  $(12/3)^{0.25}=1.41$  times bigger droplet diameter than the low viscosity fuel. Thus the larger spread in ignition probability for the chilled data compared to the room temperature case can be a result of the larger differences in droplet sizes as the fuel temperature is decreased.

In most cases, the relative ranking of the fuel viscosities does not change as the temperature is decreased. This is also consistent with the experiments, where the ignition probability rankings were essentially the same for both fuel temperatures. For C1, however, the viscosity increases more as the temperature is decreased, compared to the other fuels. This should increase droplet size and would be predicted to make ignition more difficult; compared to the room temperature data, however, C1's relative ignition ranking when chilled improves slightly. It should be noted that changes in fuel viscosity can also impact the spatial distribution of the fuel produced by the nozzle; this could also influence ignition probability by changing the amount of fuel in the region near the igniter.

Surface tension can also have a strong effect on the spray and droplet atomization process. However, the differences in surface tension among fuels are small (see Appendix A). Therefore, the variation in the surface tension is not expected to vary the droplet size much.

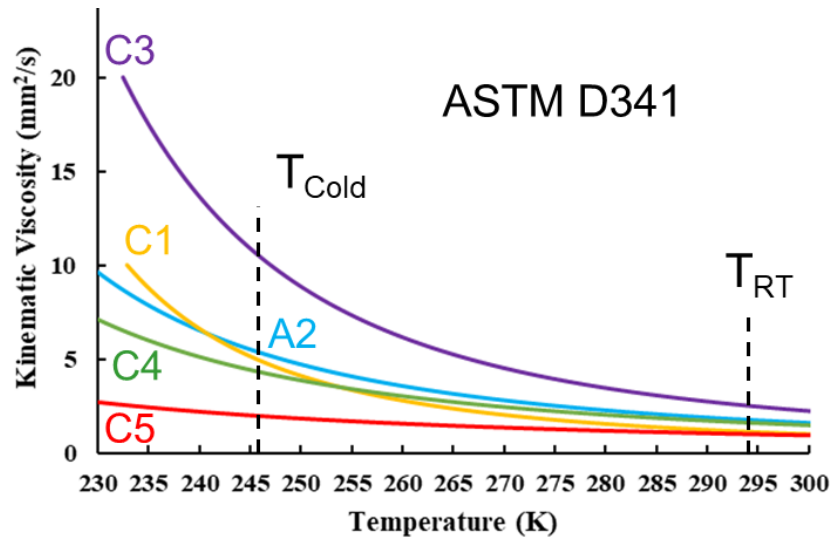


Figure 6.1-3. Viscosities versus temperature for a few fuels studied in this program. ASTM D341 is used to predict viscosities at different temperatures.  $T_{\text{cold}}$  is the temperature of the tested chilled fuels, and  $T_{\text{RT}}$  is the temperature of the tested room temperature fuels.

In summary, we see that the relative ignition probability rankings for some fuels are significantly different in fuel sprays than in prevaporized conditions. For example, C1 had the lowest ignition probability when prevaporized, but its probability ranks higher when C1 is ignited as a spray. As for liquid fuel sprays at different temperatures, fuel viscosities are shown to be influenced by temperature significantly. Droplet sizes are affected by the change in viscosity, with an increase in viscosity tend to increase the droplet sizes. A comparison of the ignition probabilities between those for the room temperature sprays and those for the chilled fuel sprays shows that the range of ignition probabilities is wider for the chilled fuel spray than for the room temperature fuel. The increased variation in fuel

properties at a low temperature is likely the cause of the increased variation in ignition probabilities.

## **6.2 Droplet distribution measurement**

The comparison presented above were for the same global conditions, e.g., fuel temperature and equivalence ratio. However, local conditions where the spark kernel interacts with the fuel are likely important to the success of ignition. For example, differences in local fuel concentration and droplet size would likely cause differences in ignition behavior. This likely motivated Lefebvre [9] suggestion, “It is strongly advised that in future experimental studies on fuel effects every effort should be made to determine mean drop size and drop-size distribution for all fuels over wide ranges of combustor operating conditions.”

Therefore, to answer Lefebvre’s call to better understand local conditions, the particle size and velocity distributions for the room temperature fuel tests were measured with a Phase Doppler Analyzer (PDPA). The PDPA records the size and velocity at a single point location. A translational stage is used to move the PDPA system so that different points in space can be scanned. For this research, the primary goal of measuring droplet statistics is to provide more detailed droplet information for future CFD modeling. In addition, the PDPA measurement gives the relative droplet distribution with respect to the kernel trajectory. Also, the measured sizes can help the validity of the empirical SMD equation (Equation 10).

The locations of measurements are shown in Figure 3.5-3. The measurements are taken for fuels A2, C1, C3, C5 and C9. The objectives of this section are to show the symmetry

of the spray and to show the correlation between the measured droplet sizes and the empirical SMDs. Also, not all measured data are included in this thesis as tens of thousands of droplets are captured for hundreds of locations. But the raw data are available upon request to the author or the author's advisor – Dr. Jerry Seitzman. The PDPA measurements for fuel C3 are taken in the transverse and span-wise directions ( $r$  and  $r'$  directions) at 10 mm downstream.

The spanwise and transverse profiles of SMD ( $D_{32}$ ) at an axial location 10 mm downstream of the nozzle are shown in Figure 6.2-1 for fuel C3. The edge of the spray is defined when less than 50 droplets are captured within an 8 second measurement span. The origin is defined at the point where the centerline of the nozzle intersects the cross-section. The SMD values in the transverse direction show better symmetry than in the spanwise direction. Traversing the PDPA system in the spanwise direction will change the laser beam quality. The droplets at the center are smaller than the droplets at the outer edge of

the spray. The radius of the spray at the 10 mm plane is approximately 10 mm. Therefore, the spray cone angle is approximately 90°.

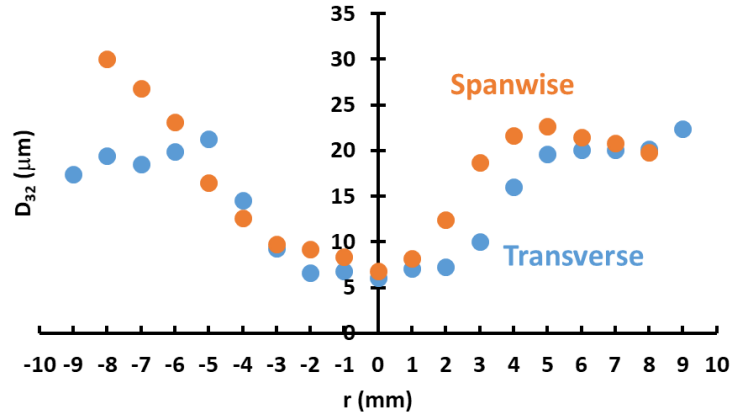


Figure 6.2-1. Sauter Mean Diameter (SMD) profiles in the spanwise and transverse directions at the plane 10 mm downstream of the nozzle for fuel C3. The origin is defined at the point at which the center line intersects the cross-section.

The center of the igniter is in a plane 30.4 mm downstream of the fuel nozzle. Transverse SMD profiles for all five fuels tested are shown in Figure 6.2-2. The variations in droplet sizes among fuels are strongest near the center and edge of the spray. The spray cone angles are also slightly different. Fuels that produce larger droplets have slightly larger cones, as the larger droplets are harder to slow down.

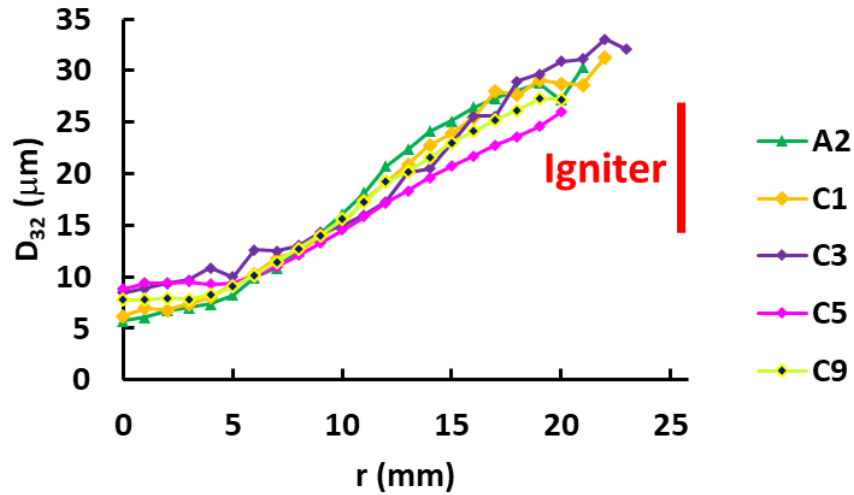


Figure 6.2-2. Transverse SMD ( $D_{32}$ ) profiles at the plane 30.4 mm downstream of the nozzle. The origin is defined at the point at which the center line intersects the cross-section. The red line indicates the position of the igniter.

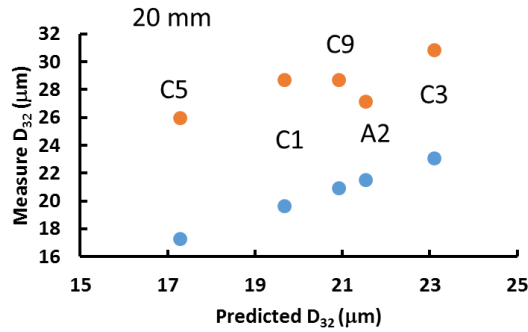


Figure 6.2-3. The measured  $D_{32}$  versus the predicted  $D_{32}$  at 5.8 mm above the igniter in the 30.4 mm plane.

The SMD data at 5.8 mm above the igniter in the 30.4 mm plane are compared to the values predicted by Equation 10 in Figure 6.2 3. The droplets close to the igniter will interact with the spark kernel when the spark kernel is at high temperature. The measured droplet SMD values are larger than the predicted sizes; this is due, at least in part, to the small droplets near the center of the spray not being included in the experimental value. Except for A2, the trend of the measured droplets match that of the predicted droplets. The



cause for A2 to be a significant outlier is unclear. Potential source of error can be the randomness in the spray formation, inconsistent laser quality, or contaminated window. In future studies, capturing multiple, repeatable data for each fuel is necessary.

In addition to average droplet sizes, the PDPA provides size distribution results. Example number distributions for the five fuels at 5.8 mm above the igniter in the 30.4 mm plane downstream of the nozzle are shown in Figure 6.2-4. All distributions can be modeled by the Rosin-Rammler relation as in Equation 16 for easier application in modeling. An example Rosin-Rammler regression check for A2 in Figure 6.2-4 is presented in Figure 6.2-5, and good fitting is obtained.

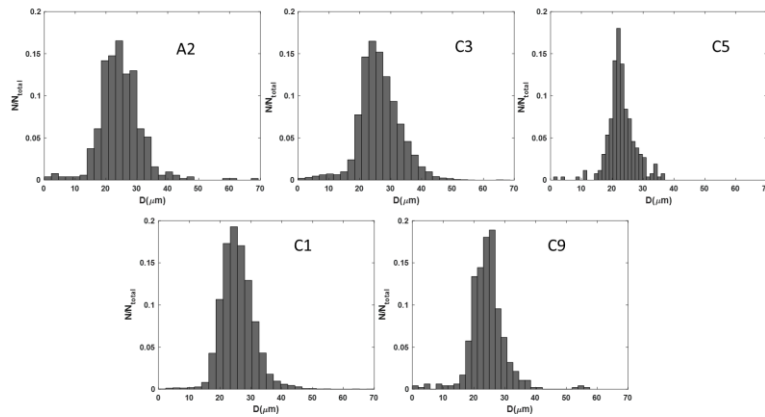


Figure 6.2-4. Droplet size number density distribution at 5.8 mm above the igniter center in the 30.4 mm plane downstream of the nozzle. Normalized by the total number of droplets captured.

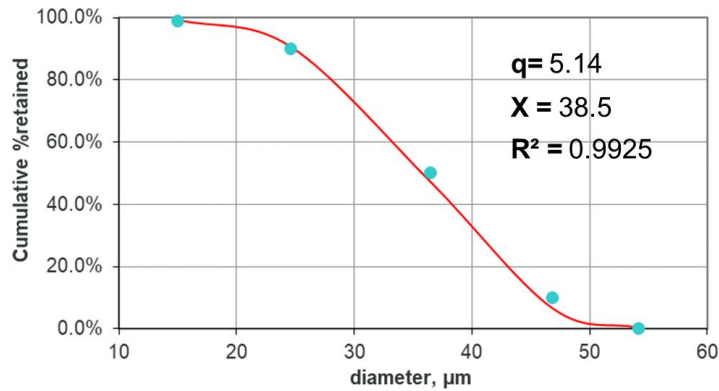


Figure 6.2-5. Rosin-Rammer fitting for A2 in Figure 6.2-4.

### 6.3 Probability correlations

The preceding analysis noted the possible importance of viscosity on ignition of fuel sprays, based on its influence on droplet size. As noted in Chapter 1, droplet heating and vaporization can be expected to be important for ignition, thus any physical properties that influence droplet atomization and vaporization will likely affect ignition. In addition, the fuel chemistry can also be important. Thus, this section investigates the correlation of ignition probability to various fuel properties.

#### 6.3.1 Correlations to single properties

The correlation between the ignition probabilities of the room temperature sprays and DCN is shown in Figure 6.3-1. No clear relation between the ignition probabilities and DCN can be seen, despite the large range of DCN values represented by the fuels. Figure 6.3-2 shows the correlation between ignition probability and fuel density. Again, no clear

correlation is evident. It may appear that fuels with higher densities seem to give lower probabilities, which is consistent with Equation 10, since larger densities are expected to produce larger droplets. However, without C3 and C7 included in the analysis, the ignition probability shows little dependence on density; for example the full range of probability is observed for two fuels with the same density (C5 and C9). Still, it is important to point out the relative variation in density among the fuels is small; thus the effect of density may not be observable.

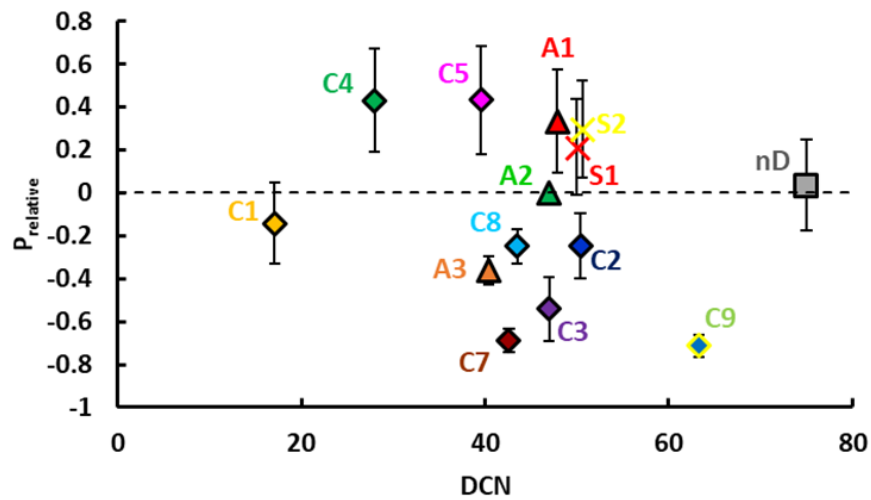


Figure 6.3-1. The relative ignition probabilities versus DCNs for ignition of room temperature fuel sprays.

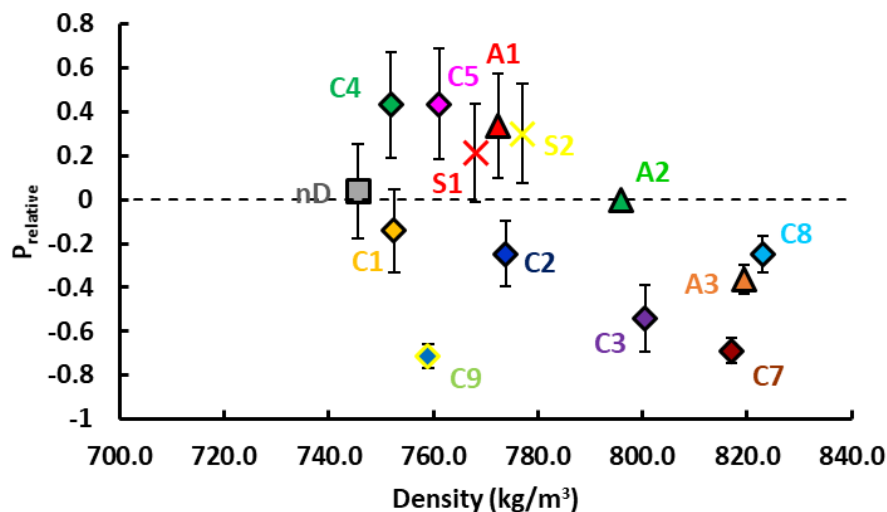


Figure 6.3-2. The relative ignition probability versus fuels' density at 15 C for ignition of room temperature fuel sprays.

Nonetheless, some fuel properties do show strong, and quasi-linear, trends when plotted against ignition probability. The linear correlation indexes for select properties are shown in Figure 6.3-3. Of the fuel properties whose values are available from the data provided by the NJFCP, those that have the strongest influence include the 10% recovery temperature (Figure 6.3-4) and the viscosity (Figure 6.3-5). The viscosity dependence relates to the previously suggested relationship to atomization and droplet size. A lower viscosity tends to produce smaller droplets, which can reach the vaporization temperature sooner during the heat up process. In addition, viscosity and droplet size can impact the spatial distribution of fuel downstream of the atomizer. Recovery temperature (or vapor pressure) will also influence the vaporization rate of the fuel. For example, a lower value for the 10% recovery temperature or a higher vapor pressure indicates the fuel will be easier to vaporize when interacting with the hot kernel, which is required to initiate chemical

reactions. The effect of choosing the recovery temperature is later explored with the reduced order model.

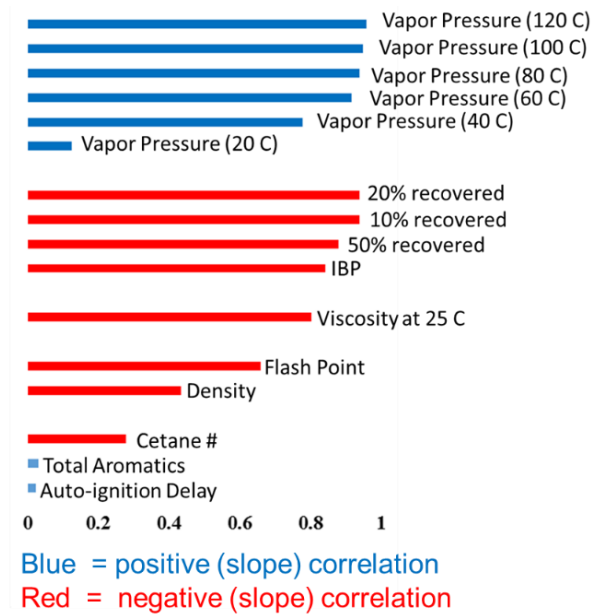


Figure 6.3-3. The linear correlation indexes between the ignition probability and the properties.

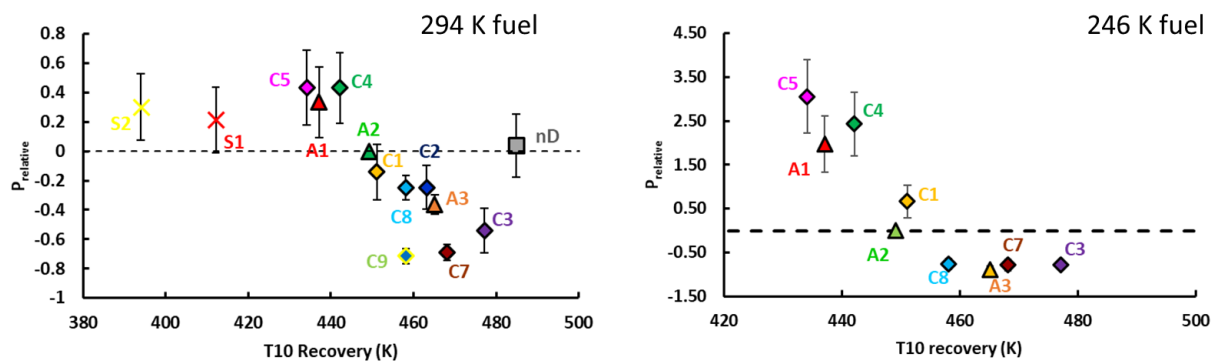


Figure 6.3-4. Relative ignition probabilities versus the 10% recovery temperature.

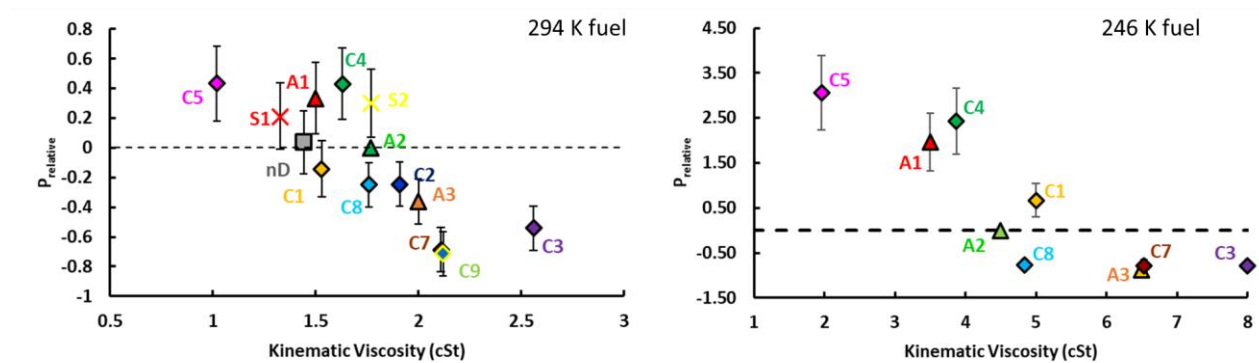


Figure 6.3-5. Relative ignition probabilities versus the kinematic viscosities.

### 6.3.2 Correlation to physical models

These strong correlations of ignition probability to properties that relate to droplet size give confidence to our earlier hypothesis that forced ignition of liquid fuel sprays can be controlled by droplet heating and vaporization. Having this confidence in the effect of droplets on ignition, we can explore more advanced correlations, including the correlation to droplet sizes, the correlation to the empirical lean light off (LLO) limit as in [9], and the correlation to the minimum ignition energy in a single size, uniformly distributed droplet array.

The correlation of the ignition probabilities to the droplet sizes predicted by Equation 10 is shown in Figure 6.3-6. A clear trend can be observed between the ignition probabilities and the SMDs calculated with Equation 10. As the droplet size increases, the ignition probability decreases. The increase in droplet size means the time required to heat the droplet to a temperature where vaporization is rapid will be longer, as the initial liquid temperature is lower than the recovery temperatures. However, the rate of mass loss will be faster for larger droplets once they reach these vaporization temperatures. C9 is an

outlier in the droplet size dependence. In addition to the physical process that is strongly affected by the droplet sizes, fuel chemistry may also impact the ignition process for liquid fuel sprays. The correlation between ignition probability and droplet size becomes stronger for the chilled data, where the predicted droplet sizes (and range) are also larger.

The droplet heating time and vaporization rate can both influence the ignition process. Therefore, the correlations to the heating times and the vaporization rates should also be investigated.

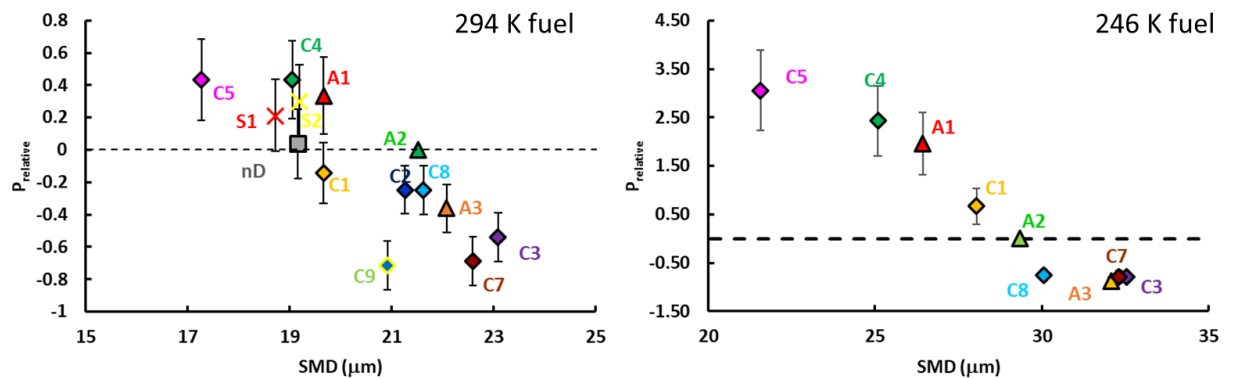


Figure 6.3-6. Relative ignition probabilities versus 10% recovery temperature. Left: fuel spray at 294 K; Right: fuel spray at 246 K.

To get a preliminary understanding of the effects of the droplet heating time and the rate of vaporization, we can first use simple heating and vaporization models and observe how the ignition probabilities correlate to heating and vaporization. For heating, as the droplets sizes are small, the infinite diffusivity heat transfer model [43] can be used. To simply investigate the effect of heating times on ignition, we can ignore the vaporization during the heat up period. The vaporization during the heating up period will make the heat up time longer as part of the heat transferred to the droplet is used for vaporization. With the assumption of no vaporization during heating and treating the liquid droplet as a solid

sphere, an analytical solution of the heat up time can be calculated using the lump analysis [cite a heat transfer book] as

$$t_{heat\ up} = -9 \times \ln\left(\frac{T_{boil} - T_{kernel}}{T_i - T_{kernel}}\right) \times \frac{Nuk_{air}}{\rho c_{p,l}} \times \left(\frac{D}{2}\right)^2 \quad (24)$$

where  $T_{boil}$  is the boiling temperature,  $T_{kernel}$  is the temperature of the spark kernel,  $T_i$  is the initial temperature of the droplet,  $k_{air}$  is the thermal conductivity of the air,  $\rho$  is the density of the liquid,  $c_{p,l}$  is the heat capacity of the liquid, and  $D$  is the droplet diameter.

In the following analysis,  $D$  is based on the calculated SMD (as in Figure 6.3-6). The kernel temperature is assumed to be at 1600 K, with the initial fuel temperature at 294 K and 246 K. For a non-vaporizing droplet, the layer of mixture near the droplet, commonly referred to as the “film,” will consist of air only. For a pure air film, the Nusselt number can be approximated using T. Yuge’s [44] heat transfer model for a solid sphere, which is

$$Nu = 2 + 0.43Ra_D^{1/4} \quad (25)$$

where  $Ra_D$  is the Rayleigh number and its calculation can be found in [44].

The results of the correlation between the ignition probability and heating time are shown in Figure 6.3-7. In Equation 24, the heating time is proportional to  $D^2$ . Thus, larger droplets will have longer heating times, though the final boiling temperature will also have an effect. The longer heating time will lead to lowered ignition probabilities, as evidenced



in both the room temperature and chilled fuel cases (Figure 6.3-7). The heating times of the room temperature droplets are longer than the heating times of the cold droplets. The low initial temperature of the droplets will tend to increase the heating time of the droplets. As the heating time of the droplets are longer, the droplets will not vaporize quickly until later times. During this droplet heat up period, the spark kernel will continue to be cooled and diluted by entrainment. Fuel C9 is an outlier as in the left graph in Figure 6.3-7. The C9 fuel has a lower ignition probability while its heating time is shorter. In this calculation, the 10% recovery temperature is used as the boiling temperature. However, as these jet fuels consists of a large variety of chemical compositions, different fuel components will vaporize at different temperatures. Thus, a different recovery temperature may make the C9 fit better.

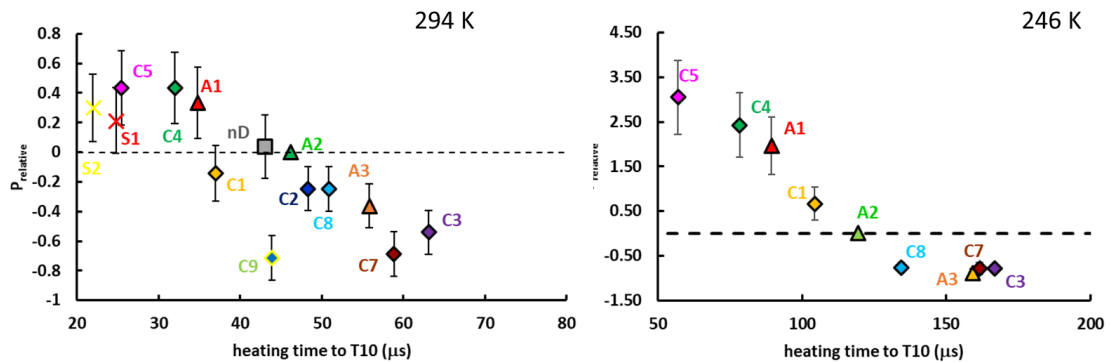


Figure 6.3-7. The heating time to the 10% recovery temperature. The droplets are placed in 1600 K quiescent air, and the initial temperatures of the droplets are 294 K (left) and 246 K (right). The droplet sizes for each fuel are predicted by Equation 10.

The correlation to the heating time to the 20% and 50% recovery temperatures are shown in Figure 6.3-8 and Figure 6.3-9. If the percentage recovered is higher, then the recovery temperature will also be higher. Longer times are required for the droplets to heat to a higher recovery temperature. For the 20% recovery temperatures in Figure 6.3-8, both

the 294 K and the 246 K droplets still shows good correlation between the ignition probabilities and the heating times. However, for the 50% recovery temperatures in Figure 6.3-9, the correlations are becoming less obvious, manifested through the shifts in C1 and n-dodecane. This result indicates that the lower recovery temperature will have a more dominant effect on ignition than the higher recovery temperatures have.

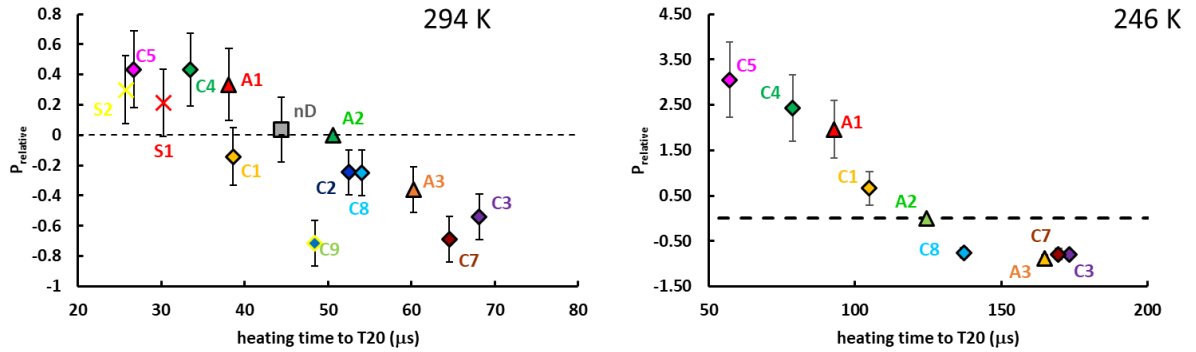


Figure 6.3-8. The heating time to the 20% recovery temperature. The droplets is placed in 1600 K quiescent air, and the initial temperatures of the droplets are 294 K (left) and 246 K (right). The droplet sizes for each fuel are predicted by Equation 10.

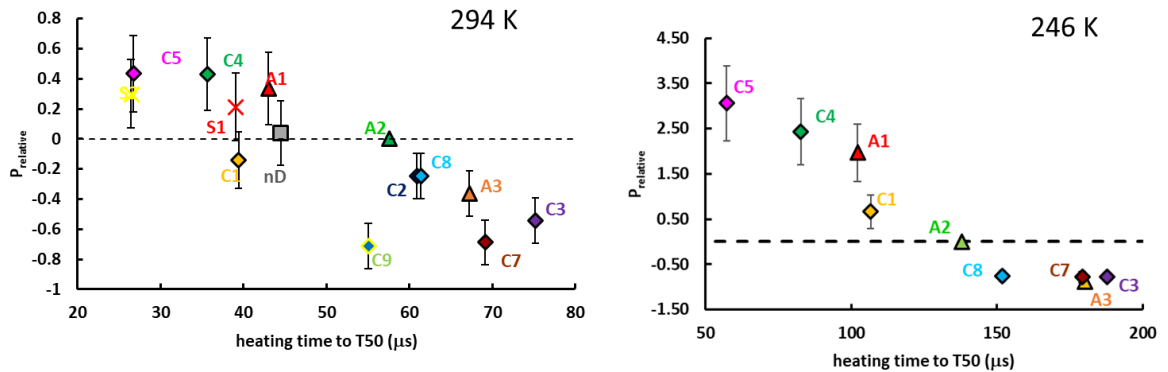


Figure 6.3-9. The heating time to the 50% recovery temperature. The droplets is placed in 1600 K quiescent air, and the initial temperatures of the droplets are 294 K (left) and 246 K (right). The droplet sizes for each fuel are predicted by Equation 10.

In addition to droplet heating, droplet vaporization can also influence ignition. The effect of the droplet vaporization can be seen from the effective vaporization rate. The effective vaporization rate in Lefebvre's work [9] is defined as

$$\lambda_{eff} = \frac{8k/c_p \ln(1+B)(1+0.22Re^{0.5})}{\rho_F} \quad (26)$$

where  $k$  and  $c_p$  are the thermal conductivity and the specific heat at constant pressure for the gaseous mixture,  $Re$  is the Reynolds number of the droplet,  $\rho_F$  is the density of the fuel in liquid form, and  $B$  is the Spalding transfer number. The Spalding transfer number can be calculated as

$$B = \frac{c_p(T_{env} - T_{boil})}{h_{fg}} \quad (27)$$

where  $T_{env}$  is the ambient temperature,  $T_{boil}$  is the boiling temperature, and  $h_{fg}$  is the heat of vaporization. Since the vaporization rates of various fuels are investigated,  $\lambda_{eff}$  can be scaled to that of A2 to simplify calculation. The scaled effective vaporization rate will be termed  $\lambda_r$ , and  $\lambda_r$  is calculated as

$$\lambda_r = \frac{\lambda_{eff}}{\lambda_{eff,A2}} = \frac{\ln(1+B)\rho_{F,A2}(1+0.22Re^{0.5})}{\ln(1+B_{A2})\rho_F(1+0.22Re_{A2}^{0.5})} \quad (28)$$

where  $B_{A2}$  and  $\rho_{F,A2}$  are the Spalding number and density of fuel A2. If we further assume the relative velocity between the droplet and the free stream is small, the Reynolds numbers are negligible. The expression for  $\lambda_r$  can then be simplified to be

$$\lambda_r = \frac{\ln(1 + B)\rho_{F,A2}}{\ln(1 + B_{A2})\rho_F} \quad (29)$$

The results for the correlation between  $\lambda_r$  and ignition probability are shown in Figure 6.3-10 for an ambient temperature of 1600 K. The 10% recovery temperatures of the fuels are used as the boiling temperatures for calculating the  $B$  values. While the variations in  $\lambda_r$  are small, there is some evidence of an increase in ignition probability with higher relative effective evaporation constant (A1 and C9 the biggest outliers).

The relative effective vaporization defined in Equation 29 accounts for the physical properties such as the boiling temperatures and the densities of the fuel. In addition, the droplet size will also play an important role in vaporization. As noted previously, larger droplets have higher mass vaporization rates than smaller droplets, because they have more surface area. To account for the effects of droplet sizes and chemistry, we can turn our

attention to Lefebvre's empirical expression (Equation 1), which includes terms for droplet size and chemistry.

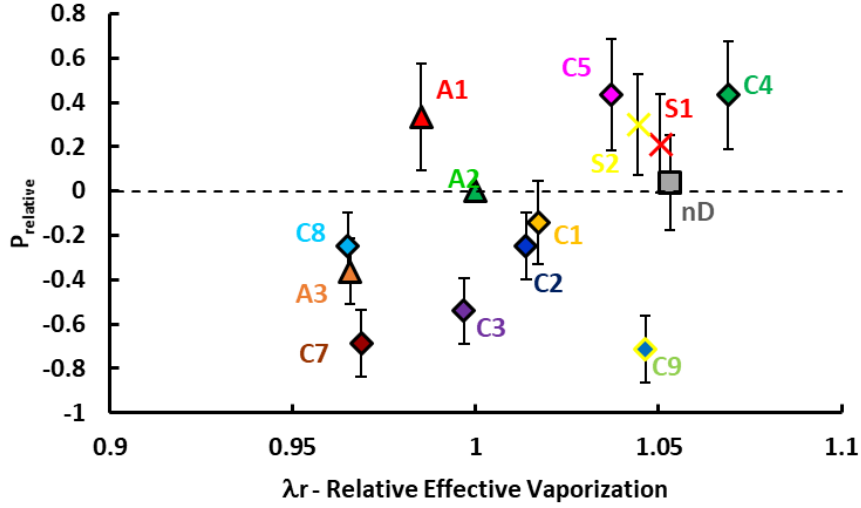


Figure 6.3-10. The relative ignition probabilities versus the relative effective vaporizations calculated with Equation 29. The ambient temperature is 1600 K.

To simplify calculation, we will look at the relative lean ignition limits with respect to that of A2. With the same approach used in obtaining  $\lambda_r$ , the relative lean ignition limit can be calculated by finding the ratio with respect to the lean ignition limit of A2, and the result is

$$f_{LLO,r} = \frac{D^2 \lambda_{r,A2} LHV_{A2}}{D_{A2}^2 \lambda_r LHV} \quad (30)$$

where  $D$  is a representative droplet size,  $\lambda_r$  is the relative vaporization as in Equation 29, and  $LHV$  is the lower heating value. The correlations between the relative ignition probabilities and the relative LLO limit is shown in Figure 6.3-11. The ignition probabilities correlate well with the LLOs for both the room temperature fuels and the

chilled fuels; higher LLOs correspond to lower ignition probabilities. The vaporization constants and the heating values of the fuels vary slightly among the fuels. The trend shown in Figure 6.3-11 for LLOs resembles the trend shown in Figure 6.3-6 for the droplet sizes. In fact, the differences in the LLOs are mainly controlled by the differences in the droplet sizes.

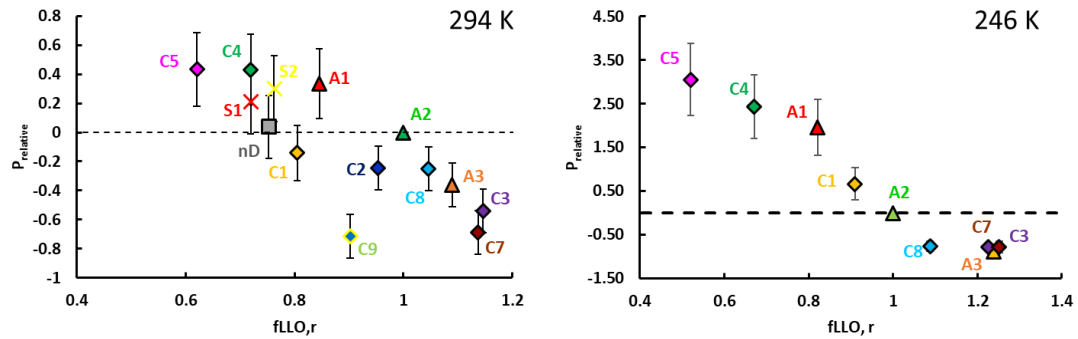


Figure 6.3-11. Relative ignition probability versus relative lean ignition limits calculated with Equation 30.

### 6.3.3 Summary

In this section, the correlation of forced ignition probability to single properties of liquid fuels and to various physical models was explored. It is found that DCN is not a good indicator for forced ignition performance in liquid jet fuels. Fuel density also show poor (or weak) correlation to ignition probability, at least based on the small range of densities seen in jet fuels. Strong correlations to viscosity and recovery temperatures are observed, which follows from their impact on droplet heating and vaporization. Based on their strong correlation to the measured forced ignition probabilities, the droplet sizes,

heating times, and vaporization rates seem to be the controlling processes impacted by the fuel properties.

The SMDs shows good correlation to the ignition probabilities. Larger SMDs will have lower ignition probabilities. Larger droplets will be more difficult to heat up. The heating time to various recovery temperatures are investigated assuming no vaporization during heating. The ignition probabilities show good correlations to the heating times corresponding to the 10% and 20% recovery temperatures, while the correlations are weaker for the heating times to the 50% recovery temperatures. The heating time to the lower recovery temperatures seems to have a stronger impact than the heating time to the higher recovery temperatures.

The vaporization rates of the droplets are investigated through the effective vaporization constant,  $\lambda_{eff}$ . The variations in  $\lambda_{eff}$  are small, and no strong correlation between the ignition probabilities and  $\lambda_{eff}$  is observed. The correlation to the lean ignition limit,  $f_{LLO}$ , is also investigated. The  $f_{LLO}$  expression includes the droplet sizes and the  $\lambda_{eff}$ . The correlation to the  $f_{LLO}$  resembles the correlation to the droplet sizes. The droplet sizes have dominant effect on  $f_{LLO}$  and the ignition outcome.

## **6.4 Reduced order simulation**

In the previous section, the factors that may affect the forced ignition process are correlated to the experimental values of the ignition probabilities for various fuels. The calculated droplet diameter is found to have a strong correlation to the measured ignition probability. With the reduced order model presented in §3.6.2, this section investigates the effect of the droplet sizes, the effect of the fuel temperature and the air temperature, the

effect of different fuels, the effect of fuel/air ratio, and the effect of droplet distribution. The python code used in this study is given in Appendix D.

#### 6.4.1 Model validation

Before examining any model predictions, it is important to ascertain if the model captures basic trends found in experimental results. As introduced in §3.6, the droplet ignition model consists of two parts: 1) the two-stage PSR model that simulates the spark kernel entrainment and chemistry, and 2) the droplet heating and vaporization model. The two-stage PSR model was previously validated by successfully predicting experimental data in [8]. The droplet heating and vaporization model for a single droplet is also validated by comparing results in §3.6.2.1 to results in [40]. To further validate the model, we can compare the model result to the  $f_{LLO}$  in Equation 1. For a single fuel,  $f_{LLO}$  is a function of the droplet size and the vaporization constant. For a constant  $f_{LLO}$ , the change in droplet size due to the variation in the boiling temperature can be expressed as

$$\begin{aligned} & \frac{D_1^2}{\ln(1 + \frac{c_p(T_{env} - T_{boil,1})}{h_{fg}})} \\ &= \frac{D_2^2}{\ln(1 + \frac{c_p(T_{env} - T_{boil,2})}{h_{fg}})} \end{aligned} \quad (31)$$

Assuming the environment temperature of 1600 K and choosing the boiling temperature to be 433 K, 453 K, and 493 K, we can compare the scaling in  $f_{LLO}$  to the scaling from the model results as in §6.4.5. If 453 K is matched to 12.5  $\mu\text{m}$  diameter, 433 K is matched to 12.54  $\mu\text{m}$ , and 493 K is matched to 12.41  $\mu\text{m}$ . Compared to Figure 6.4-13,



the model is able to predict the correct trend: higher boiling temperature will require smaller droplets. However, the model predicts a much strong sensitivity of the droplet size to the boiling temperature compared to that predicted by the  $f_{LLO}$ . To find the reason for the mismatch, we will investigate the droplet ignition process with the model in the following sections.

#### 6.4.2 *Energy transfer mechanisms*

To see the effect of the energy transfer mechanisms, we can start with analyzing the ignition of a single size droplet. The mass flow rate of the total fuel is calculated based on the air mass entrainment rate and the equivalence ratio. The fuel mass flow rate determines the amount of fuel supplied per time step. For these simulations, the ambient fluid is set to have a stoichiometric fuel-air composition. The temperature of both fuel and air are 300 K. These temperatures are chosen to simulate the engine startup environment. Cases are examined for 10 and 20  $\mu\text{m}$  droplets, as these sizes are commonly encountered in sprays. The fuel mechanism of A2 is used. A single fuel boiling temperature is used, and this temperature is chosen to be the 10% recovery temperature of A2. The transit time of the kernel through pure air is set at 20  $\mu\text{s}$ . The air entrainment rate is 30  $\mu\text{g/s}$ .

The results of the kernel temperatures as a function of time after the formation of high energy spark are shown in Figure 6.4-1. The black line indicates the temperature of the kernel if no fuel droplets are introduced. For the two cases where droplets are introduced, the amount of fuel introduced per time is the same (since the equivalence ratio is fixed). Thus the 10  $\mu\text{m}$  diameter case will have more droplets than the 20  $\mu\text{m}$  case. The simulation with 10  $\mu\text{m}$  droplets produces successful ignition, whereas the case with 20  $\mu\text{m}$  does not.

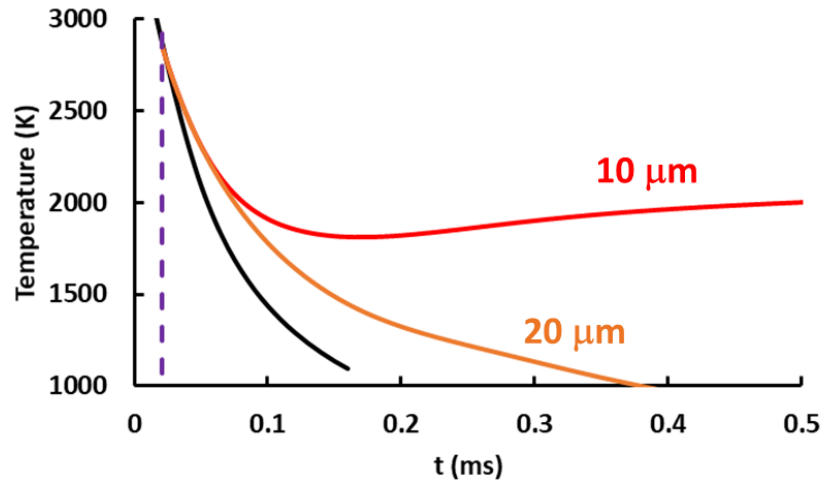


Figure 6.4-1. Temperature history for an entrained fluid mixture with an equivalence ratio of 1. The red line is for 10  $\mu\text{m}$  droplets, and the orange line is for 20  $\mu\text{m}$  droplets. The black line indicates temperature of the profile if no fuel droplets are introduced. The dashed vertical line indicates the time (20  $\mu\text{s}$ ) when fuel droplets are introduced.

To understand why the 20  $\mu\text{m}$  droplets are not able to produce a successful ignition, we can look at the primary energy transfer mechanisms that control the kernel temperature, which are the chemical heat release, the dilution cooling, and the droplet heating and vaporization. The total chemical heat release rate, the dilution cooling rate, and the droplet heating and vaporization rate for the two different droplet sizes are plotted in Figure 6.4-2, Figure 6.4-3, and Figure 6.4-4.

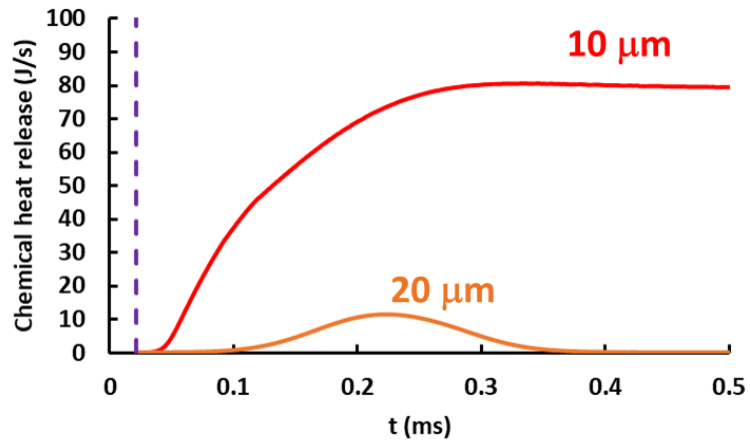


Figure 6.4-2. The chemical heat release rates for ignition of the 10  $\mu\text{m}$  droplets (red) and the 20  $\mu\text{m}$  droplets.

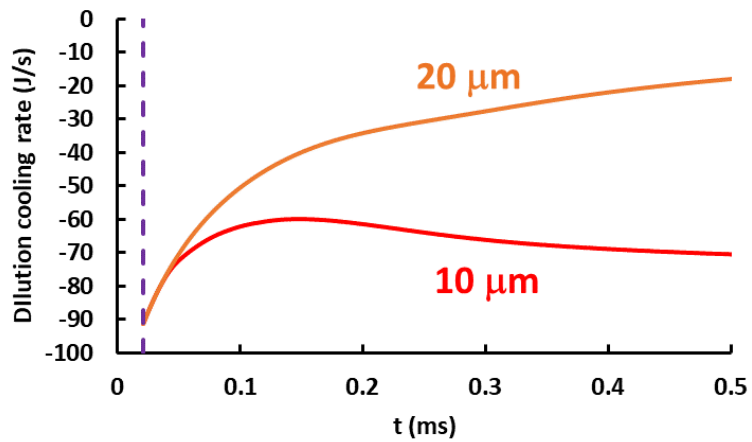


Figure 6.4-3. The dilution cooling rates for ignition of the 10  $\mu\text{m}$  droplets (red) and the 20  $\mu\text{m}$  droplets.

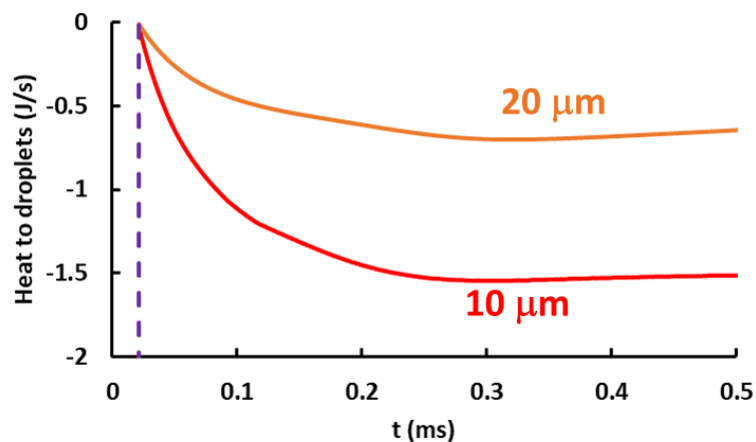


Figure 6.4-4. The energy supplied to the droplets for heating and vaporization for ignition of the 10  $\mu\text{m}$  droplets (red) and the 20  $\mu\text{m}$  droplets.

From the total chemical heat release rate (Figure 6.4-2), we see both droplet cases have heat release at early times when the kernel entrains the droplet/air mixture. For the 10  $\mu\text{m}$  case, the heat release continues, whereas the 20  $\mu\text{m}$  case produces heat only within the first 0.4 ms of the kernel development. Moreover, the total amount of heat produced in the 20  $\mu\text{m}$  case is much smaller. For both fueled cases, there is an initial delay before significant heat release is observed once the fuel is first entrained. The delay for the 10  $\mu\text{m}$  droplets is around 0.02 ms, while the delay is longer ( $\sim 0.08$  ms) for the 20  $\mu\text{m}$  droplets.

This initial delay is due to the time required for droplets to heat to a temperature close to the boiling point, when the droplets can vaporize quickly. In other words, little vapor fuel is supplied during this initial heat up time. The total vaporization rates are shown in Figure 6.4-5. The delays in the vaporization rate corresponds to the delays in chemical heat release. This indicates the delay in heat release is primarily controlled by the time required for the droplets to heat up. Thus any chemical delays (e.g., before endothermic reactions

are surpassed by exothermic reactions) are insignificant compared to the droplet heating time.

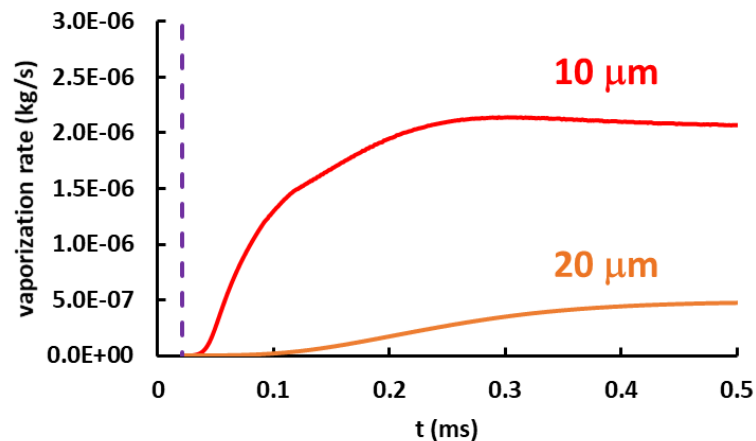


Figure 6.4-5. The total vaporization rate for ignition of the 10  $\mu\text{m}$  droplets (red) and the 20  $\mu\text{m}$  droplets.

During the droplet heat up period, when little fuel vapor is available for chemical reactions, the kernel will continue to entrain the surrounding fluids. The mixing between the hot kernel and the cold surrounding fluid leads to a drop in kernel temperature. The dilution cooling rate is shown in Figure 6.4-3.<sup>5</sup> The dilution cooling rate depends on the current kernel temperature. When the temperature of the kernel is higher, the entrained fluid needs to be heated to a higher temperature, and thus more thermal energy from the existing kernel fluid is transferred. Vice versa, if the kernel temperature is lower, less heat is required to heat the entrained fluid, and the dilution cooling rate will be lower. For the 10  $\mu\text{m}$  droplets, the dilution cooling rate decreases initially. As the chemical heat release

<sup>5</sup>The negative values of the dilution cooling rate mean the dilution cooling will decrease the temperature of the kernel.

starts raising the temperature of the kernel, the dilution cooling rate increases. For the 20  $\mu\text{m}$  droplets, the dilution cooling rate continues to decrease as the heat release rate is not able to overcome the cooling rate, and the temperature of the kernel decreases.

In addition to dilution cooling, another mechanism that can reduce the kernel temperature is transfer of thermal energy to heat and vaporize the fuel droplets. The thermal energies supplied to the droplets are shown in Figure 6.4-4. Although the amount of fuel supplied at each time step is the same, the 10  $\mu\text{m}$  droplets have a higher heat transfer rate than the 20  $\mu\text{m}$  droplets; the total surface area is higher for the larger number of smaller droplets, and a larger total surface area enhances the heat transfer rate. The heat transfer rate to the droplets also depends on the kernel temperature. With more heat release, the 10  $\mu\text{m}$  case has a hotter kernel and therefore faster droplet heating and vaporization. Comparing the magnitude of the cooling due to dilution to that associated with heat transfer to the droplets, the droplet cooling effect,  $\mathcal{O}(1 \text{ J/s})$ , is much smaller than the dilution cooling,  $\mathcal{O}(10 \text{ J/s})$ . Thus, the primary reason for any drop in kernel temperature is dilution by entrained air.

#### *6.4.3 Effect of droplet temperature and air temperatures*

In cold start and high altitude relight conditions, the temperatures of the air and the liquid fuel are lower than for regular start up conditions. The reduced order model can be used to help understand the effect of cold fuel and air on the ignition process. For this analysis, a base case is defined using most of the same conditions as in the previous section (300 K fuel and air, etc.), but now with 13  $\mu\text{m}$  droplets. Two additional cases where the fuel and air temperatures are separately set to 250 K, with the other temperature remaining

at 300 K, are used to investigate the effects of cold fuel and air. The temperatures as a function of time for the three cases are shown in Figure 6.4-6.

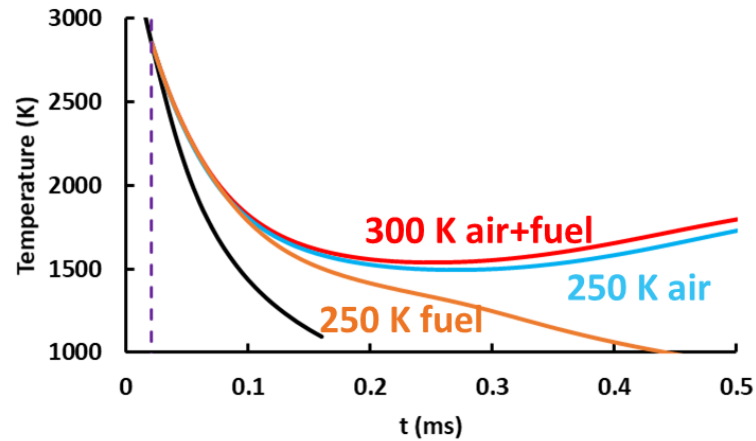


Figure 6.4-6. Kernel temperature history. The red line indicates the case where both the air and the fuel are at 300 K. The blue line indicates the case where the air temperature is set at 250 K. The orange line indicates the case where the fuel temperature is set at 250 K case.

As shown in Figure 6.4-6, both cases with 300 K fuel ignite successfully, based on the rise in the kernel temperature. For the cold fuel case, ignition is not achieved as the temperature of the kernel continues to decrease. Although the air temperature and the fuel temperature are decreased by the same amount, the change in fuel temperature has a more significant impact on the outcome of ignition. As above, additional insight is provided by examining: the chemical heat release rate, dilution cooling rate, and heat transferred to the droplets.

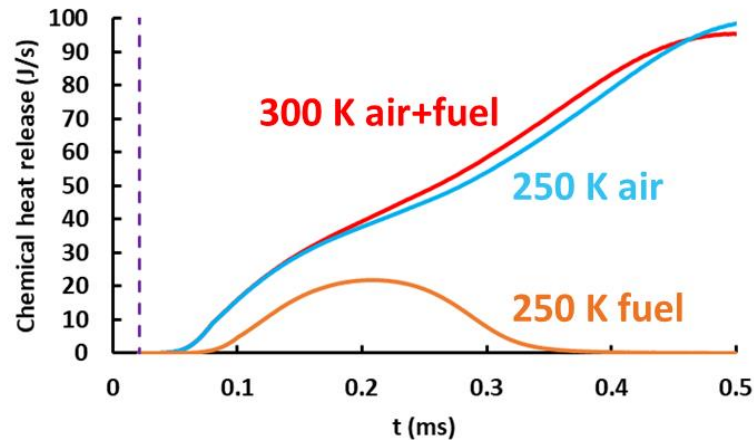


Figure 6.4-7. Total chemical heat release rate history. The red line indicates the case where both the air and the fuel are at 300 K. The blue line indicates the case where the air temperature is set at 250 K. The orange line indicates the case where the fuel temperature is set at 250 K case. The purple, dashed, vertical line indicates time when fuel droplets are introduced into the kernel.

To start, the chemical heat release rates are shown in Figure 6.4-7. The cold fuel case has a longer delay in the initial heat release compared to the base and cold air cases. As discussed previously, this chemical heat release delay is due to the time required to heat the droplet to a temperature where rapid vaporization occurs. Thus the increased time required to heat the cold fuel appears to be more important than the enhanced dilution cooling caused by reducing the air temperature. Moreover, the lower kernel temperature caused by dilution cooling will reduce the heat transfer rate to the droplets and also increase the droplet heat up time. For the cold air case, the delay in the chemical heat release rate is almost the same as that for the base case; this indicates that cooling the air by 50 K does not have a significant impact on the kernel temperature at early times.



This is verified by comparing the dilution cooling rates (Figure 6.4-8). Though the dilution cooling for the 250 K air case is faster at early times than for the 300 K air case, the difference in the dilution cooling rates are indeed small. The reason for the small difference is that the sensible enthalpy required to heat the entrained air scales as  $(T_{kernel}-T_{air})$ ; with a kernel temperature near 2000 K, a change in air temperature by 50 K is a small effect when  $T_{kernel} \gg T_{air}$ . Even if the kernel does ignite, the lower air temperature will eventually lead to a lower flame temperature, which can impact flame propagation and stability at later times.

The heat transfer rates from the kernel to the droplets are shown in Figure 6.4-9. In early times (within the first 0.1 ms), the heat transfer rate to the 250 K droplets are slightly larger than the heat transfer rates to the 300 K droplets as the temperature differences between the kernel and the droplets are larger. Although the heat transfer rate is higher for the 250 K droplets, the heat up time is still longer than those of the 300 K droplets. For the 250 K droplets, the heat transfer rate decreases in later time as the temperature of the kernel starts to drop rapidly as the kernel temperature is too low to sustain heat releasing reactions.

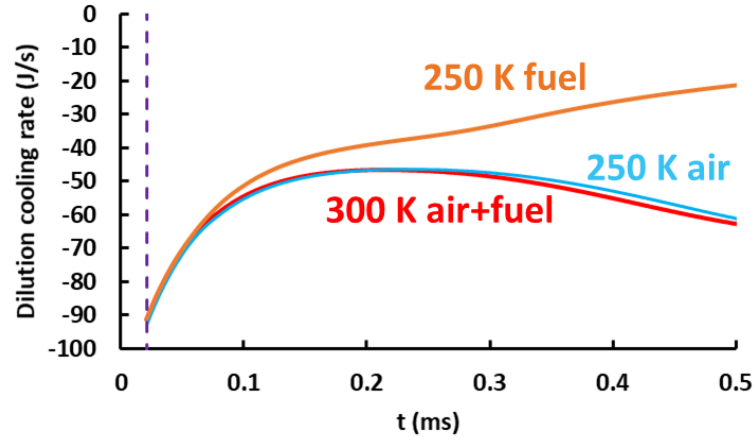


Figure 6.4-8. Kernel dilution cooling rate history. The red line indicates the case where both the air and the fuel are at 300 K. The blue line indicates the case where the case where the air temperature is set at 250 K. The orange line indicates the case where the fuel temperature is set at 250 K case.

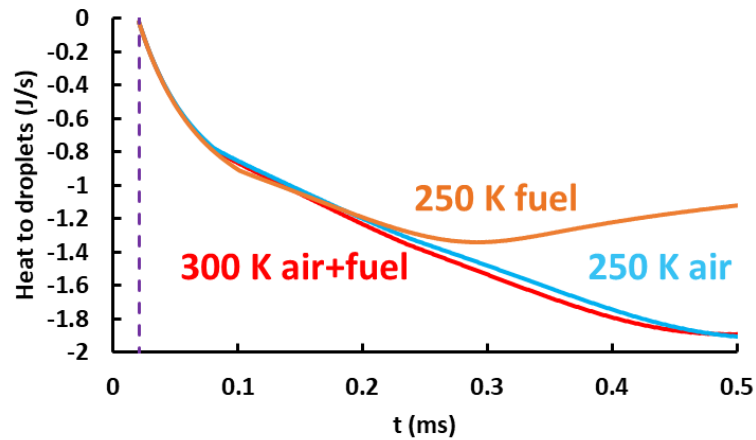


Figure 6.4-9. Temporal profile of heat transfer rate to droplets. The red line indicates the case where both the air and the fuel are at 300 K. The blue line indicates the case where the case where the air temperature is set at 250 K. The orange line indicates the case where the fuel temperature is set at 250 K case.

#### 6.4.4 Effect of droplet relative velocity (Reynolds Number)

To study the effect of Reynolds numbers on the ignition process, the droplet diameter is set at 15  $\mu\text{m}$ , and the air and fuel temperatures are 300 K. The other conditions are

consistent with those used previously. The droplet Reynolds numbers are chosen to be 0, 5, and 10. For an air viscosity at 1600 K, these Reynolds number represent droplet relative velocities at 0, 40 and 100 m/s.

The kernel temperature histories for the three relative velocity cases are shown in Figure 6.4-10. Only for  $Re_D=10$  does the kernel produce a successful ignition. Increasing  $Re_D$  and the relative velocity raises the heat transfer rate to the droplets. The impact of this is seen in the chemical heat release rate (Figure 6.4-11). The  $Re_D=0$  case has the longest time delay before chemical heat release occurs, while the  $Re_D=5$  and 10 cases have approximately the same delays. Though the delays are the same, the higher relative velocity case gives a slightly higher heat release rate; this is due to the higher vaporization rate.

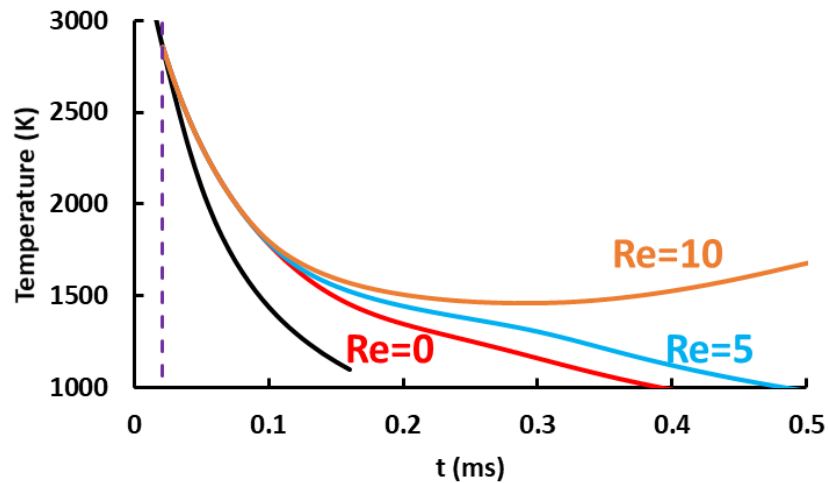


Figure 6.4-10. Kernel temperature histories. The red line indicates the case where  $Re_D=0$ . The blue line indicates the case where the case where  $Re_D=5$ . The orange line indicates the case where  $Re_D=10$ .

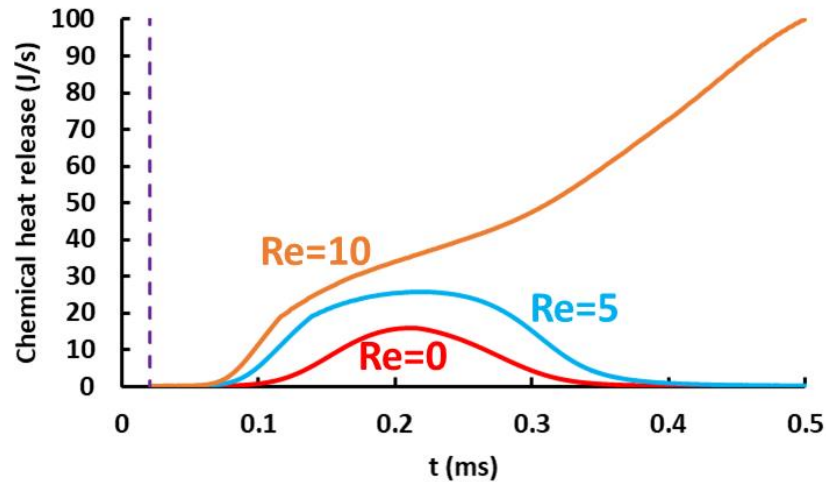


Figure 6.4-11. Chemical heat release rate histories. The red line indicates the case where  $Re_D=0$ . The blue line indicates the case where the case where  $Re_D=5$ . The orange line indicates the case where  $Re_D=10$ .

The increased heat transfer rate with Reynolds number could have a significant impact on the kernel cooling rate. This question can be answered by looking at the heat transferred to the droplets (Figure 6.4-12). Increasing  $Re_D$  indeed increases the heat transfer rate to the droplets; however, the heat transfer rate is still much smaller than the magnitudes of the chemical heat release and dilution cooling rates. Therefore, increasing relative velocity or Reynolds number will lead to earlier and faster vaporization that is beneficial to ignition, but doing so will not significantly increase the kernel cooling rate.

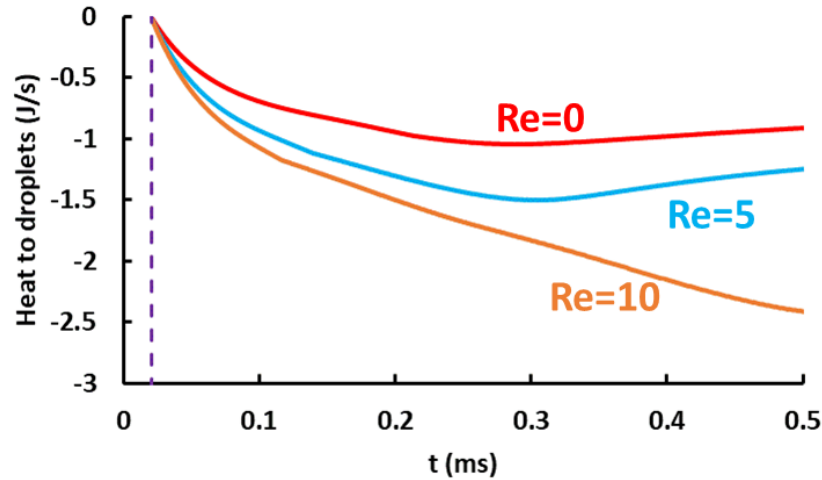


Figure 6.4-12. Temporal evolution of heat transfer rates to the droplets. The red line indicates the case where  $Re_D=0$ . The blue line indicates the case where the case where the  $Re_D=5$ . The orange line indicates the case where  $Re_D=10$ .

#### 6.4.5 Effect of fuel chemistry and recovery temperatures on ignition

In the previous simulations, the recovery temperature of the fuel is set at a constant value of 433 K, the 10% recovery temperature for A2. The fuels are composed of many different components, and the conditions required to produce rapid fuel vaporization are not completely described by a single temperature. From the analysis in §6.3.2, the ignition probabilities were seen to correlate well to the heating times when either 10% or 20% recovery temperature were chosen. In §6.4.3, varying the droplet's initial temperature proved to have a strong effect on ignition by increasing the droplet heating time. The variation of the recovery temperature should also introduce variation in the heating time. The goal of this section is to investigate the effect of the fuel chemistry, the recovery temperature, and the initial droplet temperature on the minimum or critical droplet size for

ignition to occur. The recovery temperature and the initial droplet temperature will both affect heating times, which are shown to be important in previous sections. The relative effects of fuel chemistry, viscosity, recovery temperature, and initial fuel temperature are investigated.

The relative effects are studied using two fuel chemistries, three recovery temperatures, and two initial droplet temperatures. The droplet sizes are varied such that successful and unsuccessful ignition cases are achieved. A larger critical droplet size for a given set of fuel and flow conditions indicates easier ignition. The fuel chemistries for A2 and C1 are chosen as they showed large differences in the prevaporized study (Chapter 5). The initial fuel temperatures are varied so that the heating times are longer. Longer heating time means lower kernel temperature, and the fuel chemistry effect may be more significant. The equivalence ratios are set at 1. Three boiling temperatures are chosen from the range of the 10% recovery temperature to the 40% recovery temperatures of all fuels. The parameter matrix is shown in Table 6. A total of 16 cases are studied. The results of the minimum droplet sizes for ignition of the 300 K fuel is presented in Figure 6.4-13. From this figure, we can see the relative influence of the boiling temperatures and the fuel types on ignition. The variation in droplet size caused by different fuel boiling temperature is indicated by the red vertical double-sided arrow. The results of fuel A2 is represented by a green line and green points, and that of C1 is represented by a yellow line and yellow points. Different fuel mechanisms do influence the maximum droplet size. At each boiling temperature, C1 requires smaller droplets than A2 does. This means C1 is harder to ignite than A2. Previous study on C1 fuel mechanism shows high concentration of isobutene as an intermediate product of fuel breakdown. Isobutene's reaction rate is sensitive to the temperature

variation, and its rate is slower than other intermediate products as the temperature decreases. Thus, C1 should be harder to ignite than A2. However, the change in the boiling temperature by 60 K will introduce a much larger effect on the maximum droplet size for ignition. The blue dashed vertical line indicates the range of droplet sizes due to the variation in viscosities. Therefore, viscosity will have a more dominant effect than boiling temperature or fuel type.

Table 6. Parametric study to characterize the effect of the fuel type and the boiling temperatures on ignition.

<b>Fuel Chemistry</b>	<b>Boiling Temperature</b>	<b>Fuel Initial Temperature</b>	<b>Dynamic Viscosity</b>
<b>A2</b>	433 K	300 K	1.0 cSt
<b>C1</b>	453 K	220 K	3.0 cSt
	493 K		5.0 cSt

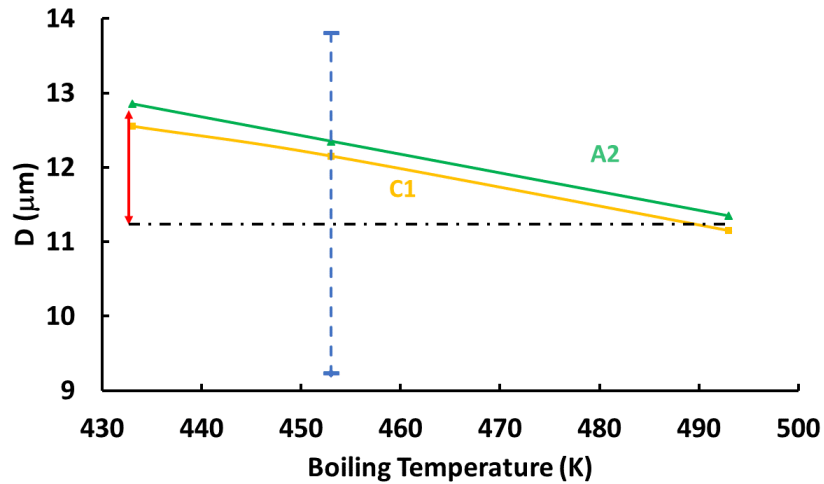


Figure 6.4-13. Dependence of critical droplet size on boiling temperatures representing the range of the 10%-40% recovery temperatures. The blue dashed vertical line indicates the variation in droplet sizes due to the differences in viscosity for the droplet size at the boiling temperature of 493 K.

For the fuel temperature starting at 220 K, the maximum droplet size of ignition is also obtained. The results compared to the 300 K fuel is presented in Figure 6.4-14. As the fuel temperature is decreased, smaller droplets are required to achieve ignition. The effect of boiling temperatures on the maximum droplet size decreases as the temperature differences increase between the boiling temperature and the initial droplet temperature.



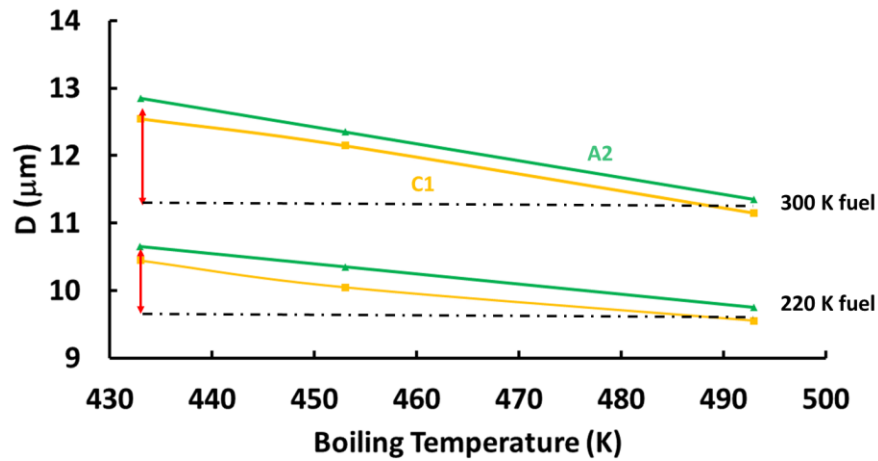


Figure 6.4-14. The maximum droplet sizes in between the successful/unsuccessful ignition cases versus the boiling temperatures representing the range of the 10%-40% recovery temperatures. The initial fuel temperatures are at 220 K and 300 K. The blue dashed vertical line indicates the variation in droplet sizes due to the differences in viscosity for the droplet size at the boiling temperature of 493 K.

#### 6.4.6 Effect of droplet distribution

For single size droplets, all droplets entering the kernel will have the same history in terms of heating and vaporization. If the droplets entering have a distribution of sizes, the Rosin-Rammler droplet size distribution ( $Q$ ) described in Equation 16 is commonly used to describe the volumetric distribution of droplets. For  $X=20 \mu\text{m}$ , the results of  $dQ/dD$  for  $q=3$ ,  $q=5$ , and  $q=10$  as a function of  $D$  are shown in Figure 6.4-15. As the value of  $q$  increases, the distribution becomes narrow, with the fuel mass stored in droplets with diameters near  $X$ . For smaller  $q$ , more masses are stored in the smaller droplets and the larger droplets. The effect of these three distributions on the ignition is tested at 300 K fuel and air temperature. The equivalence ratio is 1 with 30 mg/s entrainment rate. The fuel

boiling temperature is set at 433 K. The results or the kernel temperatures are shown in Figure 6.4-16.

For the three cases, only  $q=3$  produces a successful ignition. This shows that having more mass in the smaller droplet sizes benefits ignition. This agrees with the monodisperse droplet simulations in the previous sections; the smaller droplets begin to vaporize earlier, allowing heat release to start before the kernel temperature drops too much. This is verified by the chemical heat release rates shown in Figure 6.4-17, and the fuel vaporization rates shown in Figure 6.4-18.

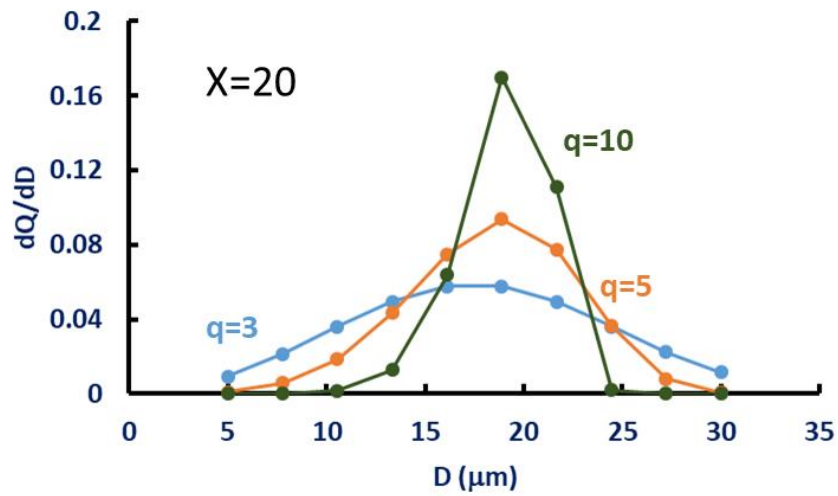


Figure 6.4-15.  $dQ/dD$  derived from the Rosin-Rammler distribution (Equation 17) for  $X=20$  and  $q=3$  (blue), 5 (orange), and 10 (green).

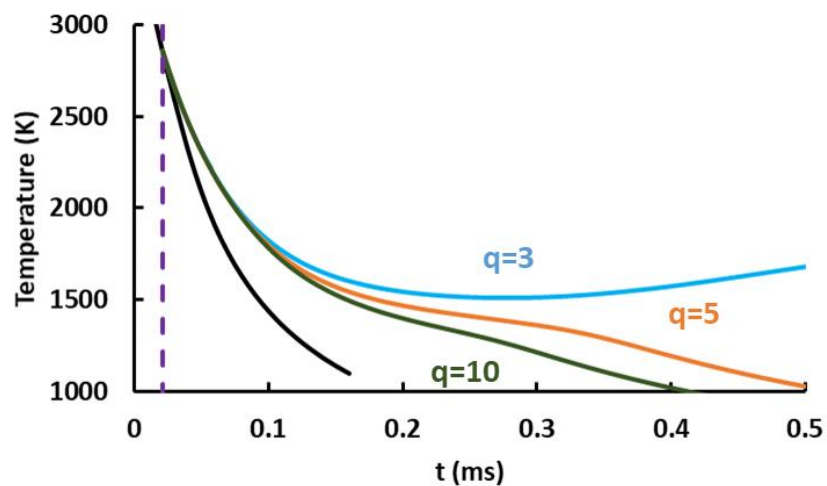


Figure 6.4-16. The temperature profiles as a function of time since the spark is introduced for three droplet size distribution based on the Rosin-Rammler distribution.

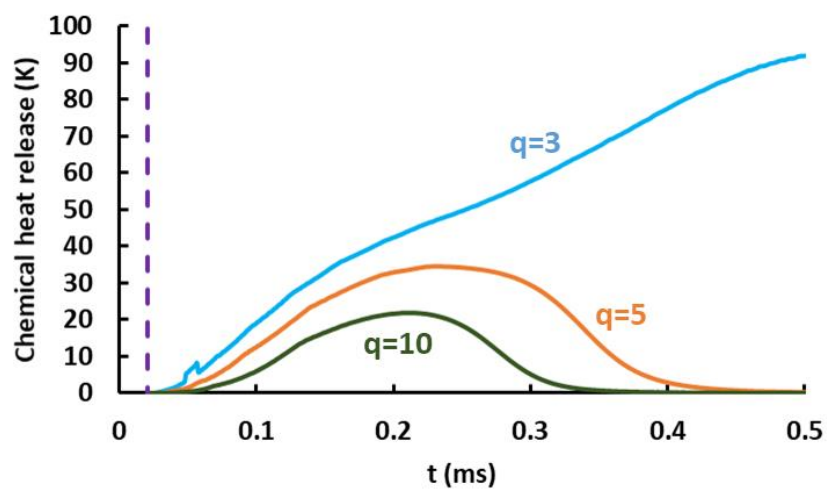


Figure 6.4-17. The chemical heat release rates as a function of time since the spark is introduced for three droplet size distribution based on the Rosin-Rammler distribution.

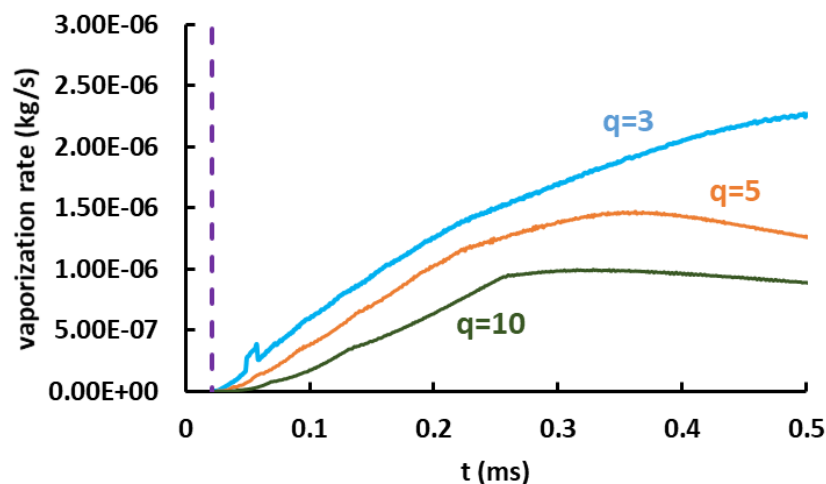


Figure 6.4-18. The liquid fuel vaporization rates as a function of time since the spark is introduced for three droplet size distribution based on the Rosin-Rammler distribution.

## 6.5 Chapter summary

The ignition probabilities for a large number of fuels were acquired at the same global equivalence ratio, and for room temperature and chilled fuel conditions. The relative ignitability of the fuels shows significant differences from the prevaporized results of Chapter 5. This result indicates factors other than the fuel chemistry will affect ignition of the liquid fuel spray. The ignition probabilities of the liquid fuel sprays show good correlations to the viscosity and the recovery temperature and bad correlations to the derived cetane numbers and the densities. Good correlation of the ignition probabilities to the predicted droplet sizes is observed, and the viscosities have strong effect on the droplet sizes. The ignition probabilities correlate well to the heating times as well, calculated based on the droplet sizes. The LLO model is also correlated to the ignition probability. The variation in the effective vaporization constant is small, and the effective vaporization constant don't show good correlation to the ignition probabilities. The good correlation

between the LLO and the probabilities is mainly due to the strong influence of the droplet sizes.

Through the droplet ignition modeling, three energy transfer mechanisms are identified, and they are chemical heat release, dilution cooling, and heat transferred to the droplets. The droplet heating time is shown to have a strong effect on the ignition outcome. If the heating time is too long, the kernel will be diluted to a lower temperature through entrainment, thus making the chemical heat release and ignition harder. Cooling the fuel have a much stronger effect than cooling the air. From the minimum droplet size required for ignition, cooling the fuel have stronger influence on the droplet sizes than the fuel recovery temperatures, and the fuel recovery temperature have a stronger influence than the fuel chemistry. The changes in fuel viscosity have the strongest influence on the droplet sizes. Lastly, having more droplets distributed in the small droplet class is beneficial for ignition as the smaller droplets will lead to heat release more quickly.

The droplet size and velocity distribution are measured with PDPA at certain locations. The PDPA measurements can be used for future CFD modeling. The PDPA measurement also confirms that using Equation 10 to predict the Sauter Mean Diameter (SMD) is a valid approximation.

## **CHAPTER 7:**

### **CONCLUSIONS AND RECOMMENDATIONS**

#### **7.1 Summary and conclusions**

The introduction of alternative jet fuels from sources different than the conventional petroleum distillates creates uncertainties in the required properties to provide robust ignition performance in existing jet engines. This thesis explores the effect of jet fuel composition on forced ignition in conditions relevant to the early evolution of the spark kernel in liquid-fueled turbine engines. This research is the first study on the detailed measurement and modeling of the ignition process with liquid fuel sprays.

To characterize the effect of fuel composition on forced ignition, ignition probabilities of 14 fuels were acquired in a well-controlled, easy-to-model rig using a conventional aircraft engine, sunken-fire igniter. The fuels included standard distillates (Jet-A, JP-5, and JP-8), ten non-distillates, and n-dodecane. Ignition probabilities were measured for prevaporized fuels and fuel sprays. In addition to the ignition probabilities, high speed diagnostics, specifically simultaneous, emission, schlieren and OH PLIF imaging were applied to study the kernel development for the prevaporized fuels. Spray ignition data were obtained at two fuel temperatures (300 and 247 K) for a fixed air temperature of 300 K. Droplet size distributions and velocities were measured at multiple locations upstream of the region where the kernel interacts with the spray for five fuels. A reduced-order model was also developed that incorporates kernel entrainment, fuel chemistry, droplet heating and vaporization, all the processes expected to be important in ignition.

### 7.1.1 Paradigm for forced ignition

Previous work for gaseous fuels had established a paradigm of the forced ignition process, wherein the ejected spark kernel entrains surrounding fluids, initially composed primarily of air. Ignition success was found to be a competition between the chemical heat release and the dilution cooling. The high speed imaging of the kernel development for the prevaporized liquid fuels confirmed the entrainment structure, and showed that successful ignition depends on the chemical reactions occurring at very early times in the regions where fuel is entrained into the hot kernel. The early development the ejected spark kernel is not like the spherically expanding kernel typically described for conventional SI engine forced ignition.

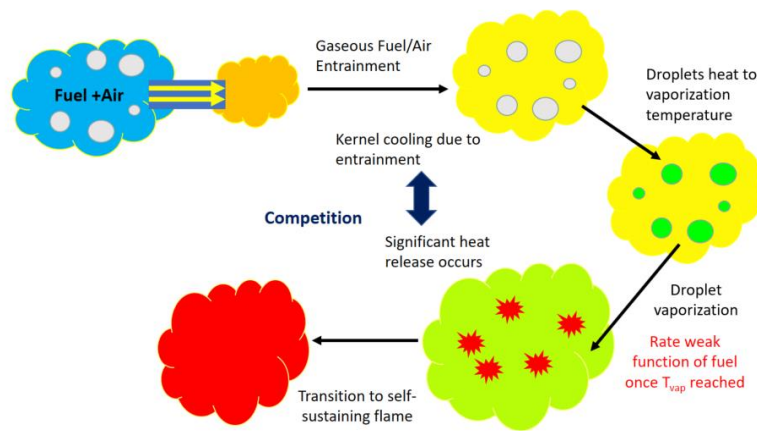


Figure 7.1-1. Schematic of the proposed paradigm for forced ignition of liquid fuel/air mixture in gas turbine combustors

This thesis has extended this understanding for forced ignition of liquid fuel sprays. The schematic for the paradigm of spray ignition is shown in Figure 7.1-1. At typical startup or relight conditions, there is little or no prevaporization of the fuel. Thus successful

ignition requires that the droplets entrained by the kernel need to be heated to a temperature where rapid vaporization can occur (and thus heat can be released by chemical reactions) before the kernel temperature drops too low due to entrainment of cold air. Through reduced order modeling, cooling due to entrainment greatly outweighs the heat transfer required to heat and vaporize the droplets.

#### *7.1.2 Droplet heating*

The major factors that influence the droplet heating process are the droplet size, fuel vaporization temperature(s), initial fuel temperature, kernel temperature. For successful ignition, the reduced order modeling revealed that the most sensitive parameters (for a fixed kernel temperature) are, in decreasing order, droplet size, initial fuel temperature, and vaporization temperature. This agreed with the experimental results, which showed a strong correlation between ignition probability and droplet size. Given the large difference between kernel and air temperature, the latter generally has a smaller effect. Similarly, variations in fuel chemistry were also found to be small. As an example, at conditions similar to the experiments, it was found that the changing the vaporization temperature from 433 to 493 K only changed the critical droplet size for ignition by  $\sim 2 \mu\text{m}$  (i.e., 13 to 11  $\mu\text{m}$ ). Whereas the fuel chemistry difference between two fuels with noticeably different chemical rates (A2 and C1) only had an equivalent size effect of  $\sim 0.1 \mu\text{m}$ .

Depending on the type of fuel atomizers, the fuel properties that most influence droplet size are the viscosity, the surface tension, and the density. The fuel temperature can influence both the droplet sizes (e.g., through the viscosity) and the amount of heat required to raise the droplet temperature to a point where vaporization is rapid.



Having an atomization that produces mostly very small droplets may seem beneficial to ignition. However, only droplets that can interact with the spark kernel at early times will influence the ignition outcome. In turbine engines, where swirling flows are present, droplets that are too small may not be able to reach a region close to the igniter. Thus there is likely to be an optimum droplet size range for successful ignition.

### 7.1.3 *Fuel chemistry*

The prevaporized studies were used to separate the effect of fuel chemistry from the physical effect of droplet vaporization. Traditional fuel characteristics such as DCN did not show a strong correlation to the experimentally measured ignition probabilities. An analysis of the intermediate species produced in the parent fuel breakdown process as predicted by the HyChem model revealed a strong correlation between ignitability and the relative production of species like ethylene, which was shown to have the most rapid autoignition behavior of all the stable fuel intermediates. Some fuels, such as C1, showed a more sensitive dependence on the kernel temperature due to the high amount of isobutene produced by that fuel. The autoignition delay for isobutene is close to that of ethylene at high temperatures (e.g., 1800 K), but is quite slow at lower temperatures (e.g., 1400 K). Of the five fuels for which HyChem mechanisms were available, the predicted ignitability rankings agreed reasonably well with the experiments, except for C5. This suggests that the C5 mechanism is inaccurate.

## 7.2 Recommendation for future work

Despite the findings on the fuel effect forced ignition already obtained in this thesis, there are many more questions yet to be answered. First, it will be beneficial to use high speed diagnostics to record the development of a spark kernel in a fuel spray. From the images, we may be able to find the fuel vaporization rate (fuel PLIF) and the trajectory of the droplets so we can confirm whether the droplets will stay in the kernel or will they have the momentum to pass through the spark kernel.

For ignition of prevaporized jet fuel, although the importance of the intermediate fuel species is identified, the autoignition study that determines the chemical reactivity of the intermediates is conducted in neat air. In actual ignition, these fuel species are likely to have influence on each other as their reaction pathway can be interdependent. More study is required to understand the effect of these intermediates when interacting with each other. Also, as mentioned previously, the C5 fuel mechanism at high temperature will need further study.

For ignition in fuel spray, the fuel C9 will required further investigation as its ignition behavior deviates from the trends of good correlations significantly. More testing should be performed on C9. The droplet ignition model can have great potential in engineering practices, such as investigating the effect of low air pressure on fuel chemistry and vaporization. Treating the vapor as a single fuel species can be problematic, as the fuel vaporizing at different fuel temperature can be very different. A better model will account for the different recovery temperatures and the vaporizing species at different temperatures. The rig used in this research has a low turbulence level in the crossflow. In actual

combustors, the flow can be highly turbulent. High turbulence can affect the spark kernel in early time by increasing the dilution cooling rate. In later time, high turbulence can severely stretch a self-sustaining flame and cause the flame to extinguish. Therefore, the forced ignition of an ejected spark kernel in turbulent flow requires more study.

## APPENDIX A. ADDITIONAL FUEL PROPERTIES

Fuel	T10 (K)	T20 (K)	T50 (K)	dynamic viscosity @ 293 K (m <sup>2</sup> /s)	surface tension(n/ m) @293 K	fuel density/kg/ m <sup>3</sup> )	%iso	%n	%aro	%cyclo	DCN
A1	437.15	444.15	462.15	1.5E-06	2.35E-02	792	26.82	36.69	13.41	20.08	47.9
A2	449.15	457.15	478.15	1.77E-06	2.6E-02	803	20.03	29.45	18.66	31.86	47
A3	465.15	472.15	491.15	0.000002	2.61E-02	827	13.89	18.14	20.59	47.37	40.4
C1	451.15	452.15	455.15	1.53E-06	2.3E-02	760	0.01	99.62	0.01	0.05	17.1
C2	463.15	471.15	497.15	1.91E-06	2.52E-02	782	5.16	77.51	17.05	0.07	50.4
C3	477.15	485.15	503.15	2.56E-06	2.61E-02	793	9.17	45.19	13.6	31.72	47
C4	442.15	443.15	452.15	1.63E-06	2.27E-02	747	0.23	98.94	0.39	0.43	28
C5	434.15	435.15	435.15	1.02E-06	2.4E-02	769	17.66	51.58	30.68	0.07	39.6
C7	468.15	478.15	490.15	2.11E-06	2.6E-02	817	N/A	N/A	N/A	N/A	42.6
C8	458.15	462.15	483.15	1.76E-06	2.6E-02	823	N/A	N/A	N/A	N/A	43.5
C9	458.15	468.15	490.15	2.12E-06	2.6E-02	759	N/A	N/A	N/A	N/A	63.3
ndodecane	484.85	485.15	485.45	1.44E-06	2.50E-02	750	N/A	N/A	N/A	N/A	75.02
S1	412.15	430.15	467.15	1.2E-06	2.6E-02	768	57.9	17.6	22.4	0.1	50
S2	394.15	404.15	407.15	1.3E-06	2.6E-02	777	50.9	26.6	22.4	0.1	50.6

## APPENDIX B. IMAGING PROCESSING CODE (MATLAB)

### Edging tracking of Schlieren Images:

```
clear all
SchlierenvidReader = VideoReader('C5_fail.avi');
nFrame = SchlierenvidReader.Duration*SchlierenvidReader.FrameRate;
Schlierenvid = zeros(SchlierenvidReader.Height,
SchlierenvidReader.Width, nFrame);
framerate = 10000;
delay = 33e-6;
n = 1;
while hasFrame(SchlierenvidReader)
    Schlierenvid(:, :, n) = readFrame(SchlierenvidReader);
    n = n + 1;
end

background = Schlierenvid(:, :, 1);

SchlierenvidNoBG = zeros(SchlierenvidReader.Height,
SchlierenvidReader.Width, nFrame);
%background subtraction
for i = 1:nFrame
    SchlierenvidNoBG(:, :, i) = Schlierenvid(:, :, i) - background;
    medfilt2(SchlierenvidNoBG(:, :, i));
end

%%obtain data
%generate processed videos

%tracking the edge of the boundary

time = zeros(nFrame, 1);
area = zeros(nFrame, 1);
ymin = zeros(nFrame, 1);

ignitorpos = 683;

for i = 1:nFrame
    SchlierenvidNoBG(:, :, i) =
medfilt2(SchlierenvidNoBG(:, :, i) ./ 255); %imshow can only show
between 0 and 1;
    bwSchlieren = medfilt2(im2bw(SchlierenvidNoBG(:, :, i), 0.1));

    [B, L] = bwboundaries(bwSchlieren, 'noholes', 4);
    s = regionprops(bwSchlieren, 'Area');
    area(i) = sum(cat(1, s.Area));
```

```

    extma = regionprops(bwSchlieren, 'Extrema');
    yval = [];

    for index = 1:length(extma)
        yval = [yval, extma(index).Extrema(:,2)];
    end
    if isempty(yval) == 1
        ymin(i) = 0;
    else
        ymin(i) = abs(ignitorpos - min(min(yval)));
    end

    %     imshow(Schlierenvid(:,:,i)./255);
    %     hold on;
    %     for k = 1:length(B)
    %         boundary = B{k};
    %         plot(boundary(:,2), boundary(:,1), 'w', 'LineWidth', 2,
    % 'Color', 'g')
    %     end
    %     pause(0.01);
    %
    %     frame = getframe;
    %     writeVideo(VidWriter, frame);

    time(i) = (i-1)*1/framerate + delay;
end
% close(VidWriter);

header = {'time', 'pixels', 'abs pos from ignitor'};
xlswrite('C5_fail.xlsx', header, 'Schlieren', 'A1');
xlswrite('C5_fail.xlsx', time, 'Schlieren', 'A2');
xlswrite('C5_fail.xlsx', area, 'Schlieren', 'B2');
xlswrite('C5_fail.xlsx', ymin, 'Schlieren', 'C2');

plot(time, area)
plot(time, ymin)

```

### **Image De-warping based on registered coordinates:**

```

SCHcali = histeq(imread('SCHcali.tif'));
PLIFcali = histeq(imread('PLIFcali.tif'));
CHEMcali = histeq(imread('CHEMcali.tif'));

schcrop = xlsread('crop.xlsx', 'sch');
chemcrop = xlsread('crop.xlsx', 'chem');
plifcrop = xlsread('crop.xlsx', 'plif');

chemcalicrop = cropthis(CHEMcali, chemcrop);
schcalicrop = cropthis(SCHcali, schcrop);

```

```

plifcalicrop = cropthis(PLIFcali, plifcrop);

movingPoints_c2s = xlsread('regpoints.xlsx', 'chemmove');
fixedPoints_c2s = xlsread('regpoints.xlsx', 'chemfix');
movingPoints_p2s = xlsread('regpoints.xlsx', 'plifmove');
fixedPoints_p2s = xlsread('regpoints.xlsx', 'plifix');

tform_p2s = fitgeotrans(movingPoints_p2s, fixedPoints_p2s,
    'affine');
Cali_PLIF_Registered =
imwarp(plifcalicrop,tform_p2s,'OutputView',imref2d(size(schcalicrop)
));

tform_p2s = fitgeotrans(movingPoints_c2s, fixedPoints_c2s,
    'affine');
Cali_Chem_Registered =
imwarp(chemcalicrop,tform_p2s,'OutputView',imref2d(size(schcalicrop)
));

```

### **Gray Scale Inversion with OpenCV:**

```

import cv2
import numpy as np
from matplotlib import pyplot as plt
import os

print("processing program running...")

fnames = os.listdir(os.getcwd())
snum = 1;
pnum = 1;
cnum = 1;
for fname in fnames:
    if fname.find('sprocess_newreg') != -1:
        imgname = 'sprocess'
        filename = fname
        img = cv2.imread(filename ,0)
        scale = float(255)/float(img.max());
        img = cv2.multiply(img, 2)
        img = cv2.medianBlur(img, 7)
        bright_mask = 255*np.ones(img.shape)
        bright_pop = bright_mask - img;
        #plt.imshow(bright_pop, cmap = 'gray')
        #plt.show();
        savefilename = imgname + '_invert' + str(snum) + '.tif';
        cv2.imwrite(savefilename, bright_pop);
        snum += 1;

    if fname.find('pprocess_newreg') != -1:
        imgname = 'pprocess'

```

```

filename = fname
img = cv2.imread(filename ,0)
scale = float(255)/float(img.max());
img = cv2.multiply(img, 3)
bright_mask = 255*np.ones(img.shape)
bright_pop = bright_mask - img;
#plt.imshow(bright_pop, cmap = 'gray')
#plt.show();
savefilename = imgname + '_invert' + str(pnum) + '.tif';
cv2.imwrite(savefilename, bright_pop);
pnum += 1;

if fname.find('cprocess_newreg') != -1:
    imgname = 'cprocess'
    filename = fname
    img = cv2.imread(filename ,0)
    scale = float(255)/float(img.max());
    bright_mask = 255*np.ones(img.shape)
    bright_pop = bright_mask - img;
    #plt.imshow(bright_pop, cmap = 'gray')
    #plt.show();
    savefilename = imgname + '_invert' + str(cnum) + '.tif';
    cv2.imwrite(savefilename, bright_pop);
    cnum += 1;

print{"check folder, done, bye bye"}i

```



## APPENDIX C. PSR TWO-STAGE IGNITION CODE (PYTHON)

### First stage with the air plasma mechanism:

```
import cantera as ct
import numpy as np
import matplotlib.pyplot as plt

def plasmareactor(dt, endtime, mentrain, Tin, Pin, Xin):
    E_spark = 1.25; #energy from spark
    V_spark = 10e-3*(np.pi/4)*(5e-3**2); #initial volume of the
    spark(or reactor)

    #-----import solution in cantera-----#
    gas = ct.Solution('SforzoairNASA9.xml');
    gas.TPX = Tin, ct.one_atm, Xin;
    NSpecies = gas.n_species; #number of species
    m_init = gas.density*V_spark; #initial mass
    gas.X = Xin;
    e_spark = E_spark/m_init + gas.int_energy_mass;
    gas.UVX = e_spark, 1/gas.density, Xin;
    gas.TP = gas.T, ct.one_atm
    gas.equilibrate('SP');
    print(gas.T)

    #-----create the reactor network-----#
    kernel = ct.IdealGasReactor(gas);
    kernel.volume = 1.9e-8;#determined by Schlieren, m3
    air = ct.Solution('SforzoairNASA9.xml');
    air.TPX = Tin, Pin, Xin;
    env = ct.Reservoir(air);
    w = ct.Wall(kernel,env);
    w.area = 1.0;
    w.expansion_rate_coeff = 1.0e6;
    mfc = ct.MassFlowController(env, kernel);#mass flow controller
    mfc.set_mass_flow_rate(mentrain);
    net = ct.ReactorNet({kernel});
    filename = 'plasma_'+ str(np.int(endtime*1e6))+
    '_microsec_477K.csv'
    print(filename)
    f = open(filename, 'w+')
    snames = '';
    for i in np.linspace(0,NSpecies-1,NSpecies):
        snames = snames + ',' + gas.species_name(i)
    f.write('time,temperature,pressure,volume' + snames + '\n')

    #-----container for data storage-----#
    for i in np.linspace(1, np.int(endtime/dt),np.int(endtime/dt)):
        net.advance(i*dt);
```

```

        if i%10 == 0:
            molefrac = '';
            print('running')
            for j in np.linspace(0,NSpecies-1,NSpecies):
                molefrac = molefrac + ',' + str(gas.X[int(j)]);
            f.write(str(net.time)+ ',' + str(kernel.T) + ',' + \
                    + str(gas.P) + ',' + str(kernel.volume) + \
                    molefrac+ '\n');
    f.close();
    return
plasmareactor(1e-8, 250e-6, 6e-5, 477, ct.one_atm, 'O2:21, N2:79')

```

### **Second stage with the hybrid chemistry (HyChem) mechanisms:**

```

import cantera as ct
import numpy as np
import sys

def fuelreactor(dt, endtime, mentrain, A2Conc, EQ, properties, Tin,
Pin, folder):
    #-----define fuel properties required later-----
    -----#
    MW_A2 = 158.6;
    MW_C1 = 178;
    rho_A2 = 837.5;
    rho_C1 = 761.0;

    gas = ct.Solution('a2c1blend.cti');

    #-----conversion of species from plasma to fuelX mech-
    -----#
    N2 = properties[3] + 0.5*properties[5] + 0.5*properties[6];
    O2 = properties[4] + 0.5*properties[5];
    O = properties[7];
    plasma_comp = 'N2:' + str(N2) + ',O2:' + str(O2) + ',O:' +
str(O);
    gas.X = plasma_comp;
    NSpecies = gas.n_species;
    gas.TPX = properties[0], properties[1], plasma_comp;

    #-----set environment gas based on the mixture ratio and
    equivalence ratio-----#
    envgas = ct.Solution('a2c1blend.cti');
    A2C = gas.n_atoms('POSF10325', 'C');
    A2H = gas.n_atoms('POSF10325', 'H');
    C1C = gas.n_atoms('POSF11498', 'C');
    C1H = gas.n_atoms('POSF11498', 'H');
    if A2Conc == 0:
        nC1 = 1;
        stoich_coeff = nC1*C1C + 0.25*nC1*C1H;

```

```

        nO2 = stoich_coeff*1;
        nN2 = stoich_coeff*3.76;
        env_comp = 'POSF11498:' + str(EQ*nC1) + ',O2:' + str(nO2) +
        ',N2:' + str(nN2);

    else:
        moleA2 = A2Conc*rho_A2/MW_A2;
        moleC1 = (100 - A2Conc)*rho_C1/MW_C1;
        nA2 = 1
        nC1 = nA2*moleC1/moleA2;
        stoich_coeff = (nA2*A2C + nC1*C1C) + 0.25*(nA2*A2H +
nC1*C1H);
        nO2 = stoich_coeff*1;
        nN2 = stoich_coeff*3.76;
        nA2 = EQ*nA2;
        nC1 = EQ*nC1;
        env_comp = 'POSF10325:' + str(nA2) + ',POSF11498:' +
str(nC1) + ',O2:' + str(nO2) + ',N2:' + str(nN2);

    print(stoich_coeff)
    print(env_comp)
    envgas.TPX = Tin, Pin, env_comp

    envgas_temp = ct.Solution('a2c1blend.cti')
    envgas_temp.TPX = Tin, Pin, env_comp

    #-----set the reactor and reactor network-----#
    kernel = ct.IdealGasReactor(gas);
    kernel.volume = properties[2];
    env = ct.Reservoir(envgas);
    w = ct.Wall(kernel, env);
    w.area = 1.0;
    w.expansion_rate_coeff = 1.0e5; # this expansion rate can
significantly affect the convergence rate
    mfc = ct.MassFlowController(env, kernel);#mass flow controller
    mfc.set_mass_flow_rate(mentrain);
    net = ct.ReactorNet({kernel});

    #set up file director for saving files
    filename = folder + '/'+'A2Conc_' + str(A2Conc) + '_EQ_' +
str(EQ) + '_envtemp_' + str(Tin) + '.csv';
    filename_kinetic = folder + '/'+'A2Conc_' + str(A2Conc) + '_EQ_'
+ str(EQ) + '_envtemp_' + str(Tin) + '_kinetic.csv'
    print(filename)
    print(filename_kinetic)
    f = open(filename, 'w+')
    f2 = open(filename_kinetic, 'w+')
    snames = ''; #name of the species
    enames = ''; #name of the reaction equations
    for i in np.linspace(0,NSpecies-1,NSpecies):
        snames = snames + gas.species_name(i);
        f.write('time,temperature,pressure,volume,heat
release,dilution,' + snames + '\n');

```

```

for i in range(0,14):
    enames = enames + ',' + gas.reaction_equation(i);

f2.write(enames + '\n');

print(gas.T)

for i in np.linspace(1, np.int(endtime/dt), np.int(endtime/dt)):
    net.advance(i*dt);

    molefrac = '';
    frate = '';
    heat_release = -np.dot(gas.net_rates_of_progress,
gas.delta_enthalpy)*kernel.volume
    envgas_temp.TP = gas.T, ct.one_atm
    dilution = mentrain*(envgas.h-envgas_temp.h)
    for j in np.linspace(0,NSpecies-1,NSpecies):
        molefrac = molefrac + ',' + str(gas.X[int(j)])
    f.write(str(net.time)+ ',' + str(kernel.T) + ',' + '\
        + str(gas.P) + ',' + str(kernel.volume) + ',' + '\
        +str(heat_release) + ',' + str(dilution) + ',' + '\
        + molefrac+ '\n');
    for j in range(0,14):
        frate = frate + ',' +
str(gas.forward_rate_constants[int(j)]);
    f2.write(frate + '\n');

    print(str(int(endtime/dt)-i) + ' iterations left');

f.close();
f2.close();
return

```

### Example execution code (the main file):

```

#iterate different cases in main.py
import csv
import cantera as ct
import fuelair as fa
import os
ct.suppress_thermo_warnings()

#-----read in data and fill in data for the nitrogen
and oxygen species----#
f = open('plasma_90_microsec_477K.csv', 'r+');
spamreader = csv.reader(f, delimiter=',');
for row in spamreader:

```

```

    if spamreader.line_num == 901:
        plasma_temp = float(row[1]);
        plasma_pressure = float(row[2]);
        plasma_volume = float(row[3]);
        #-----capture the mole fractions-----#
        plasma_N2 = float(row[4]);
        plasma_O2 = float(row[5]);
        plasma_NO = float(row[6]);
        plasma_N = float(row[7]);
        plasma_O = float(row[8]);
f.close();
print(plasma_temp)
properties = [plasma_temp, plasma_pressure, plasma_volume,
plasma_N2\
              , plasma_O2, plasma_NO, plasma_N, plasma_O]

#-----check for file directory, create if not exist--#
file_directory = '110318'
if not os.path.exists(file_directory):
    os.makedirs(file_directory)

#-----iterate through all the cases-----#
phi = [0.50, 0.48]
A2_concentration = [100]
env_temp = [477]

for A2Conc in A2_concentration:
    for EQ in phi:
        for envtemp in env_temp:
            fa.fuelreactor(1e-6, 500e-6, 6e-5, A2Conc, EQ,
properties, envtemp, ct.one_atm, file_directory);

```

## APPENDIX D. ABRAZOM AND SIRIGNANO VAPORIZATION MODEL

In the Abramzon and Sirignano droplet vaporization model, the  $Sh_0$  in Equation 21 and the  $Nu$  in Equation 20 are defined as

$$Sh_0 = 2 \left( 1 + \frac{(1 + Re_d Sc_d)^{1/3} \max[1, Re_d^{0.077}] - 1}{2F(B_M)} \right) \quad (32)$$

$$Nu = 2 \frac{\ln(1 + B_T)}{B_T} \left( 1 + \frac{(1 + Re_d Pr_d)^{1/3} \max[1, Re_d^{0.077}] - 1}{2F(B_T)} \right) \quad (33)$$

The  $F(B_{M,T})$  is defined as

$$F(B_{M,T}) = (1 + B_{M,T})^{0.7} \frac{\ln(1 + B_{M,T})}{B_{M,T}} \quad (34)$$

## APPENDIX E. PSR DROPLET IGNITION CODE (PYTHON)

### Droplet class

```
import numpy as np
class droplet(object):
    '''
        droplet class contains the essential properties for droplets of
        each fuel type, such as density, boiling temperature,
        enthalpy of vaporization...
    '''
    #temperature is in K, SI units are used, droplet only can
    consist one kind of fuel
    #will use average properties if fuel blends are used
    def __init__(self, radius=50e-6, m=1, temp=300, fuel_name='A2'):
        self.r = radius
        self.fuel = fuel_name
        self.T = temp #in kelvin

        #definition of fuel properties
        if self.fuel == 'A2':
            self.IBP = 159.2 + 273
            self.FBP = 270.5 + 273
            self.ABP = (self.IBP + self.FBP)/2
            self.sigma = 23.3*1e-3 #surface tension, J/m^2
            self.rho = 1018.1 - 0.7*self.T
            self.m_fake = 4.0/3.0*self.rho*np.pi*(self.r)**3.0
            self.m_real = m
            self.hfg = 0.428e6 #J/kg
            self.k = 0.08 #W/m-K
            self.cp = 2.6e3 #J/kg-K
            self.MW = 158.6
            self.boiled = False

            #on measurement data

        if self.fuel == 'C1':
            self.IBP = 174.3 + 273 #initial BP
            self.FBP = 263.5 + 273
            self.ABP = (self.IBP + self.FBP)/2 #XXX
            self.sigma = 23.3*1e-3 #surface tension, J/m^2 from
            linearly interpolated graph of the 3 values given
            self.rho = -0.72*self.T + 966.9 #linear interpolation,
            kg/m^3

            self.m_fake = 4.0/3.0*self.rho*np.pi*(self.r)**3.0
            self.m_real = m
            self.hfg = 0.428e6 #J/kg #heat vap
            self.k = 0.08 #W/m-K ##thermal conductivity use same if
            cant find

            self.cp = 2.6e3 #J/kg-K was unavailable
```

```

        self.MW = 178 #g/mol
        self.boiled = False

    if self.fuel == 'C5':
        self.IBP = 156.6 + 273 #initial BP
        self.FBP = 170.6 + 273
        self.ABP = (self.IBP + self.FBP)/2
        self.sigma = (-7*(e-5))*self.T+0.0437
        self.rho = -0.0001*self.T + 0.0617
        self.m_fake = 4.0/3.0*self.rho*np.pi*(self.r)**3.0
        self.m_real = m
        self.hfg = 0.428e6 #J/kg #heat vap
        self.k = 0.08 #W/m-K
        self.cp = 2.6e3 #J/kg-K was unavailable
        self.MW = 178 #g/mol
        self.boiled = False

```

### Droplet entrainer

```
# -*- coding: utf-8 -*-
```

```
"""
```

```
Created on Fri Oct 26 16:31:36 2018
```

```
This will be a entrainer that takes in multiple sizes of drpolets.
```

```
@author: Sheng Wei
```

```
"""
```

```

from droplet import *
import numpy as np
import copy
import sys
#T is used to set temperature of the droplets, mdot is used to
#calculate mean droplet diameter
#D is the droplet diameter

def entrainer(T, mdot, dt, D_arr, Y, fuel='A2'):
    '''
    T-initial droplet temperature
    mdot-droplet entrainment rate
    dt-time step of iteration, will give dm per time step
    X-in microns
    '''
    #assume everytime the kernel entrains 10 droplets, based on the
    fuel mass flow rate
    m_total = mdot*dt #amount of mass per time step
    m_left = copy.copy(m_total)

```



```

    drop_tempo = droplet(1, 1, temp=T) #a "useless" droplet to get
fuel info
    d_arr = []

    #check if D and Y have the same length. if not, exit
    if (len(D_arr) != len(Y) ):
        sys.exit('D_arr and Y_arr need to have same dimension')

    #re-normalize Y array, such that the sum of all values in Y is 1
    Y = Y/np.sum(Y)
    m_frac = Y*m_total

    for i in range(0, len(Y)):
        dm_at_D = m_frac[i]
        D = D_arr[i]
        m_droplet= (4.0/3.0)*np.pi*(D*1e-6/2.0)**3*drop_tempo.rho
        while ((dm_at_D - m_droplet) > 0):
            d_arr.append(droplet(D*1e-6/2.0, m = m_droplet, temp=T,
fuel_name=fuel))
            dm_at_D -= m_droplet
        if (dm_at_D > 0):
            d_arr.append(droplet(D*1e-6/2.0, m = dm_at_D, temp=T,
fuel_name=fuel))
    return d_arr

#derivative as a function of D for the rosin rammler fit
#the diameters need to be in termes of microns
def dQdD_RR(X, q, D):
    """
    Returns the volumetric fraction of the given droplet size
    X - 63% volume less representative droplet size
    q - spread
    D - droplet size
    """
    dQdD = np.power(np.exp(-
    ( np.power((float(D)/float(X)),float(q)) )*((float(D)/float(X)))),
float(q)) *float(q)/float(D)
    return dQdD

def dQdD_RRmodified(X, q, D):
    """
    X - 63% volume less representative droplet size
    q - spread
    D - droplet size
    """
    dQdD = q*((np.log(D))**(q-1))/(D*np.log(X)**q)*np.exp(-
(np.log(D)/np.log(X))**q)
    return dQdD

```

### Heating and vaporization based on Abramzon and Sirignano model

"""

Created on Sun Apr 1 10:24:05 2018

@author: Sheng Wei  
"""

```
import numpy as np
from scipy.integrate import odeint
from droplet import *
import matplotlib.pyplot as plt

def dT_dt(T,t,droplet, Tenv, boilingTemp , re=0):#heat transfer to
droplet, droplet heating and vaporization
    Xsurf = np.exp(-droplet.hfg/8315.0*droplet.MW*(1.0/T -
1.0/boilingTemp))
    Ysurf = Xsurf*droplet.MW/(droplet.MW + 28.85)
    if Ysurf > 1:
        Ysurf = 0.9999999
    B = Ysurf/(1 - Ysurf)
    rho_air = 101325.0/8315.0/Tenv*28.85
    Tr = Tenv + (Tenv + droplet.T)/3.0
    mdot = 2.0*np.pi*rho_air*Dfa(Tr, droplet)*Sh0(B, Re =
re)*droplet.r*np.log(1.0+B)

    h = h_coeff(droplet, Tenv, Re = re)
    #print(h)

    #establish the ordinary differential equation
    A = 4.0*np.pi*droplet.r**2.0
    V = 4.0/3.0*np.pi*droplet.r**3.0

    dTdt = (h*A*(Tenv - droplet.T) -
mdot*droplet.hfg)/(droplet.rho*V*droplet.cp)
    return dTdt

def vaporize(T_kernel, d_array, dt, boilingTemp, re = 0):

    qdot = 0
    mdot = 0

    rho_air = 101325.0/8315.0/T_kernel*28.85
    for droplet in d_array:
        #calculate the wetbulb temperature
        T_wetbulb = TwetBulb(T_kernel, droplet, boilingTemp)

        A = 4.0*np.pi*droplet.r**2.0
        h = h_coeff(droplet, T_kernel, Re = re)

        qdot += h*A*(T_kernel-droplet.T)

        if droplet.T > T_wetbulb:
            droplet.T = T_wetbulb;
            droplet.boiled = True
```

```

15:         if droplet.m_real < 0 or np.absolute(droplet.m_real) < 1e-
            d_array.remove(droplet)
            pass

        if (droplet.T < T_wetbulb and droplet.boiled):
            droplet.T = T_wetbulb;

        if (droplet.T < T_wetbulb and not(droplet.boiled)):
#            print("droplet heating...")
            ts = np.linspace(0,dt,2)
            Ts = odeint(dT_dt,droplet.T,ts,args=(droplet, T_kernel,
boilingTemp, re))
            Tavg = (droplet.T + Ts[1])/2
            Xsurf = np.exp(-droplet.hfg/8315.0*droplet.MW*(1.0/Tavg
- 1.0/boilingTemp))
            Ysurf = Xsurf*droplet.MW/(droplet.MW + 28.85)
            if Ysurf > 1:
                Ysurf = 0.99
            B = Ysurf/(1 - Ysurf)
#            if
(4.0*np.pi*droplet.k*droplet.r/droplet.cp*np.log(1.0+B)>0):
#                mdot +=
4.0*np.pi*droplet.k*droplet.r/droplet.cp*np.log(1.0+B)
                Tr = T_kernel + (T_kernel + droplet.T)/3.0
                droplet.T = Ts[1]
                droplet.m_fake = droplet.m_fake -
2.0*np.pi*rho_air*Dfa(Tr, droplet)*Sh0(B, Re =
re)*droplet.r*np.log(1.0+B)*dt
                droplet.m_real = droplet.m_real -
2.0*np.pi*rho_air*Dfa(Tr, droplet)*Sh0(B, Re =
re)*droplet.r*np.log(1.0+B)*dt
                if droplet.m_real < 0:
                    pass
                else:
                    mdot += 2.0*np.pi*rho_air*Dfa(Tr, droplet)*Sh0(B, Re
= re)*droplet.r*np.log(1.0+B)
                    droplet.r =
(droplet.m_fake*3.0/4.0/np.pi/droplet.rho)**(1.0/3.0)
                    pass

        if droplet.T >= T_wetbulb:
            #B = droplet.cp*(T_kernel-boilingTemp)/droplet.hfg
            Ysurf = 0.9999999
            B = Ysurf/(1 - Ysurf)
            Tr = T_kernel + (T_kernel + droplet.T)/3.0
            droplet.m_fake = droplet.m_fake - h*A*(T_kernel-
droplet.T)/droplet.hfg*dt
            droplet.m_real = droplet.m_real - h*A*(T_kernel-
droplet.T)/droplet.hfg*dt

```

```

        if droplet.m_real < 0:
            pass
        else:
            mdot += h*A*(T_kernel-droplet.T)/droplet.hfg
            #print(Dfa(T_kernel, droplet))
            #qdot += mdot*droplet.hfg
            droplet.r =
(droplet.m_fake*3.0/4.0/np.pi/droplet.rho)**(1.0/3.0)
            pass

    return mdot, qdot

=====
# calculate heat transfer coefficient
=====

def h_coeff(droplet, T_kernel, Re = 0.25):
# Optional way of finding nusselt number, used at beginning of
study, will use a more appropriate model.
    #calculate the nusselt number based on T. Yuge's method, which
does not seem accurate based on his experiemntal approach on solid
spheres
# Pr = 0.7
# #calculate Grashof #
# beta = 0.003695 #thermal expansion coefficient, 1/K ??of air or
fuel droplet??
    L = 2*droplet.r #droplet diameter, m
# g = 9.81 #gravitational acceleration, m/s^2
# rho = 0.25 #density of air, approx., kg/m^3
# del_T = T_kernel - droplet.T
# nu = 530e-7 #air viscosity?E
# Gr = L**3*rho**2*g*del_T*beta/nu**2
#
# #Rayleigh # based on Grashof and Prandtl #'s
# Ra = Gr*Pr
#Nusselt #, based on Abramzon and Sirignano's method
#Reynold's number and Prandtl's number are used as place holder.
Pr = 0.7;
BT = droplet.cp*(T_kernel-droplet.T)/droplet.hfg
FT = (1+BT)**0.7*np.log(1+BT)/BT
Nu = 2*np.log(1.0 + BT)/BT*(1+\
((1.0+Re*Pr)**0.333*np.max([1, Re**0.077]))-
1)/2.0/FT)
    #convective heat transfer coefficient
    #print(Nu)
    k = 0.08e-3*T_kernel-0.021 #thermal conductivity for air
at ?1600K?
    h = Nu*k/L
    return h

=====

```

```

# calculate the wetbulb temperature
#=====
def TwetBulb(T_kernel, droplet, boilingTemp):
    BT = droplet.cp*(T_kernel-boilingTemp)/droplet.hfg
    YS = BT/(1+BT)
    XS = YS*28.85/(droplet.MW - YS*(droplet.MW - 28.85))
    T_wetbulb = 1/(1.0/boilingTemp -
8314/droplet.MW/droplet.hfg*np.log(XS))
    return T_wetbulb

#=====
# calculate the binary diffusion coefficient, use the binary
diffusion coefficient of n-Dodecane
#=====
def Dfa(T_kernel, droplet, P = 1): #unit of P is atm
    Mf = droplet.MW #kg/mol
    Ma = 28.97#kg/mol
    sigmaFA = 0.5*(6.60 + 3.617) #average cross section between
fuel and air
    Tref = T_kernel/np.sqrt(454.7*97) #the reference temperature
based on fuel and air's Lenard-jones energy
    omegaFA = 1.06036/np.power(Tref, 0.15610) +
0.193/np.exp(0.47635*Tref) \
        + 1.03587/np.exp(1.52996*Tref) +
1.76474/np.exp(3.89411*Tref)
    Dfa = 1.8583e-7*np.sqrt(np.power(T_kernel, 3.0)* (1.0/Mf +
1.0/Ma))*1.0/(P*sigmaFA*omegaFA)
    #print(Dfa)
    return Dfa

#
#=====
# calculate the sherwood number
#=====
=
def Sh0(BM, Re= 0.25, Sc=1):
    FM = np.power((1 + BM), 0.7)*np.log(1+BM)/BM
    sh0 = 2.0*(1+(np.power((1+Re*Sc), 1.0/3.0)*np.max([1,
Re**0.077])-1)/(2.0*FM))
    #print(sh0)
    return sh0

```

### Example execution code (the main file)

```

# -*- coding: utf-8 -*-
"""
Created on Wed Oct 3 14:04:51 2018

@author: Sheng Wei
"""

'''
Read data from air plasma kernel evolution histroy, first stage

```

```

'''
import os
import datetime

from DropletIgnitionKernel_multiple_sizes import *
#from tabulate import tabulate
#include the parameters that need to be varied into execute,
parameters include air temperature,
#reading in the information, for air plasma in 300K cross flow air,
plasma at 30 microsecond
#May need to rerunk the first stage reactor
f = open('plasma_200_microsec_300K.csv', 'r+');
spamreader = csv.reader(f, delimiter=',');
for row in spamreader:
    if spamreader.line_num == 3:
        plasma_temp = float(row[1]);
        plasma_pressure = float(row[2]);
        plasma_volume = float(row[3]);
        #-----capture the mole fractions-----#
        plasma_N2 = float(row[4]);
        plasma_O2 = float(row[5]);
        plasma_NO = float(row[6]);
        plasma_N = float(row[7]);
        plasma_O = float(row[8]);
f.close();

properties = [plasma_temp, plasma_pressure, plasma_volume,
plasma_N2\
               , plasma_O2, plasma_NO, plasma_N, plasma_O]

'''
The droplet introduced, second stage

'''

'''
Make a folder that stores results from today's simulation
'''
now = datetime.datetime.now()
folder = str(now.year) + '_' + str(now.month) + '_' + str(now.day)

if not os.path.exists(folder):
    os.makedirs(folder)

##Change the properties here that you are interested in varying
BP = 433 #boiling temperature
AirTemp = 400#air temperature
FuelTemp = 300 #fuel temperature
fuelType = 'A2' #fuel type
EndTime = 500e-6 #total time to run,s
del_t = 1e-6 #time step,s

```

```

phi = 1 #equivalenc ratio
Re = 0

#the lengths of D array and the Y array need to be the same, D_arr
is the droplet size array
#Y_arr is the mass fraction array

#=====
# generate D and Y vectors based on rosin rammler distribution
#=====
def dQdD_RR(X, q, D):
    '''
    Returns the volumetric fraction of the given droplet size
    X - 63% volume less representative droplet size
    q - spread
    D - droplet size
    '''
    dQdD = np.exp(-( np.power((float(D)/float(X)),float(q)))) *
np.power((float(D)/float(X)), float(q)) *float(q)/float(D)
    return dQdD

Y_arr = []
D_arr = np.linspace(5, 30, 10)
for D in D_arr:
    Y_arr.append(dQdD_RR(20, 10, D))
Ynorm = Y_arr/np.sum(Y_arr)
plt.ylim([0,0.3])
plt.scatter(D_arr, Y_arr)

plt.show()

#Y_arr = [1]
#D_arr = [20]

#print a table of the important parameters
#print(tabulate(["Fuel","D(micron)", "BP", "AirTemp",
"DropletTemp"],[fuelType, D*1e6, BP, AirTemp, FuelTemp]))
#filename = folder + '/' + 'BP' + str(BP) + 'AirTemp' + str(AirTemp)
+ \
#         'FuelTemp' + str(FuelTemp) + fuelType + '.csv'
filename = 'X20q_10micron_Re0UniformDropletDisstribution.csv'
'''
In execute, the parameters are:
1. properties - properties of the air plasma kernel at the end
of the transit time
2. D - Droplet size
3. BP - boiling point (use recovery temperatures)
4. AirTemp - Temperature of the ambient fluid

```

```

5. FuelTemp - Temperature of the fuel
6. filename - file name for saving the current run
7. dt - time step
8. endtime - how long the kernel should run
9. EQ - equivalence ratio
10. mdot_air - mass entrainment rate of air
11. Fuel type - A2, C1
'''

execute(properties, BP, AirTemp, FuelTemp, D_arr, Y_arr, filename,
dt=del_t, \
    endtime=EndTime, EQ=phi, mdot_air = 3e-5, fueltype=fuelType,
re=Re)

```



## APPENDIX F. ASME D341 – PYTHON CODE FOR VISCOSITY

### APPROXIMATION

```
# -*- coding: utf-8 -*-
"""
Created on Mon Sep 11 13:57:59 2017
This program computes the relation between temperature and
viscosity, using asme method D341
loglogZ = A - B*logT
@author: Sheng Wei
"""

import numpy as np
import matplotlib.pyplot as plt
log = np.log10

#define all parameters that depends on viscosity
def C(nu):
    return np.exp(-1.14833 - 2.65868*nu)
def D(nu):
    return np.exp(-0.0038138 - 12.5646*nu)
def E(nu):
    return np.exp(5.46491 - 37.6289*nu)
def F(nu):
    return np.exp(13.0645 - 74.6851*nu)
def G(nu):
    return np.exp(37.4619 - 192.643*nu)
def H(nu):
    return np.exp(80.4945 - 400.468*nu)
def Z(nu):
    return nu + 0.7 + C(nu) - D(nu) + E(nu) - F(nu) + G(nu) - H(nu)

if __name__ == '__main__':
    #calculate coefficients A and B
    T0 = float(input("Enter first temperature in K:"))
    nu0 = float(input("Enter first nu in mm^2/s:"))
    T1 = float(input("Enter second temperature in K:"))
    nu1 = float(input("Enter second nu:"))

    fuel = input("Enter fuel name, e.g, A2 :")

    B = (log(log(Z(nu0))) - log(log(nu1)))/(log(T1) - log(T0))
    A = log(log(Z(nu0))) + B*log(T0)

    nu = np.linspace(0.21, 20, 1000)

    T = []

    for v in nu:
        try:
```

```

        T.append(np.power(10, ((A - log(log(Z(v))))/B)))
    except:
        print((A - log(log(Z(v))))/B)

plt.plot(T, nu)

filename = fuel + '_D341Viscosity.csv'
f = open(filename, 'w+')
f.write('temperature(K), viscosity(cst)\n')

for i in np.arange(nu.size):
    f.write(str(T[i]) + ',' + str(nu[i]) + '\n')

f.close()

```

## APPENDIX G. ABSOLUTE IGNITION PROBABILITY RANKING

Table 7. Absolute ignition probability for room temperature fuel spray.<sup>6</sup>

	p	65% uncertainty
A1	0.047	0.006
A2	0.035	0.005
A2-2018	0.124	0.008
A3-2018	0.079	0.006
C1	0.030	0.005
C2	0.016	0.005
C3	0.016	0.005
C4	0.050	0.005
C5	0.050	0.006
C7-2018	0.039	0.006
C8-2018	0.093	0.008
C9-2018	0.036	0.006
S1	0.043	0.005
S2	0.046	0.005
n-dodecane	0.036	0.006

---

<sup>6</sup> The data are taken in two campaigns. The data labeled with 2018 were taken in 2018, while the rest were taken in 2017. A2 is taken in both 2017 and 2018 for comparable ranking. The rig was modified in 2018 so the absolute probability changed.

Table 8. Absolute ignition probability for chilled fuel spray.

Fuel	P	65% uncertainty
A1	0.0447	0.0048
A2	0.0151	0.0028
A3	0.0017	0.0012
C1	0.0251	0.0030
C3	0.0032	0.0013
C4	0.0517	0.0051
C5	0.0612	0.0050
C7	0.0032	0.0019
C8	0.0036	0.0016

## REFERENCES

1. Turns, S.R., *An Introduction to Combustion: Concepts and Applications*. 3 ed. 2011, New York: McGraw-Hill Education.
2. ASTM, *Standard Practice for Qualification and Approval of New Aviation Turbine Fuels and Fuel Additives*, in *ASTM D4054-16*. 2016, ASTM International: West Conshohocken, PA.
3. ASTM, *Standard Specification for Aviation Turbine Fuel Containing Synthesized Hydrocarbons*, in *ASTM D7566-17a*. 2017, ASTM International: West Conshohocken, PA.
4. Colket, M., et al., *Overview of the National Jet Fuels Combustion Program*. AIAA Journal, 2017. **55**(4): p. 1087-1104.
5. Striebel, D.S.a.E.E., *Starting means for a gas turbine engine*, U.S. Patent, Editor. 1983, United Technologies Corp: USA.
6. Boileau, M., et al., *LES of an ignition sequence in a gas turbine engine*. Combustion and Flame, 2008. **154**(1-2): p. 2-22.
7. Mastorakos, E., *Ignition of turbulent non-premixed flames*. Progress in Energy and Combustion Science, 2009. **35**(1): p. 57-97.
8. Brandon Sforzo, J.K., Jeff Jagoda and Jerry Seitzman, *Ignition Probability in a Stratified Turbulent Flow With a Sunken Fire Igniter*. J. Eng. Gas Turbines Power, 2014. **137**(1): p. 8.
9. Lefebvre, A.H., *Fuel effects on gas turbine combustion-ignition, stability, and combustion efficiency*. J. Eng. Gas Turbines Power 1985. **107**(1): p. 14.
10. C. Gleason, O.L.O., T & W. Shayeson, M & W. Bahr, D., *Evaluation of Fuel Character Effects on the F101 Engine Combustion System*. Technical Report AFAPL-TR - Air Force Aero Propulsion Laboratory, 1979.
11. Gleason, C.C., Oiler, T. L., Shayeson, M. W., and Bahr, D. W., *Evaluation of Fuel Character Effects on J79 Engine Combustion System*. AFAPL-TR-79-2015, 1979.
12. Gleason, C.C., Oiler, T. L., Shayeson, M. W., and Kenworthy, M. J., *Evaluation of Fuel Character Effects on J79 Smokeless Combustor*. AFWAL-TR-80-2092, 1980.

13. Oiler, T.L., Gleason, C. C , Kenworthy, M. J., Cohen, J. D., and Bahr, *Fuel Mainburner/Turbine Effects*. AFWAL-TR-81-2100, 1982.
14. Vogel, R.E., Troth, D. L., and Verdouw, A. J., *Fuel Character Effects on Currentf High-Pressure Ratio, Can-Type Turbine Combustion Systems*. AFAPL-TR-79-2072, 1980.
15. Russell, P.L., *Fuel Mainburner/Turbine Effects*. AFWAL-TR-2081, 1982.
16. Lefebvre, A.H., *Fuel Effects on Gas Turbine Combustion—Ignition, Stability, and Combustion Efficiency*. J. Eng. Gas Turbines Power, 1985. **107**(1): p. 24-37.
17. Thomas Mosbach, V.B., Barani Gunasekaran, *Fuel Composition Influence on Gas Turbine Ignition and Combustion Performance*, in *ASME Turbo Expo 2015: Turbine Technical Conference and Exposition*. 2015: Montreal, Quebec, Canada.
18. D.R. Ballal, A.H.L., *A general model of spark ignition for gaseous and liquid fuel-air mixtures*. Symposium (International) on Combustion, 1981. **18**(1).
19. Lefebvre, D.R.B.A.H., *Igniton and flame quenching of quiescent fuel mists*. Proc. R. Soc. Lond. A., 1978. **364**: p. 17.
20. Fajardo, C.M., J.D. Smith, and V. Sick, *PIV, high-speed PLIF and chemiluminescence imaging for near-spark-plug investigations in IC engines*. Journal of Physics: Conference Series, 2006. **45**: p. 19-26.
21. Sforzo, B., et al., *Post discharge evolution of a spark igniter kernel*. Combustion and Flame, 2015. **162**(1): p. 181-190.
22. Lefebvre, A.H. and D.R. Ballal, *Gas Turbine Combustion: Alternative Fuels and Emissions*. 2010, 6000 Broken Sound Parkway NW, Suite 300, Boca Raton, FL 33487-2742.
23. Sforzo, B., *HIGH ENERGY SPARK IGNITION IN NON-PREMIXED FLOWING COMBUSTORS*, in *Aerospace Engineering*. 2014, Georgia Institute of Technology: Atlanta Georgia.
24. Didden, N., *On the formation of vortex rings: Rolling-up and production of circulation*. Journal of Applied Mathematics and Physics, 1979. **30**(1): p. 101–116.
25. Krueger, A.B.O.a.P.S., *Measurement of ambient fluid entrainment during laminar vortex ring formation*. Experiments in Fluids, 2008. **44**(2): p. 235–247.
26. Johari, H., *Scaling of fully pulsed jets in crossflow*. AIAA journal, 2006. **44**(11): p. 2719–2725.
27. Hanson, R.K., *Planar Laser-Induced Fluorescence Imaging*. J. Quant. Spectrosc. Radtat. Transfe, 1988. **40**(3): p. 343-362.

28. Seitzman, J.M.a.H., R.K., *Planar Fluorescence Imaging in Gases*. Experimental Methods for Flows With Combustion ed. A. 1993, London: Taylor Academic Press.
29. Hanson, R.K. *Introduction to Planar Laser-Induced Fluorescence*. 12/16/2018]; Available from: [https://hanson.stanford.edu/researchReports/plif/Introduction\\_to\\_Planar\\_Laser-Induced\\_Fluorescence.pdf](https://hanson.stanford.edu/researchReports/plif/Introduction_to_Planar_Laser-Induced_Fluorescence.pdf).
30. A. Lozano, B.Y., R. K. Hanson, *Acetone: a tracer for concentration measurements in gaseous flows by planar laser-induced fluorescence*. Experiments in Fluids, 1992. **13**(6): p. 369–376.
31. B. K. McMillin, J.M.S., and R. K. Hanson, *Comparison of NO and OH planar fluorescence temperature measurements in scramjet model flowfield*. AIAA Journal, 1994. **32**(10 ): p. 1945-1952.
32. Jerry M. Seitzman, G.K., and Ronald K. Hanson, *Instantaneous temperature field measurements using planar laser-induced fluorescence*. Optics Letters, 1985. **10**(9): p. 439-441.
33. Arthur H. Lefebvre, V.G.M., *Atomization and Sprays*. 2017, Florida, USA: CRC Press Taylor & Francis Group.
34. *Cantera*. 2018 [cited 2018 Dec.5]; Cantera is an open-source suite of tools for problems involving chemical kinetics, thermodynamics, and transport processes.]. Available from: <https://cantera.org/>.
35. Robert J. Kee, M.E.C., Peter Glarborg, *Chemically Reacting Flow : Theory and Practice*. 1 ed. 2003, New Jersey: Wiley-Interscience.
36. Wang, H., et al., *A physics-based approach to modeling real-fuel combustion chemistry - I. Evidence from experiments, and thermodynamic, chemical kinetic and statistical considerations*. Combustion and Flame, 2018. **193**: p. 502-519.
37. H. Wang, X.Y., A.V. Joshi, S.G. Davis, A. Laskin, F. Egolfopoulos, C.K. Law, *USC Mech Version II. High-Temperature Combustion Reaction Model of H2/CO/C1-C4 Compounds*. 2007.
38. Sforzo, B.D., Hoang; Wei, Sheng; Seitzman, Jerry, *Liquid Fuel Composition Effects on Forced, Nonpremixed Ignition*. Journal of Engineering for Gas Turbines and Power, 2017. **139**(3).
39. ABRAMZON, B. and W.A. SIRIGNANO, *Droplet vaporization model for spray combustion calculations* int. J. Heat Mass Transfer, 1989. **32**(9): p. 1605-1618.
40. S.S. Sazhin, T.K., W.A. Abdelghaffar, M.R. Heikal, *Models for fuel droplet heating and evaporation: Comparative analysis*. Fuel, 2006. **85**(12-13): p. 1613-1630.

41. ASTM, *Standard Test Method for Determination of Ignition Delay and Derived Cetane Number (DCN) of Diesel Fuel Oils by Combustion in a Constant Volume Chamber*, in ASTM D6890-16e2. 2016: West Conshohocken, PA.
42. ASTM, *Standard Practice for Viscosity-Temperature Charts for Liquid Petroleum Products*, in D341-17. 2017, ASTM: West Conshohocken, PA.
43. John H Lienhard V, J.H.L.I., *A Heat Transfer Textbook: Fourth Edition* 4th ed. Dover Civil and Mechanical Engineering. 2015: Dover Publications.
44. Yuge, T., *Experiments on Heat Transfer From Spheres Including Combined Natural and Forced Convection*. J. Heat Transfer 1960. **82**(3): p. 214-220.